Trinity College Dublin
Coláiste na Tríonóide, Baile Átha Cliath
The University of Dublin

Bose condensation in nonequilibrium quantum gases

An adventure in the thermodynamics of light and matter

Luisa Toledo Tude

School of Physics

A thesis submitted in partial fulfillment of the requirements towards the degree of

Doctor of Philosophy in Physics

Hilary Term 2025

Declaration

I declare that this thesis has not been submitted as an exercise for a degree at this or any other university and it is entirely my own work.

I agree to deposit this thesis in the University's open access institutional repository or allow the library to do so on my behalf, subject to Irish Copyright Legislation and Trinity College Library conditions of use and acknowledgement.

I consent consent to the examiner retaining a copy of the thesis beyond the examining period, should they so wish (EU GDPR May 2018).

Signed: ____________________ Date: ____________________

Bose condensation in nonequilibrium quantum gases
An adventure in the thermodynamics of light and matter

Luísa Toledo Tude
Michaelmas Term 2024

Abstract

Nonequilibrium condensates in microcavities have been extensively analysed over the past decades. Like equilibrium condensates, they are characterised by a macroscopic population of the ground state, however, the system is subjected to gain and loss through the finite lifetime of the microcavity. In these systems, a Bose gas is an open system in which heat and particles are continually exchanged with reservoirs. Based on the collection of knowledge of their kinetics provided by simulations and by experimental works, we show that these gases act as thermal machines whose output power is coherent emission of light. As in the case of a laser, these thermal machines are constrained by the second law of thermodynamics and operate with efficiency bounded by the Carnot limit.

We considered in depth condensation of both exciton-polaritons and photons. Starting with polaritons, we constructed a few-level model that captures the main processes involved in the buildup of a ground state population. The model consists of a three-level system interacting with a field and connected to a hot and a cold thermal reservoir, that represents a non-resonant pump and the lattice phonons. This subsystem can drive a condensate, through polariton-polariton scattering, which produces work in the form of coherent light emission from the microcavity. We obtain a phase diagram as a function of the temperatures of the two baths and analyse the phase transition.

To extend the analysis to a photon gas we use a kinetic approach to show that condensation is also restricted by the second law of thermodynamics and that, with a resonant pump, it can be mapped to a three-level heat engine model. We continue the analysis by exploring the effects of altering the pump on the steady state of the system. We show that condensation can be achieved using sunlight as a source and obtain its efficiency.

Our results elucidate a new link between nonequilibrium condensation and lasers. Beyond that, we also discuss the connection of these phenomena with synchronisation.

Acknowledgements

First of all, I would like to thank my supervisor Paul Eastham for his guidance during this PhD. From him I received more support than I could even hope for. And I not only learned a lot from him, but also had a great time in our discussions.

I would also like to thank all my office colleagues and friends that I met in Dublin during the last years. I am specially grateful to Carlos and Eoin for all the interesting physics discussions, and to Magdalini, Laetitia, and Artur for the support and friendship.

Outside of physics, I would like to thank my family and friends in Brazil, whose love and encouragement were essential during my PhD, and to Mika and Glenn for all the care and making me feel home.

List of publications

The results discussed in this thesis appeared in the following publications:

1. L. T. Tude and P. R. Eastham,
   Quantum thermodynamics of driven-dissipative condensates
   APL Quantum 1.3 (2024).
2. C. N. Murphy, L. T. Tude and P. R. Eastham,
   Laser Cooling beyond Rate Equations: Approaches from Quantum Thermodynamics
   Applied Sciences 12.3 (2022), 1620.

The following work, although unrelated to the main topics of this thesis, was completed and published during the course of the PhD:

1. L. T. Tude, C. N. Murphy and P. R. Eastham,
   Overcoming temperature limits in the optical cooling of solids using light-dressed states
   Physical Review Letters 132.26 (2024), 266901.

The code used to generate the data in this thesis is openly available in Zenodo at 10.5281/zenodo.14740150.

Contents

1. Introduction 1

2. Background 5
  2.1 Bose-Einstein condensates 5
  2.2 Methods for non-equilibrium condensates 8
    2.2.1 The Boltzmann equation 9
    2.2.2 Quantum master equations 10
  2.3 Quantum thermodynamics. 13
    2.3.1 Three-level heat engine 16
    2.3.2 Counting field statistics 19
  2.4 Synchronisation of classical oscillators 21

3. Polariton Condensation. 23
  3.1 Microcavity Polaritons 24
  3.2 Kinetics of polariton condensation 27
    3.2.1 Polariton-phonon interaction 28
    3.2.2 Polariton-polariton interaction 31
  3.3 Discussion 34

4. Thermodynamics of Polariton Condensation 37
  4.1 Condensates as heat engines. 38
  4.2 Methods 43
  4.3 Results 45
    4.3.1 Steady state of the microcavity. 47
    4.3.2 Effects of the internal structure of the reservoirs. 52
    4.3.3 Thermodynamic figures of merit 55
    4.3.4 Modes of operation of the thermal machine. 56
  4.4 Conclusions 58

5. Photon Condensation 61
5.1 A model of photon condensation 63
5.2 Nonequilibrium thermodynamics: heat engines and the second law . . . 68
5.3 Condensation pumped by a thermal source of light 70
5.3.1 A two-level photon gas 71
5.3.2 Solar-pumped multimode model 73
5.4 Conclusions 80

6. Universality of coherent phenomena 81
6.1 Mean-field approach 84
6.2 Synchronisation in the quantum regime 88
6.3 Discussion 93

7. Conclusions 95

Bibliography 98

A. Polariton heat engine: equations-of-motion 109

Chapter 1

Introduction

Bose-Einstein condensates (BECs) are an ordered state of matter in which quantum properties manifest on a macroscopic scale. Originally conceived as an equilibrium phenomenon, condensates form when a gas of bosons is cooled to low temperatures. As the thermal energy decreases, the de Broglie wavelength of the particles becomes comparable to the average space between them, leading to an overlap of wave functions. This results in symmetry breaking and a phase transition to a collective state.

Nonequilibrium condensates extend this concept to systems that undergo gain and loss. They are quantum states that exhibit macroscopic coherence and collective behaviour, but operate away from thermodynamic equilibrium. Examples of Bose gases in which nonequilibrium condensates have been demonstrated include those of exciton-polaritons in inorganic [1] and organic semiconductors [2], photons in semiconductors [3] and in dye-filled cavities [4, 5], plasmon-polaritons [6], and magnons [7].

This out-of-equilibrium phenomenon represents a rich intersection between quantum optics and condensed matter physics, leading to applications in quantum optoelectronic devices like lasers, switches, and transistors. When implemented in optical microcavities, as with photons and polaritons, the low mass of the confined light enables condensation to occur at room temperature [8]. This, combined with the development of electronically injected condensates [9, 10], offers considerable experimental advantages, increasing the practicality of implementing these condensates into controllable energy-efficient small-scale devices [11, 12].

Additionally, nonequilibrium BECs are pivotal in fundamental research on collective states and pattern formation, including synchronisation, superfluidity, and vortices. For example, a lattice of polariton condensates can be used to simulate the XY Hamiltonian and, by analogy, it reproduces the behaviour of other systems such as unconventional superfluids, spin liquids, the Berezinskii–Kosterlitz–Thouless phase transition, and classical magnetism [13].

Nonequilibrium condensates represent an intermediate state between a conventional laser and an equilibrium Bose-Einstein condensate. As BECs, they exhibit a macroscopic occupation on the ground state, while, like lasers, they require a continuous external pump, and operate away from thermal equilibrium, to generate coherent emission. The extent to which the steady state particle distribution of a condensate resembles equilibrium depends on the relative time scales of loss and thermalisation. For example, photons and magnons can quickly reach a quasi-equilibrium state, while in exciton-polariton gases, the thermalisation time is usually similar to the lifetime of the particles in the cavity, and so an equilibrium distribution is not achieved. However, regardless of the particle distribution, there is, in any case, a continuous flow of energy and particles, maintaining a steady state condition where the losses are balanced by gain from an external pump.

The dynamics and steady states of these condensates have been studied with different models, using kinetic equations and field-theoretic approaches, among other techniques. In this thesis, we aim to use thermodynamics to derive a general theory of nonequilibrium condensation in Bose gases. We focus on exciton-polaritons and photons and argue that, from a fundamental perspective, the emission of coherent light is the output power of a thermal machine. In this way, the constraint of positive entropy production imposed by the second law of thermodynamics provides a general way of identifying requirements for condensation.

The next two chapters will serve as an introduction to our main results. In chapter 2 we present a brief summary of important concepts used later in the thesis, and in chapter 3 we present a theory of microcavity polaritons and a kinetic approach to condensation. By analysing the role of phonon-polariton and polariton-polariton interactions separately, we lay the groundwork used in the thermodynamic analysis presented in the following chapter.

In chapter 4 we analyse condensation using the framework of quantum thermodynamics. Based on the collection of knowledge about polariton kinetics provided by kinetic simulations and by experimental works, we construct a few-level model that captures the main processes involved in the buildup of a ground-state population of polaritons. The model consists of a three-level system interacting with a classical field (which is the condensate) and connected to a hot and a cold thermal reservoir, that represent a pump and the lattice phonons. The three-level system is similar to a laser model [14], whose connection to thermal machines has been extensively studied [14–19]. We analyse condensation using our model and obtain a phase diagram as a function of the temperatures of the two baths and the chemical potential.

In chapter 5 we extend our approach to photon condensation. We use a kinetic theory to analyse entropy generation and its restrictions on condensation. Our results consist of a new approach to obtaining restriction of condensation that rely on thermodynamics. It shows that although the system can reach thermalisation, its nonequilibrium nature still plays an important role in defining the phase boundary to condensation. We start with the analysis of a photon gas pumped at the dye frequency and extend the analysis to show that condensation could be achieved from sunlight harvesting.

In chapter 6, we continue the analysis of nonequilibrium condensation by discussing the connections to laser and synchronisation phenomena. We use a mean-field approach to analyse the threshold of a laser, which is constrained by the emergency of a limit cycle and happens concurrently with the field-spin synchronisation. In chapter 7, we present final remarks and conclude the thesis.

Chapter 2

Background

IN WHICH WE SET THE GROUNDWORK FOR THE REST OF THE THESIS

Throughout this thesis, we will approach condensation in nonequilibrium quantum gases from the perspective of thermodynamics. Our approach can give a new interpretation of results already existent in the literature and add original insights into how the restrictions imposed by the laws of thermodynamics reflect in the condensation constraints. Therefore, the comprehension of both nonequilibrium condensation and quantum thermodynamics is indispensable.

In this chapter, we review concepts of Bose-Einstein condensation and the methods that will be used later on in the thesis to describe driven-dissipative condensates. Next, we introduce definitions and concepts regarding thermodynamics in the quantum regime and present how they apply in a simple model of a quantum thermal machine.

2.1 Bose-Einstein condensates

Bose-Einstein condensates (BECs) are an ordered state of matter in which microscopic quantum phenomena become visible macroscopically. They are achieved by identical bosons with low thermal energy when the inter-particle spacing is small compared to the de Broglie wavelength. As a result, the waves overlap, acquiring a single collective phase.

The existence of BECs is explained by the statistical properties of quantum identical particles. The occupation distribution of states $\mathbf{k}$ in a Bose gas with inverse temperature β and chemical potential μ is

$$n_{\mathbf{k}} = \frac{1}{e^{\beta(\epsilon_{\mathbf{k}}-\mu)} - 1}, \tag{2.1}$$

where we have taken the energy of the ground state to be zero. The total number of particles is given by the sum $\sum_{\mathbf{k}} n_{\mathbf{k}}$. Hence, if the occupation shows little variation with $\mathbf{k}$, in the thermodynamic limit the sum can be replaced by an integral, and the density of the gas is

$$\rho = \frac{1}{(2\pi)^3} \int \frac{d\mathbf{k}}{e^{\beta(\epsilon_{\mathbf{k}}-\mu)} - 1}. \tag{2.2}$$

However, because $\mu < 0$ the right-hand side of Eq. (2.2) can have an upper bound ρ_c. For densities above this critical value the assumption of smooth variation of $n_{\mathbf{k}}$ is not valid, meaning the gas must have at least one state with a macroscopic occupation. In principle, more than one state could play the role of keeping these excess particles. But, even if the inter-particle coupling is weak, it affects the stability of the distribution making the configuration with a macroscopic occupation of the ground state the less energetic [20].

A critical temperature of condensation is obtained defining the phase transition as the point at which $\mu = 0$ [21]. In a three-dimensional system

$$T_c = \left(\frac{2\pi\hbar^2}{mk_b}\right)\left(\frac{\rho}{2.612}\right)^{2/3}. \tag{2.3}$$

In two dimensions, the improper integral in Eq. (2.2) is not bounded. Therefore, condensation can only happen if the limits of integration are finite. In other words, condensation is restricted to finite spaces in 2D.

The existence of a macroscopic occupation of a single-particle state is what characterises condensation as a new state of matter. Nevertheless, it must always be accompanied by two other essential properties: gauge symmetry breaking and coherence. The first implies that the macroscopic state has a well-defined phase. This means that the most appropriate order parameter for the phase transition is the average of the annihilation operator rather than the number of particles in the ground state. The second implies that the phase must be coherent over a long time and distances. For a condensate of photons or polaritons, the coherence can be measured by the first and second-order correlation functions of the electromagnetic field [21]

$$g_1(\mathbf{r},\mathbf{r}',t,t') = \frac{\langle E^*(\mathbf{r}',t')E(\mathbf{r},t)\rangle}{\sqrt{\langle E^*(\mathbf{r}',t')^2\rangle\langle E(\mathbf{r},t)^2\rangle}} \tag{2.4}$$

$$g_2(\mathbf{r},\mathbf{r}',t,t') = \frac{\langle E^*(\mathbf{r}',t')E^*(\mathbf{r},t)E(\mathbf{r},t)E(\mathbf{r}',t')\rangle}{\langle E^*(\mathbf{r}',t')^2\rangle\langle E^*(\mathbf{r},t)^2\rangle}. \tag{2.5}$$

In the steady state, these quantities depend only on $|\mathbf{r}-\mathbf{r}'|$ and $|t-t'|$ and are usually measured fixing one of the variables, i.e, taking $\mathbf{r}=\mathbf{r}'$ or $t=t'$. For example, the first-order temporal correlation $g_1(\tau)=g_1(\mathbf{r},\mathbf{r},t+\tau,t)$ is expected to show a power law decay $g_1(\tau)=\tau^{-\eta}$ with $\eta=\frac{k_bTm}{2\pi\rho\hbar^2}$ for a two-dimensional condensate [21]. The second-order temporal correlation $g_2(\tau)=g_2(\mathbf{r},\mathbf{r},t+\tau,t)$ is expected to be $g_2(0)=1$ for a coherent state and tends to the value expected for a thermal state $g_2(\tau)=2$ as the delay time increases [21].

The first observation of condensation was of Helium-4 at temperatures of approximately 2K, and was shown to be the cause of superfluidity [20]. In the 90s, condensation was achieved by a combination of cooling techniques in dilute atomic gases such as rubidium [22] and sodium [23]. While these examples are an equilibrium phenomena, there are now many situations where condensation occurs in the nonequilibrium steady states of driven open systems. Examples include condensates of exciton-polaritons in inorganic [1] and organic semiconductors [2], photons in dye-filled cavities [4, 5], plasmon-polaritons [6], and magnons [7]. These particles have a finite lifetime, and the condensate must be maintained against losses by gain from an external pump. Some condensates, such as those of photons and magnons, quickly reach a quasi-equilibrium state, and so can to an extent be treated using equilibrium thermodynamics. However, in other systems, such as polaritons, a macroscopic occupation of the ground state can be obtained even in cases where thermalisation is not fully achieved.

In this thesis, we aim to develop the basis of a general theory to describe condensation in driven-dissipative condensates. However, we focus on polariton and photon condensates achieved in optical microcavities filled with a semiconductor and a dye solvent, respectively. Condensation in optical microcavities has attracted attention over the last decades because of the high temperature at which the photon mass enables it to occur [24]. The practical applications of condensation in microcavity systems include quantum computing [25, 12], analog simulation [13], topological states [26], and optoelectronic devices such as novel laser sources [4], switches [27], sensors [28] and transistors [29]. Furthermore, driven-dissipative condensates have also been used as a playground for the study of fundamental properties of collective states and pattern formation such as synchronisation, superfluidity, and vortexes [21, 30].

2.2 Methods for non-equilibrium condensates

Driven dissipative condensates are typically obtained by cooling down a quantum gas to a temperature below the threshold, and this cooling mechanism can be described as the extraction of energy by an external reservoir. Moreover, the out-of-equilibrium nature of these gases requires an external pump acting to compensate for the finite lifetime of the particles. Both the energy extraction and the particle flow in the steady state of the condensate are described by the framework of open quantum systems, in which a system interacts with an external environment.

In this section, we explain the methods used throughout the thesis to describe the effects of interaction with an external environment. We do not intend to account for all possible approaches, but just the ones relevant to comprehension of the results in the thesis. Other methods commonly used in the literature are non-Hermitian Hamiltonians [31], input-output theories [32], the Keldysh formalism [33, 20], and the Gross-Pitaesvkii equation [30].

2.2.1 The Boltzmann equation

The quantum Boltzmann equation is a Fokker-Plank-type equation that describes the evolution of the distribution of particles of a gas in momentum space. Its general form is

$$\frac{\partial n_i}{\partial t} = \sum_s W^{(s)}_{f\to i} - W^{(s)}_{i\to f}, \tag{2.6}$$

where $W^{(s)}_{f\to i}$ and $W^{(s)}_{i\to f}$ are the scattering rates into and out of a state i due to a certain interaction labeled as s. If the density of particles is low, first-order perturbation theory is valid, and the scattering rates are given by Fermi's golden rule

$$W_{i\to f} = \frac{2\pi}{\hbar} \sum_f |\left\langle f\right| V_{\text{int}} \left|i\right\rangle|^2 \delta(E_f - E_i). \tag{2.7}$$

The indexes f and i correspond to the final and initial state, respectively, and V_{int} is the interaction Hamiltonian. The evolution can be obtained by numerical iteration, where $n_i(t+dt) = n_i(t) + \left(\frac{\partial n_i}{\partial t}\right) dt$, and dt the time step.

The Boltzmann equation is a consequence of the H-theorem of statistical physics and evolves the system toward equilibrium. In cases where the total number of particles is not conserved in the system, a term for the rates of loss and gain can be added to the equation. This approach has been used to describe the evolution and steady-sate properties of systems such as excitons [34, 35], polaritons [36, 37], and photons [5]. However, it does not encompass features such as the phases and coherences, that can be relevant depending on the analysis. Typically, the Boltzmann equation is valid as long as the interaction strengths of each interaction considered are small in comparison to the energy scales of the system, so that perturbation theory can be used. In addition, it relies on the mean-field approximation over the particle number operator, $\hat{n}_i \approx n_i$, which requires a large number of particles. As the system grows, individual fluctuations become less significant, and the average field better represents the overall behaviour.

2.2.2 Quantum master equations

The Schrodinger equation correctly describes the evolution of any physical (closed) system; however, in many cases, a system is big, and it is impracticable to calculate its dynamics. In these cases, one must resort to approximations. In the framework of open quantum systems, we split the full system into a subsystem of interest $\mathcal{S}$ and an environment $\mathcal{E}$, and follow with approximations (which depend on the particularities of each case) to describe the evolution $\mathcal{S}$ only. This part of interest is an open quantum system and the equation describing its dynamics is the so-called dynamical map [38]. A typical case is that of the systems described in this thesis, where the dynamics of an open quantum system can be described by a time-local master equation for its reduced density matrix. We obtain such equations from microscopic models that consider the environment explicitly by making the weak-coupling and Markovian approximations. They can also often be postulated phenomenologically, based on the observation that the most general equation of motion must be a CPTP map (complete positive trace-preserving map) having Lindblad form [38].

In this section, we show the main steps of the microscopic derivation of the master equation used in chapter 4 and discuss the validity of the approximations considered. The discussion is adapted from [39], where we prove its suitability for the calculation of heat currents in the steady states of a thermal machine by comparing the cooling currents of a laser cooling protocol obtained with other methods.

The equation we use is a full Bloch-Redfield equation, obtained using the weak-coupling and Markovian approximations but without making the secular approximation. The Redfield equation does not guarantee that the eigenvalues of the reduced density matrix remain positive [40, 38]. For a system where there are no degeneracies or near-degeneracies, that issue can be cured by secularization [40, 41], which corresponds to eliminating oscillating terms in the dissipator that average to zero over time. This leads to a Lindblad form [42, 43] with positive rates. It is, however, a priori invalid for systems with near degeneracies.

Consider a Hamiltonian of an open quantum system of the form

$$H = H_S + H_B + H_{SB} \tag{2.8}$$

$$H_{SB} = \sum_k g_k O(b_k + b_k^\dagger). \tag{2.9}$$

Here H_S is the Hamiltonian for the system, H_B for its environment, or bath, and H_{SB} is the system-bath coupling. We consider the common situation in which the bath comprises a set of harmonic oscillators [38], which we index using a quantity or quantities labeled r. Note that r denotes the full set of quantum numbers required to label the modes. The oscillators have frequencies ω_r, and ladder operators b_r and $b_r^\dagger$. The displacement of the rth bath mode is coupled to the system operator O, with coupling strength g_r. The dissipative effects of the bath depend on its spectral density, $J(\omega) = \sum_r |g_r|^2 \delta(\omega - \omega_r)$.

We work in the interaction picture with respect to $H_S + H_B$, so that $O(t) = e^{iH_S t} O e^{-iH_S t}$. Note that where necessary we will distinguish operators in the interaction and Schrödinger pictures as, for example, $O(t)$ and O. From the von Neumann equation we obtain the form

$$\frac{d\rho(t)}{dt} = -i[H_{SB}(t), \rho(0)] - \int_0^t dt' [H_{SB}(t), [H_{SB}(t'), \rho(t')]] \tag{2.10}$$

where $\rho(t)$ is the full density operator of the system and environment. For weak coupling to a bath one can replace $\rho(t') \approx \rho_S(t') \otimes \rho_B(t')$ on the right-hand side, where ρ_S is the reduced density matrix of the system, and ρ_B that of the bath. Since the bath is macroscopic it can be assumed to be unperturbed by the system, and ρ_B taken to be a thermal state at inverse temperature β. For a Markovian system one may, furthermore, approximate $\rho_S(t') \approx \rho_S(t)$. We can write the coupling operator in the eigenbasis of H_S as

$$O(t) = \sum_{ij} e^{i(E_i - E_j)t} \langle i|O|j\rangle |i\rangle\langle j| \equiv \sum_{ij} \hat{O}_{ij}(t). \tag{2.11}$$

Taking the trace of Equation (2.10) over the environment's degrees-of-freedom we find

$$\begin{aligned}\frac{d\rho_S(t)}{dt} = \sum_{ij} \{ & A_{ij}[\hat{O}_{ji}(t)\rho_S(t)O(t) + O(t)\rho_S(t)\hat{O}_{ij}(t) \\ & \qquad - \rho_S(t)\hat{O}_{ij}(t)O(t) - O(t)\hat{O}_{ji}(t)\rho_S(t)] \\ & -iB_{ij}[\hat{O}_{ji}(t)\rho_S(t)O(t) - O(t)\rho_S(t)\hat{O}_{ij}(t) \\ & \qquad + \rho_S(t)\hat{O}_{ij}(t)O(t) - O(t)\hat{O}_{ji}(t)\rho_S(t)]\}.\end{aligned} \tag{2.12}$$

The quantities A_{ij} and B_{ij} are related to the the real-time Green's functions of the environment at the transition frequency $\nu_{ij} = E_i - E_j$ connecting levels i and j. The quantities A_{ij} are associated with dissipation, and are

$$A_{ij} = \pi\{[n(\nu_{ij}) + 1]J(\nu_{ij}) + n(\nu_{ji})J(\nu_{ji})\}. \tag{2.13}$$

Here $n(\nu > 0) = 1/(\exp(\beta\nu) - 1)$ is the Bose function describing the bath occupation, and $J(\nu) = 0$ for $\nu < 0$. The first term in A_{ij} corresponds to the creation of a bath quantum as the system transitions from a state i to j with $E_i - E_j > 0$, whereas the second corresponds to the absorption of a bath quantum in the opposite case, $E_i - E_j < 0$. The quantities B_{ij} are associated with energy shifts, and are given by the principal value integral

$$B_{ij} = \mathscr{P}\int J(\omega)\frac{\omega + (2n(\omega) + 1)(E_i - E_j)}{\omega^2 - (E_i - E_j)^2}d\omega. \tag{2.14}$$

Equation (2.12) can be used directly, but is often further approximated, leading to other forms of equation-of-motion for an open quantum system. One very common approximation is to drop the principal value terms proportional to B_{ij}. Another common approximation is to *secularise* the equation-of-motion. This is done by decomposing the remaining coupling operators, $O(t)$, into the energy eigenbasis: $O(t) = \sum_{kl}\hat{O}_{kl}(t)$. Every term in Equation (2.12) then involves a product of operators corresponding to two transitions, one involving the pair of levels i and j, and one involving the pair k, l. If the levels are non-degenerate these products of operators are, in general, time-dependent in the interaction picture, and average to zero. The exception is where a transition in one direction is paired with the same transition in the opposite direction, so that the time-dependence cancels out. Retaining only those terms the dissipative part of Equation (2.12) becomes

$$\frac{d\rho_S(t)}{dt} = \sum_{ij} 2A_{ij} \left(\hat{O}_{ji}(t)\rho_S(t)\hat{O}_{ij}(t) - \frac{1}{2}[\rho_S(t), \hat{O}_{ij}(t)\hat{O}_{ji}(t)]_+ \right), \tag{2.15}$$

where $[A, B]_+ = AB + BA$ is an anticommutator. This is of Lindblad form and, therefore, guarantees the positivity of the density operator. It has a straightforward physical interpretation: the environment causes transitions from the system state i to the system state j at rate $2A_{ij}$.

If the conditions are such that a rotating wave approximation can be performed in the interaction Hamiltonian — as is the case for the hot bath in the model derived in chapter 4 — the term H_{SB} in Eq. (2.8) would instead be

$$H_{SB} = \sum_q g_q(O_- x_q^\dagger + O_+ x_q). \tag{2.16}$$

Following the same steps as above and ignoring the principal value terms, we obtain

$$\begin{aligned}\frac{d\rho_s}{dt} = \pi \sum_{ij} J(\nu_{ij}) \big[n(\nu_{ij}) \big(O_{+,ij}(t)\rho_s(t)O_-(t) - O_-(t)O_{+,ij}(t)\rho_s(t) \big) \\ + (n(\nu_{ij}) + 1) \big(O_-(t)\rho_s(t)O_{+,ij}(t) - \rho_s(t)O_{+,ij}(t)O_-(t) \big) \big] \\ + J(\nu_{ji}) \big[n(\nu_{ji}) \big(O_+(t)\rho_s(t)O_{-,ij}(t) - \rho_s(t)O_{-,ij}(t)O_+(t) \big) \\ + (n(\nu_{ji}) + 1) \big(O_{-,ij}(t)\rho_s(t)O_+(t) - O_+(t)O_{-,ij}(t)\rho_s(t) \big) \big].\end{aligned} \tag{2.17}$$

2.3 Quantum thermodynamics

Statistical mechanics describes the behaviour of ensembles of particles within a probabilistic framework, addressing the system's averages, correlations, and fluctuations. In the limit of large systems — i.e, in the thermodynamic limit— thermal fluctuations are negligible and the average properties derived by statistical mechanics give rise to classical thermodynamics. Quantum thermodynamics, on the other hand, aims to describe the effects of quantum mechanics on the statistical properties at the nanoscale, with the control of energy transfer as the main target. In realistic situations, the control of a quantum system requires an understanding of the interaction with its environment. Therefore the theory of open quantum systems is an essential toolbox.

The laws of thermodynamics, valid in both classical and quantum regimes, provide fundamental restrictions to both the equilibrium and dynamics of any system. In particular, the second law of thermodynamics, together with Landauer's principle, establishes an intrinsic connection between thermodynamics and information theory. The generality of these theories gives rise to a wide realm of applications in fields such as quantum computation, nanotechnology, material science, sensing, and quantum biology [44, 45].

The first law of thermodynamics ensures the conservation of energy. It states that the change in the internal energy of a system is given by the heat Q absorbed or supplied and the work W done on or by the system

$$\Delta U = W + Q. \tag{2.18}$$

In classical thermodynamics, we call work any useful energy, however, in the quantum regime, concepts such as mechanical work are not always applicable making it more difficult to extend the definition. A broadly accepted way of differentiating heat and work is to define heat as energy exchanged irreversibly while work is always done reversibly [46]. This implies that only heat is associated with changes in entropy $S = -k_b \mathrm{Tr}[\rho \log \rho]$. With this separation in mind, we can write the average change of energy in a quantum system as

$$\frac{\partial \langle H \rangle}{\partial t} = \mathrm{Tr}\left[\frac{\partial \rho}{\partial t} H\right] + \mathrm{Tr}\left[\rho \frac{\partial H}{\partial t}\right], \tag{2.19}$$

and identify the first and second term as heat and work currents, respectively.

The second law of thermodynamics is

$$\dot{\Sigma} = \frac{\partial S}{\partial t} + \sum_j \frac{1}{k_b T_j} \frac{\partial Q_j}{\partial t} \geq 0, \tag{2.20}$$

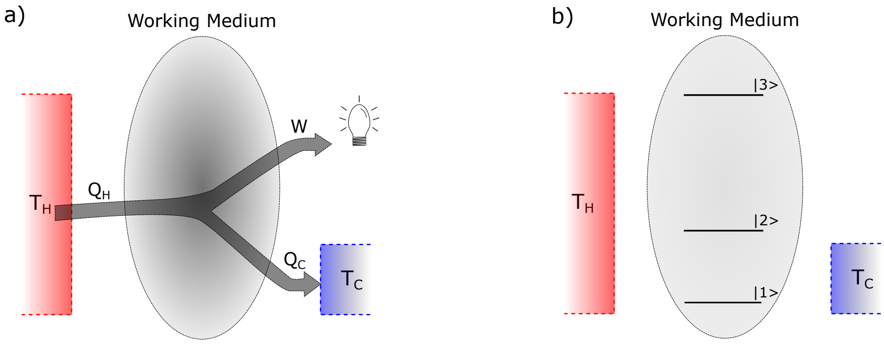

Figure 2.1: (a) Illustration of the energy flux in a heat engine. (b) Illustration of the three-level heat engine.

where $\dot{\Sigma}$ is the total entropy production, $\frac{\partial S}{\partial t}$ the entropy change in the system and $\frac{1}{k_b T_j}\frac{\partial Q_j}{\partial t}$ the entropy flow rate between the systems and the j-th bath, with temperature T_j. In the steady state the entropy change in the system vanishes, and when applied to a system coupled to a hot and a cold bath, the requirement of positive entropy production $\dot{\Sigma} \geq 0$ leads to the Carnot efficiency

$$\eta \leq \eta_c = 1 - \frac{T_c}{T_h}. \tag{2.21}$$

Where the equality holds in the reversible limit where heat is exchanged infinitely slow with the reservoirs, so the total entropy production is zero. Figure 2.1.a shows an illustrative picture of a heat engine with arrows pointing out the direction of energy flow. In the reversible limit the power output is effectively zero. It is achieved when the quotient of the temperatures is equal to the quotient of the energies exchanged with each bath $\left|\frac{Q_h}{Q_c}\right| = \frac{T_h}{T_c}$. For temperatures such that $\left|\frac{Q_h}{Q_c}\right| > \frac{T_h}{T_c}$ the thermodynamic cycle is inverted and the thermal machine operates as a refrigerator, i.e, using work to take energy from the cold to the hot reservoir. Moreover, note that the form of the second term of Eq. (2.20) leads to another way of interpreting work: the energy exchanged with a reservoir at infinite (or negative) temperature.

One of the most significant aspects of thermodynamics is its generality, meaning that the same theory can be applied to a plethora of different systems. Quantum thermal machines have been realised in a variety of systems, for example, trapped-ions [47], superconducting qubits [48], atom-cavity systems [49], quantum dots [50, 51], and optomechanical devices [52–56]. In the remainder of this section, we will first present the model of a maser as a heat engine, first introduced by Scovil and Schulz-DuBois [14] and extensively analysed in the literature [15–19]. We then describe the method of counting field statistics, used to calculate energy currents in the following chapters of the thesis.

2.3.1 Three-level heat engine

Heat engines must be composed of a working medium connected to both a hot and cold reservoir. They can operate in either cyclic strokes or in a continuous steady state. A working medium composed of a qubit operating in a steady state is equivalent to one connected to one reservoir with an intermediate temperature T ($T_c < T < T_h$) and, therefore, cannot produce work without violating the second law of thermodynamics. In a three-level system, on the other hand, the reservoirs can be coupled with levels with different energy gaps, which allows the possibility of producing an effective temperature hotter than T_h between a pair of states. As a result, the three-level system is the simplest system that can function as a working medium in a steady state [57].

Figure 2.1.b shows a schematic representation of a three-level laser as a heat engine. The first and top levels are coupled with a hot reservoir at temperature T_h and the first and middle levels are coupled with a cold reservoir at temperature T_c. We set the energy of the ground state to be zero $e_1 = 0$, and the energy of the second and third levels are e_2, and e_3, respectively. When there is no coupling between levels 2 and 3, the population of each level with respect to the ground state is given by

$$\begin{aligned} \frac{p_3}{p_1} &= \exp\left(-\frac{e_3}{k_b T_h}\right), \\ \frac{p_2}{p_1} &= \exp\left(-\frac{e_2}{k_b T_c}\right). \end{aligned} \tag{2.22}$$

The condition for lasing is a population inversion of the levels 2 and 3,

$$\frac{p_3}{p_2} = \exp\left(-\frac{e_3}{k_b T_h} + \frac{e_2}{k_b T_c}\right) \geq 1, \tag{2.23}$$

which can be rewritten as $\left|\frac{Q_h}{Q_c}\right| = \frac{e_3}{e_2} \leq \frac{T_h}{T_c}$. This is the same condition as having the thermal machine operating as a heat engine. Another way to view this connection is to think in terms of the effective temperature of the levels 2 and 3. Inversion is equivalent to having the transition coupled to a bath with negative effective temperature, which, as discussed in the last section, can be viewed as work [58].

To model the threshold behaviour of this three-level laser, we need to allow radiative decay associated with the transition between the two upper levels. The working medium is weakly coupled to the reservoirs and the emitted light, so there are no relevant energy shifts and we can use a phenomenological Lindblad approach to describe the evolution of the density matrix of the three-level system

$$\dot{\rho} = -i[H(\langle a\rangle), \rho] + \mathscr{L}_h(\rho) + \mathscr{L}_c(\rho). \tag{2.24}$$

The dissipators are

$$\begin{aligned}\mathscr{L}_\alpha(\rho) = {} & 2\gamma_\alpha^\uparrow\big(\lambda_\alpha^\uparrow \rho \lambda_\alpha^\downarrow - \frac{1}{2}(\lambda_\alpha^\downarrow \lambda_\alpha^\uparrow \rho + \rho \lambda_\alpha^\downarrow \lambda_\alpha^\uparrow)\big) \\ & + 2\gamma_\alpha^\downarrow\big(\lambda_\alpha^\downarrow \rho \lambda_\alpha^\uparrow - \frac{1}{2}(\lambda_\alpha^\uparrow \lambda_\alpha^\downarrow \rho + \rho \lambda_\alpha^\uparrow \lambda_\alpha^\downarrow)\big),\end{aligned} \tag{2.25}$$

with rates respecting detailed balance and jump operators

$$\lambda_h^\uparrow = \begin{pmatrix} 0 & 0 & 1 \\ 0 & 0 & 0 \\ 0 & 0 & 0 \end{pmatrix} \qquad \text{and} \qquad \lambda_c^\uparrow = \begin{pmatrix} 0 & 0 & 0 \\ 0 & 0 & 1 \\ 0 & 0 & 0 \end{pmatrix}. \tag{2.26}$$

In addition, $\lambda_\alpha^\downarrow = (\lambda_\alpha^\uparrow)^T$, with $\alpha = h, c$. The Hamiltonian of the system depends on the ladder operators of the field a, $a^\dagger$, in which we make a mean-field approximation

$$H = \begin{pmatrix} e_3 & g\langle a(t)\rangle & 0 \\ g\langle a^\dagger(t)\rangle & e_2 & 0 \\ 0 & 0 & 0 \end{pmatrix}. \tag{2.27}$$

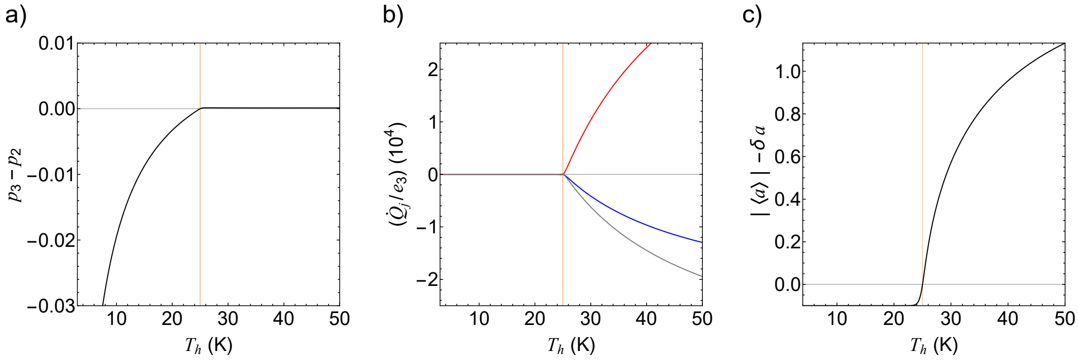

Figure 2.2: Effects of changing the temperature of the hot reservoir in the steady state of the three-level heat engine. (a) Population difference between the two excited levels. (b) Energy currents to the hot (red) and cold (blue) baths and work (black). (c) The average value of the annihilation operator of photons. We consider an initial perturbation in the occupation of photons of $\delta a = 0.1$. The parameters used in the simulation are $e_2 = 0.4\ e_3$, $\gamma^{\downarrow}_{h/c} = 0.05\ e_3$, $g = 0.3\ e_3$ and $T_c = 10$K, and the reversible limit is depicted in an orange vertical line at $T_h = 25$K.

The evolution of the working medium Eq. (2.24) is coupled to the evolution of the photons

$$\langle \dot{a} \rangle = -i(e_3 - e_2)\langle a \rangle - ig\rho_{12}, \tag{2.28}$$

where ρ_{ij} corresponds to the element ij of the density matrix and g the coupling strength of the interaction with the photon field.

Figure 2.2 shows the results of the long-time behaviour of a three-level amplifier. A state with $\langle a \rangle = 0$ and $\rho_{12} = 0$ is always a solution of Eqs. (2.24) and (2.28), therefore, we start with an initial condition slightly perturbed with $\langle a(t=0) \rangle = \delta a$. To observe the thermodynamic connection with laser emission, we consider zero photon loss, which would correspond to having the three-level heat engine inside a perfect cavity. The population inversion, the heat currents, and the number of photons are shown in Fig. 2.1 (a), (b), and (c), as a function of the hot temperature. We use the convention in which the energy currents are positive when absorbed by the three-level system, so in the heat engine mode, the hot current (red) is positive, and the cold current (blue) and output power (grey) are negative. Following the definition in Eq. (2.19), the heat and work currents are

$$\begin{aligned}\dot{Q}_\alpha &= \mathrm{Tr}[H\mathcal{L}_\alpha(\rho)],\\ P &= 2(e_3 - e_2)g\mathfrak{Im}[\langle a\rangle\rho_{21}]\end{aligned} \tag{2.29}$$

and respect the first law $P = -(Q_h + Q_c)$. Note that the power is directly connected to the coherent (off-diagonal) terms of the density matrix that emerge from the unitary interaction with photons. This is a typical result in quantum thermal machines since coherence was shown to be associated with work [59].

Above the threshold, $T_h > T_c\, e_3/e_2$, depicted as an orange vertical line, population inversion is achieved, and a thermodynamic cycle emerges with the three-level system as the working medium. The magnitude of the average field operator reflects the choice of initial perturbation; meaning that no more photons are emitted into the cavity at the normal state, but $|\langle a\rangle| > \delta a$ at the laser mode.

2.3.2 Counting field statistics

One effective way of obtaining heat currents in open quantum systems consists of introducing a variable that keeps track of the energy exchanged with the reservoirs. This method, called that of full counting statistics [60–62], involves defining an annotated density operator ρ_u such that the characteristic function of the heat distribution $P(Q,t)$ is

$$G(u,t) = \int dQP(Q,t)e^{iuQ} = \mathrm{Tr}[\rho_u(t)]. \tag{2.30}$$

Assuming a total Hamiltonian of the form Eq. (2.8) without the rotating wave approximation in the system-bath interaction the time-evolution of the annotated density operator is $\rho_u(t) = U_{u/2}\rho_u(0)U^\dagger_{-u/2}$, with annotated time-evolution operator $U_u = e^{iuH_b}Ue^{-iuH_b}$. Defining a general annotated operator O_u in the same way it obeys the Heisenberg-like equation

$$i\frac{dO_u}{du} = [O_u, H_B]. \tag{2.31}$$

This implies that the ladder operator of the bath are $b_{u,k} = e^{-i\omega_k u} b_{0,k}$. The time-evolution operators $U_{\pm u/2}$ are thus given by the usual expressions with the Hamiltonians $H^{\pm}_{SB} = \sum g_k O(b_k e^{\mp i\omega u/2} + b_k^{\dagger} e^{\pm i\omega u/2})$. Instead of the von Neumann equation, we have to solve

$$\frac{d\rho_u(t)}{dt} = -i(H^{+}\rho_u(t) - \rho_u(t)H^{-}). \tag{2.32}$$

Ignoring the principal value terms and following the steps described in section 2.2.2, we obtain a generalised master equation where the terms of the form $O\rho O$ acquire phase factors proportional to the energy difference $\nu_{ij} = E_i - E_j$

$$\begin{aligned}\frac{d\rho_{S,u}}{dt} = \pi \sum_{ij} \big\{ [(n+1)J(\nu_{ij}) + nJ(\nu_{ji})] \, [e^{iu\nu_{ij}}(O_{ji}(t)\rho_S(t)O(t) + O(t)\rho_S(t)O_{ij}(t)) \\ - O(t)O_{ji}(t)\rho_S(t) - \rho_S(t)O_{ij}(t)O(t)]\big\}.\end{aligned} \tag{2.33}$$

The moments of a distribution can be obtained with the derivatives of the characteristic function. Therefore, by definition, the average heat is

$$\langle Q\rangle = -i\left.\frac{dG(u,t)}{du}\right|_{u=0} = -i\mathrm{Tr}\left[\frac{d\rho_{u,S}(t)}{du}\right]_{u=0}. \tag{2.34}$$

Applying it to Eq. (2.33) we find

$$\begin{aligned}\frac{d\langle Q\rangle}{dt} = \pi \sum_{ij} [(n+1)J(\nu_{ij}) + nJ(\nu_{ji})] \\ \times \nu_{ij}\mathrm{Tr}[O_{ji}(t)\rho_S(t)O(t) + O(t)\rho_S(t)O_{ij}(t)].\end{aligned} \tag{2.35}$$

$$\begin{aligned}\frac{d\langle Q\rangle}{dt} = \pi \sum_{ij} J(\nu_{ij}+\omega)(\nu_{ij}+\omega)\mathrm{Tr}\big[(n+1)O_{-}(t)\rho_s(t)O_{+,ij}(t) - nO_{+,ij}(t)\rho_s(t)O_{-}(t)\big] \\ + J(\nu_{ji}+\omega)(\nu_{ji}+\omega)\mathrm{Tr}\big[(n+1)O_{-,ij}(t)\rho_s(t)O_{+}(t) - nO_{+}(t)\rho_s(t)O_{-,ij}(t)\big].\end{aligned} \tag{2.36}$$

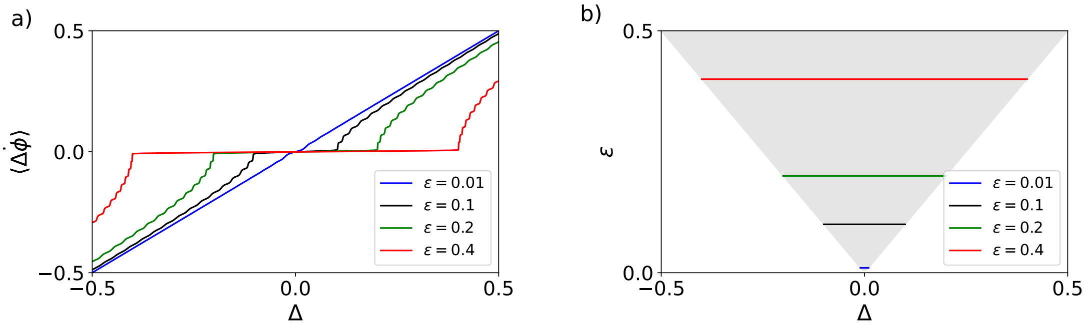

Figure 2.3: Classical synchronisation. (a) Time derivative of the phase difference of two oscillators as a function of detuning for different values of coupling strength. The oscillators are synchronised when $\dot{\Delta\phi} = 0$. (b) Phase diagram of synchronisation as a function of the coupling strength and the detuning. The synchronised region, highlighted in grey, is called Arnold's tongue.

2.4 Synchronisation of classical oscillators

Synchronisation or phase locking is a dynamic phenomenon where two or more systems oscillate at the same frequency. It has applications in many different contexts ranging from natural to social sciences [63]. A basic requirement for synchronisation is that the systems must have a closed, stable and periodic trajectory in phase space, or more specifically, they must have a limit cycle. Once each system oscillates freely, they can synchronise by adjusting the frequency with which they move along the cycle. In that way, synchronisation happens with a phase symmetry breaking, where one particular phase is preferred over the rest.

The most straightforward classical system to synchronise is a set of two weakly coupled oscillators. Their dynamics is governed by the Kuramoto model

$$\frac{d\Delta\phi}{dt} = \Delta - \epsilon \sin(\Delta\phi), \tag{2.37}$$

where $\Delta\phi$ is the phase difference of the two oscillators, Δ is the frequency difference, and ϵ the coupling strength.

Figure 2.3(a) shows the average dynamics of the evolution of the phase difference between the oscillators. The oscillators are synchronised when $\dot{\Delta\phi} = 0$, that is, when their phase difference is constant over time. The range of detunings to which the systems phase lock increases with higher values of coupling strength. Fig. 2.3(b) shows the synchronised region (shaded in grey) as a function of the coupling strength and the detuning between the oscillators. The triangular shape of the phase diagram is considered a universal signature of synchronisation known as an Arnold tongue [63]. In chapter 6, we will discuss the generalisation of this concept in the quantum regime and analyse its connection to condensation.

Chapter 3

Polariton Condensation

IN WHICH WE ARE INTRODUCED TO MICROCAVITY POLARITONS AND ANALYZE CONDENSATION USING A KINETIC THEORY

Exciton-polaritons are the result of the strong light-matter interaction in a semiconductor. Their composition brings about combined properties of both excitons and photons. In particular, having nonlinearities accompanied by small masses makes them ideal candidates for condensation.

Since the early experiments achieved polariton condensation [64], advancements in experimental techniques and theoretical understanding have enabled numerous developments. In the current state-of-art, lattices of condensates can be manipulated to research rich physics such as collective phenomena [65–68].

In this chapter, we describe a kinetic theory of photo-luminescence experiments in a semiconductor microcavity. We unravel polariton condensation in semiconductor microcavities by looking at the effects of the interaction with phonons and pairwise polariton scattering separately. The approach, using kinetic theory, is closely based on Refs. [69] and [70]. The results are similar to those obtained there, but here serve to lay the groundwork for the thermodynamic analysis presented in the following chapter.

3.1 Microcavity Polaritons

A photoluminescence experiment is a technique used to study the optical properties of materials by analyzing the light they emit after being excited by a light source. Figure. 3.1(a) shows the configuration of a semiconductor microcavity used in a photoluminescence experiment. A pair of distributed Bragg reflectors (DBRs) are placed facing each other to play the role of high-reflective mirrors with a semiconductor in the middle. The DBRs have alternating layers of high and low reflective materials that produce destructive interference of the reflected light, creating a stop band for transmission and a peak at the resonant frequency. The trapped light acquires, to a good approximation, a quadratic energy dispersion $E_c = \dfrac{\hbar^2 k_\|^2}{2m_c}$ with $k_\|$ being the component of the wave-vector parallel to the reflector's surface and m_c an effective mass.

For consistency, we consider GaAs microcavities throughout this chapter, however, all calculations are straightforward to adapt to other semiconductor microcavities. Excitation of the semiconductor leads to a bound state of an electron-hole pair, called a Wannier-Mott exciton. In the centre of the microcavity, a thin layer of a semiconductor — of thickness comparable to the exciton's Bohr radius — is placed between layers with a larger band gap, forming a quantum well. Hence, the excitons are confined to a two-dimensional surface.

The emitted light has three components: one perpendicular and two parallel to the microcavity surface. The parallel components are connected by the in-plane symmetry (we use the notation $|\mathbf{k}_{||}| = k$). Therefore, an angular measure of the emitted light provides information on energy versus wave vector, and the intensity would give the population in each emitted mode.

The top panel of Fig. 3.1(b) shows in black the dispersion curves of the cavity photons and excitons that are the relevant excitations when the light-matter coupling is negligible. In contrast to polaritons in bulk materials, the interaction strength g can be controlled by properties of the cavity design. This presents the advantage of producing fewer side effects on the quantum well material compared to other methods such as applying an external field or altering the system's temperature. When the coupling is strong, the energy of the light-matter components

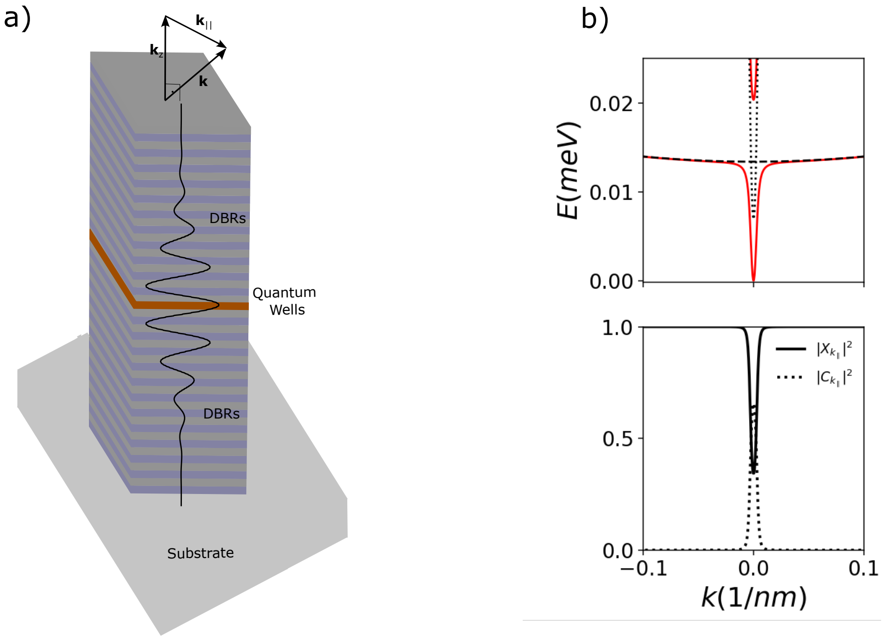

Figure 3.1: (a) Structure of a microcavity. Two Bragg mirrors formed by staggered layers of materials with high and low reflective materials are placed with layers of semiconductor quantum wells in the middle. Light is pumped into the cavity and trapped by the mirrors. The emitted light contains information on the dispersion curves and population of excitons and photons in the weak coupling light-matter regime and of polaritons in the strong coupling regime. (b) The upper graph shows the dispersion curves of the excitons (dashed) and photons (dotted) in black and of the upper and lower polaritons in red. In the lower graph, the excitonic (solid) and photonic (dotted) fractions of the lower polaritons are displayed as a function of one of the in-plane wave vectors. The exciton-photon detuning is $\Delta < 0$, hence, at $k = 0$ the lower polariton has a dominant photonic character $|C| > 1/2$, and at high momentum it is exciton. The system possesses rotational symmetry around the perpendicular axes, therefore the graphs for one of the in-plane components of **k** are sufficient to cover the physics of the two-dimensional system.

of the microcavity cannot be considered separately. The energy of the system is given by the eigenvalues of the Hamiltonian

$$H = \sum_k E_\mathrm{c}(k, k_z) a_k^\dagger a_k + E_\mathrm{ex}(k) b_k^\dagger b_k + g(a_k^\dagger b_k + b_k^\dagger a_k), \tag{3.1}$$

where a_k and b_k are the annihilation operators of a photon and exciton with in-plane wave vector k.

We diagonalize Eq. 3.1 by defining new operators as a weighted sum of the photon and exciton annihilation operators

$$\begin{aligned} p_k &= X_k b_k + C_k a_k \\ q_k &= -C_k b_k + X_k a_k, \end{aligned} \tag{3.2}$$

where the weights X_k and C_k are complex numbers called Hopfield coefficients. It is straightforward to show that because a_k and b_k obey bosonic commutation relations, so do p_k and q_k. The Hamiltonian becomes that of two free particles, namely the upper and lower polaritons

$$H = \sum_k E_{\mathrm{lp}} p_k^\dagger p_k + E_{\mathrm{up}} q_k^\dagger q_k. \tag{3.3}$$

The dispersion curves show an avoided crossing between the exciton and photon energy. They are given by

$$E_{\mathrm{up,lp}}(k) = \frac{1}{2}(E_{\mathrm{c}}(k, k_z) + E_{\mathrm{ex}}(k) \pm \frac{1}{2}\sqrt{\Delta E(k)^2 + 4g^2}, \tag{3.4}$$

and are depicted in red in Fig. 3.1. The Hopfield coefficients that diagonalize the Hamiltonian are

$$|X_k|^2 = \frac{1}{2}\left(1 + \frac{\Delta E(k)}{\sqrt{\Delta E(k)^2 + 4g^2}}\right) \quad \text{and} \quad |C_k|^2 = \frac{1}{2}\left(1 - \frac{\Delta E(k)}{\sqrt{\Delta E(k)^2 + 4g^2}}\right), \tag{3.5}$$

where $\Delta E(k) = E_{\mathrm{c}}(k, k_z) - E_{\mathrm{ex}}(k)$, and $|X_k|^2 + |C_k|^2 = 1$.

The composition of the lower polaritons is shown in the bottom graph of Fig. 3.1(b), with X_k and C_k being the excitonic and photonic fraction, respectively. At large momentum, the lower polaritons are almost entirely excitons. However, near the ground state, they acquire a higher photonic fraction, with a degree of mixture that depends on the detuning of the bare particles at $k = 0$. We define the exciton-photon detuning $\Delta = \Delta E(k = 0)$.

The hybrid nature of polaritons provides them with a rich combination of characteristics. Excitons have a mass approximately 10^4 times larger than the cavity photon, as revealed by the difference in the curvature of the dispersion curves. This implies a stark difference ($\sim 10^4$) in the value of the density of states of polaritons with a non-negligible photonic fraction when compared to excitons. Hence, while the exciton component allows pairwise scattering of polaritons and consequently a non-linear behavior, the photonic component inhibits such effects. On the other hand, even though the photonic character reduces the probability of interactions which increases the thermalization time, the low mass of the photons is a facilitator for condensation since the critical temperature is inversely proportional to the mass (see chapter 2). Moreover, the small lifetime of the cavity photons (a few picoseconds) is an obstacle to full thermalization, making it an out-of-equilibrium system.

3.2 Kinetics of polariton condensation

One of the early works on polaritons suggested that they could be used as a potential source of coherent light [71]. The idea consisted of using stimulated polariton-phonon scattering to generate a buildup of population on the ground state, and, consequently, coherent emission. This was expected to result in relaxation by emission of acoustic phonons through the lower energy states, forming a non-equilibrium condensate that would act as a laser without the need for population inversion between conduction and valence bands. Nonetheless, the actual picture is not so simple: kinetic simulations show that phonon emission is not sufficient to generate a macroscopic occupation in the ground state, which can be explained by the density of states [37]. At present, the polariton-polariton interaction is known to be the main mechanism to promote the occupation of the low energy polariton modes [72, 73, 8]. However, the details of how to treat this interaction are not completely lighted on [74, 75].

Kinetic equations have been shown to be a strong tool to approach polariton condensation [76–82, 70]. In this section, we use this well established framework to simulate the dynamics and steady-state distribution of a polariton gas. We consider a non-equilibrium system, with radiative decay and an external pump, and study the role of each interaction in the condensation process.

To simulate the population dynamics of a polariton gas we use a Boltzmann equation (2.6) and include a pump term $P_k(t)$ and radiative losses $n_{\mathbf{k}}\Gamma_k$

$$\frac{\partial n_{\mathbf{k}}}{\partial t} = P_{\mathbf{k}}(t) - n_{\mathbf{k}}\Gamma_{\mathbf{k}} + \sum_{\mathbf{k'},\mathbf{s}} W^{(s)}_{\mathbf{k}\to\mathbf{k'}}(t) - W^{(s)}_{\mathbf{k'}\to\mathbf{k}}(t), \tag{3.6}$$

where n_k is the occupation number of the state k. Here a rotational symmetry allows the replacement of the wave vector by its norm $|\mathbf{k}| = k$. The Ws represent the scattering processes into and out of the k-th mode due to the s-th interaction.

3.2.1 Polariton-phonon interaction

We start our analysis by taking only phonon scattering, pump, and decay into consideration and reproduce the calculations in [69, 73]. The polariton-phonon interaction happens via emission and absorption, therefore, for a polariton with in-plane wave vectors k_0 and a phonon with $q_\parallel$, four processes are possible

1. $\mathbf{k_0} \to \mathbf{k_1} + \mathbf{q}_\parallel$,
2. $\mathbf{k_0} + \mathbf{q}_\parallel \to \mathbf{k_1}$,
3. $\mathbf{k_1} + \mathbf{q}_\parallel \to \mathbf{k_0}$,
4. $\mathbf{k_1} \to \mathbf{k_0} + \mathbf{q}_\parallel$.

The processes $1, 2$ $(3, 4)$ are the out(in)-scattering terms for a polariton with wave vector k_0, which are inverse of each other and consequently have the same equations of energy and momentum conservation. This symmetry is used as a check on the numerical calculation. Applying Fermi's golden rule, Eq. (2.7),

$$\begin{aligned}\left.\frac{\partial n_{\mathbf{k_0}}}{\partial t}\right|_{\text{pol-ph}} &= \frac{2\pi}{\hbar}\sum_{\mathbf{k_1},\mathbf{q}} |M|^2 \big\{ \left[(1+n_{\mathbf{k_0}})n_{\mathbf{k_1}}N_{\mathbf{q}} - n_{\mathbf{k_0}}(1+n_{\mathbf{k_1}})N_{\mathbf{q}}\right]\delta(E_0 + \hbar u|\mathbf{q}| - E_1) \\ &+ \left[(1+n_{\mathbf{k_0}})n_{\mathbf{k_1}}(1+N_{\mathbf{q}}) - n_{\mathbf{k_0}}(1+n_{\mathbf{k_1}})(1+N_{\mathbf{q}})\right]\delta(E_0 - \hbar u|\mathbf{q}| - E_1)\big\},\end{aligned} \tag{3.7}$$

where $M = M(k_0, k_1, q)$ is the matrix element of the interaction, and N_q the number of phonons in the state $q_\parallel$. The first two terms correspond to the processes 1 and 3, and the last two to 2 and 4. Taking the thermodynamic limit, we convert the sum into an integral and get, for process 1

$$\begin{aligned}\frac{\partial n(E_0)}{\partial t} &= \frac{D(E)}{\rho u_l 16\pi^2} dE_0 \int_0^{E_0} dE_1 \int d\theta_1 \frac{X_{k_0} X_{k_1} (E_0 - E_1)^2}{\frac{\partial E_1}{\partial (k_1^2)} (\hbar u_l)^3} \\ &\times \frac{\left[a_e I_e^{\|}(\mathbf{q}) I_e^{\perp}(a) - a_h I_h^{\|}(\mathbf{q}) I_h^{\perp}(a)\right]^2}{\sqrt{\frac{(E_0-E_1)^2}{(\hbar u_l)^2} - |\mathbf{k_0} - \mathbf{k_1}|^2}} f(E_0)[1 + f(E_1)][1 + F(|E_0 - E_1|)],\end{aligned} \tag{3.8}$$

for the longitudinal acoustic phonons, and

$$\begin{aligned}\frac{\partial n(E_0)}{\partial t} &= \frac{D(E)}{\rho u_{tr} 16\pi^2} dE_0 2 \int_0^{E_0} dE_1 \int d\theta_1 \frac{X_{k_0} X_{k_1} (E_0 - E_1)^2}{\frac{\partial E_1}{\partial (k_1^2)} (\hbar u_{tr})^3} \\ &\times \frac{\left[\Xi_e I_e^{\|}(\mathbf{q}) I_e^{\perp}(a) - \Xi_h I_h^{\|}(\mathbf{q}) I_h^{\perp}(a)\right]^2}{\sqrt{\frac{(E_0-E_1)^2}{(\hbar u_{tr})^2} - |\mathbf{k_0} - \mathbf{k_1}|^2}} f(E_0)[1 + f(E_1)][1 + F(|E_0 - E_1|)]\end{aligned} \tag{3.9}$$

for the transverse acoustic phonons. The rates for the other three processes can be calculated analogously, by substituting the appropriate statistical factors. The integration limits are given by the requirement of energy and momentum conservation. The variables Ξ_e, Ξ_h, a_e, and a_h, are the electron and hole effective deformations potentials, and u_l and u_{tr} are the phonon speed of sound. The numerical values of these parameters are given in [73]. A factor of 2 is added in Eq. (3.9) to account for the possible directions of polarization of the transverse phonon.

In Eqs. (3.8) and (3.9) the scattering rates are in terms of the occupation of energy. This is $n(E) = f(E)D(E)dE$, where $f(E) = f(E(k)) = n_k$ is the occupation number per state. The density of states $D(E)$ depends on the curvature of the dispersion curve and is such that

$$D(E)dE = \frac{S}{2\pi} \left(\frac{\partial E}{\partial (k^2)} \right)^{-1} dE \tag{3.10}$$

is the number of states with energy between E and $E + dE$, and S the area.

To simulate the population dynamics, we discretize both time and the energy

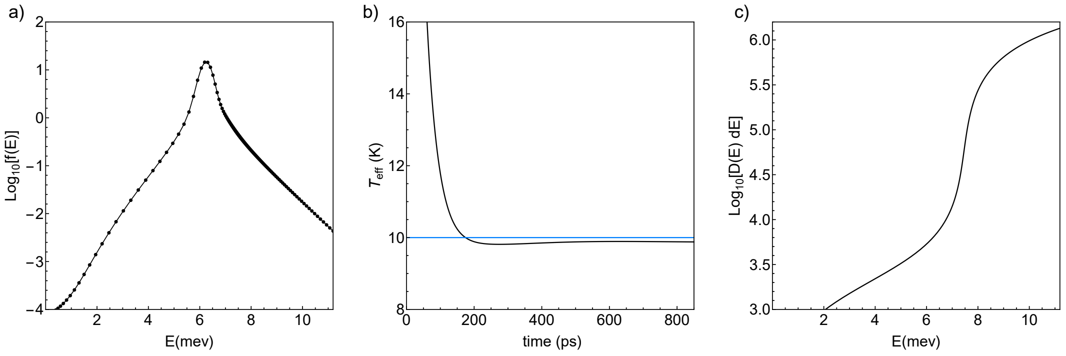

Figure 3.2: Simulation of the Boltzmann equation considering radiative decay, polariton-phonon scattering, and a energy independent pump. The initial condition is the same as the pump. (a) Steady-state distribution has a thermal tail on the excitonic branch of the polariton states, an accumulation of particles in the bottleneck region, and a small occupation of the polariton states with low energy. (b) The exciton effective temperature approaches the lattice temperature (10K) in the steady state. The final temperature for the time interval shown is 9.87K. (c) The density of states as a function of energy shows a stark change of many orders of magnitude for states from excitonic states to low-energy states. The parameter region of transition corresponds to the bottleneck region.

space and iterate the populations with an interval Δt chosen so that

$$\text{Max}\left[\frac{\Delta f(E)}{f(E)}\right] = 0.01. \tag{3.11}$$

The energy bins must be considerably smaller than the average energy exchanged and the rate of change in the distribution. We follow the discretization choice in [73] and consider a pump that generates a constant population over the polariton states. However, the particular shape of the generation of particles has been shown to have little importance [8]. This is consistent with what is expected of a thermalization process, where irreversibility implies independence of the initial conditions. Even though the losses prevent a full thermalization of polariton, we still expect it to act as a source of irreversibility. The decay rate of each mode is given by the lifetime of its components weighted by Hopfield coefficients

$$\Gamma_k = \frac{|C_k|^2}{\tau_c} + \frac{|X_k|^2}{\tau_{ex}}. \tag{3.12}$$

τ_c and τ_{ex} are the photon ($\sim$ 5ps) and exciton ($\sim 10^6$ps) lifetimes.

Fig. 3.2(a) shows the steady state distribution of a simulation taking polariton-phonon scattering as the only interaction. The results agree with [73]. The scenario is unrealistic but shows the role played by phonons. Polaritons with energy below 7 meV have a non-negligible photonic fraction and are not able to overcome the radiative losses to thermalize. This is attributed to the small density of states inherited from their photonic component, seen in Fig. 3.2(c). The peak of occupation happens in the called “bottleneck” region of the dispersion, where the transition from high to low density of states happens [37]. A portion of the higher energy polaritons acquires a thermal distribution with effective temperature displayed in Fig. 3.2(b). The time required for the thermalization is approximately 400ps, and the final temperature approaches the lattice temperature (blue line) from below.

3.2.2 Polariton-polariton interaction

Polariton-polariton scattering rates can be calculated from Fermi’s golden rule analogously to the phonon scattering rates. However, we follow the simplified approach derived in [70] with small changes to capture the physics of GaAs microcavities instead of the CdTe. These authors had argued that with only phonon and polariton-polariton scattering, condensation in GaAs would require a density near saturation $n_{\text{sat}} = 1.3 \times 10^{11}\text{cm}^2$. This would imply that other means of relaxing to lower states, such as electron scattering, for example, must be taken into account to explain condensation in these systems, which occurs at densities well below saturation. Here we consider a microcavity with 10 quantum wells to show that condensation can be justified as an effect of polariton-polariton interaction. The saturation density increases directly with the number of quantum wells and the inter-particle scattering is altered as discussed below.

The approach takes into consideration two separate regions of the polariton dispersion: an excitonic region where $E > E_{\text{ex}}(k = 0)$ is considered to possess a thermal distribution with a varying temperature T_x and density n_x, and a polariton region whose dynamics is affected by the pair-wise scattering of the excitons in the first region and by radiative decay. This corresponds to assuming that the exciton thermalization time is rapid in comparison with the polariton relaxation time. The polariton population dynamics is given by

$$\frac{dN_k^{\mathrm{lp}}}{dt} = W_k^{\mathrm{in}} n_x^2 \left(1 + N_k^{\mathrm{lp}}\right) - W_k^{\mathrm{out}} n_x N_k^{\mathrm{lp}} - \Gamma_k^{\mathrm{lp}} N_k^{\mathrm{lp}} \tag{3.13}$$

and the density in the exciton reservoir is altered by pair-wise scattering $W^{\mathrm{in/out}}$, radiative losses and a pump p_x

$$\frac{dn_x}{dt} = -\frac{1}{S}\sum_k dg_k^{\mathrm{lp}} \left(W_k^{\mathrm{in}} n_x^2 \left(1 + N_k^{\mathrm{lp}}\right) - W_k^{\mathrm{out}} n_x N_k^{\mathrm{lp}}\right) - \Gamma_x n_x + p_x. \tag{3.14}$$

N_k^{lp} is the occupation number of the state k, dg_k^{lp} the degeneracy of each state, Γ^{lp} and Γ_x are the polariton and exciton decay rates and p_x is the pump. We have assumed that the occupation of the exciton states is considerably smaller than one.

The exciton temperature is related to the energy density in the reservoir

$$e_x(t) = n_x(t) k_B T_x(t), \tag{3.15}$$

that depends on the same factors as the exciton density in addition to losses through phonon relaxation

$$\begin{aligned} \frac{de_x}{dt} = &-\frac{1}{S}\sum_k e_k^{lp} dg_k^{lp} \left(W_k^{\mathrm{in}} n_x^2 \left(1 + N_k^{\mathrm{lp}}\right) - W_k^{\mathrm{out}} n_x N_k^{\mathrm{lp}}\right) + \frac{\rho_x}{2\pi}\sum_i \Delta E e_i^x \left.\frac{dN_i^x}{dt}\right|_{\mathrm{ph}} \\ &+ p_x k_B T_L - \Gamma_x n_x k_B T_x, \end{aligned} \tag{3.16}$$

where the ΔE is the size of the energy grid in the exciton region and we assumed that the pump generates excitons with a thermal distribution with the lattice temperature T_L. The scattering rates $W^{\mathrm{in/out}}$ must consider the Coulomb interaction and saturation effects and, therefore are effectively described as exciton-exciton and exciton-photon interaction. We use the expressions

$$\begin{aligned} W_k^{\mathrm{in}} &= \frac{2\pi}{\hbar k_b T_x} M_k^2 e^{e_k^{lp}/k_b T_x} \\ W_k^{\mathrm{out}} &= \frac{M_k^2}{\hbar} \rho_x e^{2e_k^{lp}/k_b T_x} \end{aligned} \tag{3.17}$$

derived in [70] with $M_k = M_{xx} X_k + \sigma_{\mathrm{sat}} C_k$, however, we use a more updated

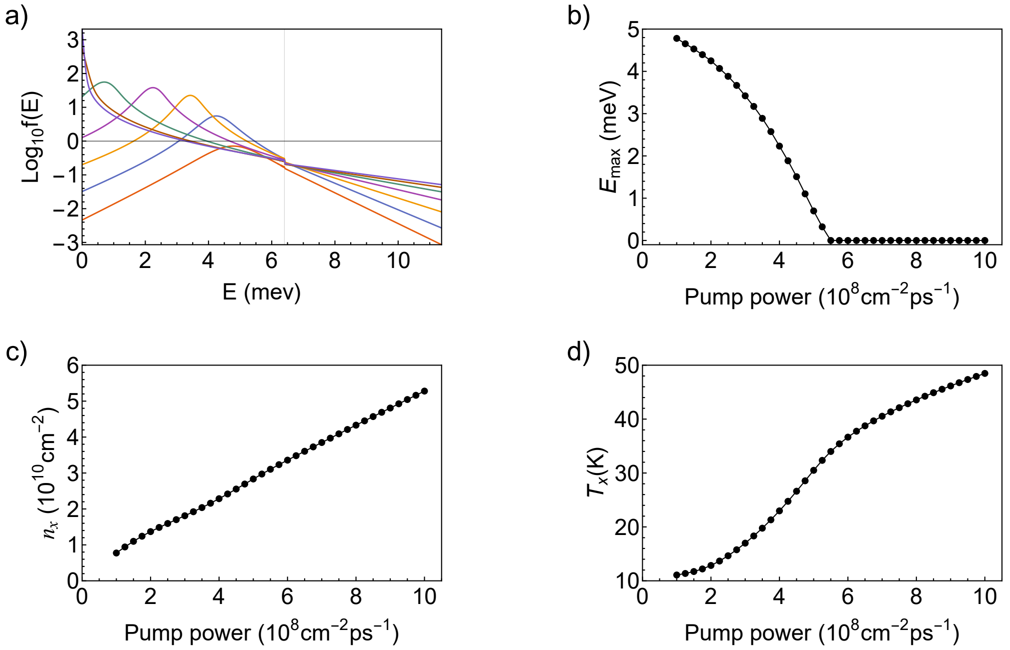

Figure 3.3: Polariton dynamics in GaAs microcavities using the model proposed in [70]. (a) Steady-state polariton distribution for pumps of $(1-7)\ 10^8\text{cm}^{-2}\text{ps}^{-1}$. The vertical line indicates the boundary of the exciton reservoir. (b) The energy at which the peak of polariton distribution is located for different values of p_x. The threshold of condensation at the ground state is $p_x \approx 5.5 \times 10^8\text{cm}^{-2}\text{ps}^{-1}$. The sub-figures (c) and (d) show the exciton density and temperature as a function of the pump. The exciton density grows linearly with the pump power and does not reach saturation, however, the temperature acquires a smaller slope after the condensation threshold.

expression for the matrix elements of the interaction [74] and take the number of quantum wells N_{qw} into consideration

$$\begin{aligned} M_{xx} =& \frac{6E_B a_b^2}{2N_{qw}} \\ \sigma_{\text{sat}} =& \frac{32\pi}{7N_{qw}} g a_b^2. \end{aligned} \tag{3.18}$$

The values of binding energy E_B and Bohr radius a_b for GaAs and the bare exciton density of states ρ_x are the same as in the last section, taken from [73].

In Fig. 3.3(a) we show the steady state distribution of population for different pump rates. The higher the pump rate, the higher the peak of the distribution, and the lower the energy of the peak. Above the pump threshold, the peak is at the ground state, which becomes microscopically occupied. This behavior is qualitatively consistent with the results obtained by the same model for CdTe microcavities and with experimental observations [72]. Figure 3.3(b) shows the energy of the peak of the distribution for different pump values, indicating that the threshold is at $p_x \approx 5.5 \times 10^8 \mathrm{cm}^{-2}\mathrm{ps}^{-1}$.

The density of excitons, shown in Fig 3.3(c), grows linearly with the pump for all values considered and does not reach saturation. The dependence of the temperature on the pump changes after the threshold, acquiring a smaller slope. In that case, the pairwise exciton scattering is comparable to the exciton radiative recombination, meaning the two factors add up as loss mechanisms in the exciton reservoir.

3.3 Discussion

In this chapter, we have investigated the dominant interactions in a polariton gas and looked at how the different parts of the dispersion branch respond to each of them. In conclusion, the polariton branch can be divided into three: excitons, bottleneck polaritons, and low-energy polaritons. The excitons interact rapidly with the phonons and with each other, relaxing to a thermal distribution. The low-energy polaritons, on the other hand, have a small density of states, which implies smaller relaxation rates. Therefore, the thermalization of this part of the distribution is conditioned to either a longer cavity lifetime or a large in-scattering rate of particles resulting from the interaction between bottleneck polaritons and excitons.

The results presented in this chapter illustrate the fundamental function of each component of the system. The phonons act as a cold reservoir that extracts energy from the polariton gas. The bottleneck polaritons, interacting with excitons, are responsible for populating the condensate mode. The pump adds energy and particles to the gas, not only enabling a non-trivial steady state but also generating the particle number needed to stimulate the polariton-exciton interaction. In the next chapter, this picture will be used as a base for the development of a few-level polariton model and its thermodynamic interpretations.

Other physical mechanisms that could affect polariton condensation, such as electron interaction and piezoelectric phonon effects, have been considered in the literature, but for semiconductor microcavities were proved to be small when compared to the interactions we considered [73]. Interactions with particles in the upper polariton branch are also a small possibility and so are not considered in our calculation.

Additionally, there are non-linear effects caused by the polariton-polariton interaction, which include a blue shift and phase-filling effects. The first is a shift in the energy of the polariton modes caused by their excitonic component and neglected in our calculations. The second, included in Eq. (3.18), is a saturation effect inherited from the fermionic nature of the fundamental components excitons, i.e., electrons and holes. This correction can be used up to a certain density, however, if the average de Broglie wavelength of the particles is comparable to their average separation distance the Boltzman equation is no longer a valid approximation [34].

Chapter 4

Thermodynamics of Polariton Condensates

IN WHICH WE MODEL A POLARITON GAS AS A
QUANTUM THERMAL MACHINE

The kinetic approach, used in the last chapter, has served as the groundwork for the analysis of polariton condensation in many different experimental settings and contexts [80, 81, 83–86]. Although developing a theory that precisely accounts for experimental specifics is crucial, the multitude of details can obscure the identification of the core requirements for condensation. In this chapter, we suggest a universal description of non-equilibrium condensation as the output of a thermal machine. We show how condensation can be described using a three-level laser model, whose connection to the thermodynamics of heat engines, first pointed out by Scovil and Schulz-DuBois, has been extensively studied [14–19]. We base our model on the collection of knowledge provided by theoretical and experimental works and the results of the preceding chapter.

Our approach restricts condensation into a minimal model allowing the extraction of fundamental thermodynamic constraints of the system, such as the Carnot limit. We investigate properties such as efficiency, and determine the conditions required for condensation. An important result is that the occurrence of condensation is determined by two temperatures whose difference controls the direction of energy flow in the system, governing the formation of the condensate, and allowing the losses to be overcome. Our work further clarifies that non-equilibrium condensation requires a population inversion, albeit of an unconventional kind, and emphasizes the need for an effective coupling to a cold reservoir. This last requirement – the need for a rapid depopulation of the lower state – is well known in the context of lasers, but is rarely explicit in the literature on driven-dissipative condensates.

The thermodynamics of three-level amplifiers has been studied before, and our main contribution is to apply these results to driven-dissipative condensation. However, this application does require two extensions of the general framework. Firstly, we consider not just amplification, but the balance of gain and loss in the full system comprising a condensate driven by a gain medium. This allows us to compute non-equilibrium phase diagrams and study how thermodynamic quantities such as efficiency vary across them. Secondly, we allow for the possibility that the thermal machine operates between reservoirs at different chemical potentials, as well as different temperatures, implying that it absorbs work as well as heat. This is necessary in practice for driven-dissipative condensates, as discussed below, but also relevant in cases such as electrically-driven lasers, where the voltage bias is a source of work.

4.1 Condensates as heat engines

Driven-dissipative condensates are typically understood as open quantum systems, in which energy from an incoherent pump reservoir is converted into a coherent condensate, which is in turn emitted into an environment. As discussed further below, we argue that if the pump is an incoherent source it corresponds to a heat bath, while the coherent emission from the condensate is a source of work. With these identifications we identify the basic form of condensate as a heat engine, converting heat, from the pump, into work. It follows immediately, as a consequence of the second law of thermodynamics, that a consistent description of condensation requires consideration of a cold reservoir, in addition to the hot reservoir representing the pump. Note that in the following we extend these considerations to allow the pump to provide work, as well as heat.

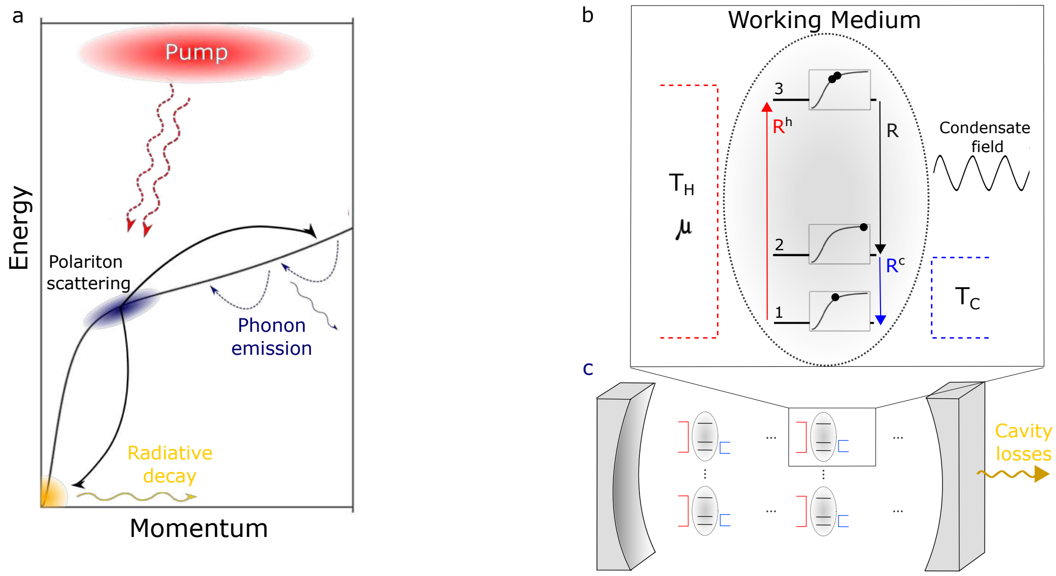

Figure 4.1: (a) Illustration of the main processes that lead to condensation of inorganic microcavity polaritons. A non-resonant pump creates excitons that relax to lower energy states through phonon emission. Pair-wise polariton scattering leads to occupation in the lower energy modes if it can overcome radiative losses. (b) The condensation process is modeled as the outcome of a three-level heat engine with a hot bath connecting the ground state and the most energetic state and a cold bath connecting the ground state to the middle state. The condensate is a classical field interacting with the two excited states of the working medium. The rectangles on the top of each level show the corresponding states in the dispersion curve. The first and third levels correspond to $n-1$ and n polaritons in the bottleneck, respectively. The middle level corresponds to a state with a high energy exciton. (c) Model of a microcavity comprising M three-level systems that contribute to the growth of the condensate, which competes with loss due to the finite polariton lifetime.

To develop this idea further, we construct a few-level model of condensation. As illustrated in Fig. 4.1(a), particles are created by a high-energy pump, which produces electron-hole pairs that populate the exciton states at high momentum. This population quickly begins to thermalize with the emission of acoustic phonons [71], but such scattering becomes ineffective for the polaritonic final states at low energy and momentum. As confirmed by the kinetic simulations in the previous chapter and previous works [32, 36, 64, 73, 8, 80–82, 70, 84, 87–89], this bottleneck effect [37] can be overcome by polariton-polariton scattering. If the density is large enough this scattering into low-energy states can exceed their loss. It then becomes a stimulated process which leads to condensation [90].

To determine the thermodynamic constraints on condensation we consider a minimal model, consisting of a heat engine whose working medium is a three-level system with energies e_1, e_2, and e_3. We discussed in chapter 2 that this is the simplest possible case [57]. As shown in Fig. 4.1(b), we suppose that the highest energy state of the working medium, $|3\rangle$, corresponds to a population of n polaritons in the bottleneck region. These can undergo pairwise scattering, adding one particle to the condensate and promoting one polariton to a higher-energy exciton state. Due to the macroscopic occupation of the condensate mode, such stimulated scattering can be treated as an interaction with a condensate field external to the working medium. It takes the latter to an intermediate state, $|2\rangle$, that has a particle in a high energy state. The high-energy exciton can then transition back to the bottleneck region by phonon emission, leading to the state $|1\rangle$ with bottleneck population $n-1$. In the terminology of the polariton parametric oscillator [90], the populated bottleneck states are the pump states and the high-energy exciton state generated by pairwise scattering is the idler.

The three-level working medium drives the polariton condensate, which we treat as a classical mean field. The relevant Hamiltonian is

$$H_s = g_c(p_c^\dagger p_i^\dagger p_p p_p + p_c p_i p_p^\dagger p_p^\dagger), \tag{4.1}$$

where p_c, p_p, and p_i are the annihilation operators for particles in the condensate state, pump state, and idler state, respectively, and g_c is the interaction strength. We consider a macroscopically occupied condensate mode and approximate $g_c p_c \approx g_c\langle p_c\rangle = e^{-i\omega t}\Omega/2$, where ω is the condensate frequency, and for a condensate of N particles

$$\Omega = 2g_c\sqrt{N}. \tag{4.2}$$

In the basis of the three-level system, the final three terms in each product in Eq. (4.1) become transition operators $p_i^\dagger p_p p_p = |2\rangle\langle 3|$, and the Hamiltonian for the scattering process reduces to that of the three-level system driven by a field corresponding to the condensate,

$$H_s = \frac{\Omega}{2}\big(e^{-i\omega t}\,|3\rangle\langle 2| + e^{i\omega t}\,|2\rangle\langle 3|\big). \tag{4.3}$$

This implies that the energy transfers between the three-level system and the condensate are work, in accordance with the standard partition of energy currents in Eq. (2.19) in which work arises from the time-dependence of a Hamiltonian and heat from that of the density-matrix. Using this along with Eq. (4.3), the power supplied to the condensate is

$$\begin{aligned}\langle \dot{W} \rangle = \left\langle \frac{\partial H_s}{\partial t} \right\rangle &= \omega\Omega\mathfrak{Im}\left\{\mathrm{Tr}[\rho e^{i\omega t}\left|2\right\rangle\left\langle 3\right|]\right\} \\ &= \omega\Omega\mathfrak{Im}\rho_{32},\end{aligned} \tag{4.4}$$

where ρ_{32} is an element of the density matrix in the time-dependent basis introduced below.

Additionally, the three-level system exchanges energy and particles with a reservoir of acoustic phonons and a reservoir of excitons that is generated by the pump. The phonons act as the cold bath of the heat engine, extracting heat from the working medium as the excitons relax to the bottleneck ($\left|2\right\rangle \rightarrow \left|1\right\rangle$). The excitons generated by the external pump act as the hot bath. To stay within the framework of a three-level model we suppose they feed the states at the bottleneck, causing transitions from $\left|1\right\rangle$ to $\left|3\right\rangle$. The lifetime of a reservoir exciton is relatively long, so that the hot reservoir forms a quasi-equilibrium state with temperature T_h and chemical potential μ. This means that the heat engine operates with a chemical potential drop between the hot and cold reservoirs. Since particles flow through the engine across this chemical potential drop, its energy input consists of both work and heat.

In summary, the thermal machine operates in a mode in which the hot reservoir inputs work and heat into the three-level system, which performs work by interacting with the condensate and emits the rest of the energy into a cold bath of phonons. Combining the free Hamiltonian of the three-level system, the coupling to the condensate, and the coupling to the baths, we have

$$\begin{aligned}H_0 + H_{sb} = e_3\left|3\right\rangle\left\langle 3\right| + e_2\left|2\right\rangle\left\langle 2\right| + e_1\left|1\right\rangle\left\langle 1\right| + \frac{\Omega}{2}\big(e^{-i\omega t}\left|3\right\rangle\left\langle 2\right| + e^{i\omega t}\left|2\right\rangle\left\langle 3\right|\big) \\ + \sum_k g_k^{\mathrm{ph}}\big(\left|1\right\rangle\left\langle 2\right| + \left|2\right\rangle\left\langle 1\right|\big)(b_k + b_k^\dagger) \\ + \sum_q g_q^{\mathrm{p}}\big(\left|3\right\rangle\left\langle 1\right| + \left|1\right\rangle\left\langle 3\right|\big)(x_q + x_q^\dagger).\end{aligned} \tag{4.5}$$

The energies $e_{1,2,3}$, which we refer to as the bare states are depicted in Fig. 4.2(a), and are the energy of the system when the field is turned off. The second and third lines of Eq. (4.5) represent the interactions with the cold and hot baths, with coupling strengths g_k^{ph}, and g_q^{p}, and annihilation operators b_k and x_q, respectively. In the present case, they refer to phonons, and excitons in states which repopulate the bottleneck. One could also consider, in addition to the process where a pump-generated exciton transfers into a bottleneck state, one in which it transfers into the higher-energy state, which then relaxes to the bottleneck by phonon emission. This could be incorporated by using a four-level model, with an additional state $|4\rangle$, representing the state with an additional high-energy exciton, which then relaxes to $|3\rangle$ by phonon emission. Such a model could be further extended to include higher phonon states, giving a form similar to that used for photon condensation by Kirton and Keeling [5]. However, inclusion of these additional pathways would not be expected to qualitatively affect our results, because under reasonable conditions the reservoir population will decrease with increasing energy, so that the strongest effect of repopulating the bottleneck comes from the process we consider.

We eliminate the time dependence of Eq. (4.5) by using the rotating frame with the condensate frequency $(|1_R\rangle, |2_R\rangle, |3_R\rangle) = (|1\rangle, |2\rangle, e^{-i\omega t}|3\rangle)$, which leads to

$$\begin{aligned} H_0' + H_{sb}' = {} & (e_2 + \Delta)\,|3_R\rangle\langle 3_R| + e_2\,|2_R\rangle\langle 2_R| + e_1\,|1_R\rangle\langle 1_R| \\ & + \frac{\Omega}{2}\big(\,|3_R\rangle\langle 2_R| + |2_R\rangle\langle 3_R|\,\big) \\ & + \sum_k g_k^{\mathrm{ph}}\big(\,|1_R\rangle\langle 2_R| + |2_R\rangle\langle 1_R|\,\big)(b_k + b_k^\dagger) \\ & + \sum_q g_q^{\mathrm{p}}\big(\,|3_R\rangle\langle 1_R|\,x_q + |1_R\rangle\langle 3_R|\,x_q^\dagger\big). \end{aligned} \tag{4.6}$$

The transformation to this rotating basis would produce a time dependence in the coupling to the hot bath, which, however, has been removed by transforming to an interaction picture with respect to a Hamiltonian $\sum_q \omega x_q^\dagger x_q$, and making the rotating wave approximation in the system-reservoir coupling. The detuning $\Delta = (e_3 - e_2) - \omega$ corresponds to the energy difference between the low-energy final state of the scattering and the condensate. The energy levels given by the

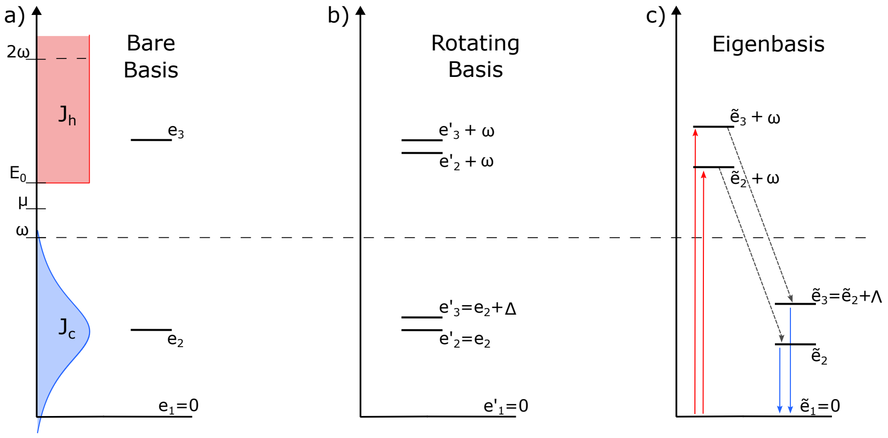

Figure 4.2: Energy diagram of the three-level system in the three different bases, and the spectral densities of the hot and cold bath. (a) The energy levels, e_i, in the bare basis when the field is turned off. Correspond to the ones shown in Fig. 1. (b) When the Hamiltonian is transformed into a rotating basis its time dependence is lost, however, the states acquire a periodicity in energy. Two Floquet zones are included (e_i') in the diagram. (c) The interaction with the condensate field mixes the states of the rotating basis to produce eigenstates with energies ($\tilde{e}_2, \tilde{e}_3$), split by $\Lambda = \sqrt{\Delta^2 + \Omega^2}$. These states are replicated in the two Floquet zones. The red and blue arrows indicate transitions due to the hot and cold baths respectively (see text).

first three terms of this Hamiltonian are depicted in Fig.4.2(b). We note that, as the energies of a periodically-driven system, they are defined up to multiples of the driving frequency ω. We define the zero of energy to be $e_1 = 0$. For the other energies, we use values representative of a GaAs microcavity, $e_2 = 5$ meV and $e_3 - e_2 = 1$ eV.

4.2 Methods

To analyze Eq. (4.6) we use the standard method, previously applied to a three-level heat engine in [17], in which one transforms to the eigenbasis of H_0' and eliminates the heat baths within the Born-Markov approximation. The transformation to the eigenbasis of H_0' is effected by the rotation

$$\begin{pmatrix} |\tilde{3}_R\rangle \\ |\tilde{2}_R\rangle \\ |\tilde{1}_R\rangle \end{pmatrix} = \begin{pmatrix} \cos\theta/2 & \sin\theta/2 & 0 \\ -\sin\theta/2 & \cos\theta/2 & 0 \\ 0 & 0 & 1 \end{pmatrix} \begin{pmatrix} |3_R\rangle \\ |2_R\rangle \\ |1_R\rangle \end{pmatrix} = U \begin{pmatrix} |3_R\rangle \\ |2_R\rangle \\ |1_R\rangle \end{pmatrix}, \tag{4.7}$$

which makes $\tilde{H}_0 = U^{\dagger} H_0' U$ diagonal when $\tan\theta = \Omega/\Delta$. The resulting energies, $\tilde{e}_1 = e_1 = 0$ and $\tilde{e}_{2,3} = \left(e_3 - \omega + e_2 \mp \sqrt{\Delta^2 + \Omega^2}\right)/2$ are depicted in Fig. 4.2(c). To derive a master equation for the working medium we follow the steps explained in section 2.2. We neglect the principal value terms but do not make the secular approximation. The principal value terms emerge from tracing out the bath degrees of freedom and correspond to energy shifts, which can be included in the original Hamiltonian. Further justification for these approximations is given in Ref. [39] and chapter 2. The resulting equations-of-motion are given in Eqs. (4.16–4.18) and Eqs. (A.1–A.6).

The method of counting field statistics was implemented to obtain the energy currents to the bath (also described in chapter 2). We find

$$\langle \dot{Q}_{\rm c} \rangle = \tilde{e}_3 R_3^c + \tilde{e}_2 R_2^c, \tag{4.8}$$

$$\langle \dot{E}_{\rm h} \rangle = (\tilde{e}_3 + \omega) R_3^h + (\tilde{e}_2 + \omega) R_2^h. \tag{4.9}$$

The energy current to the cold bath is entirely heat and hence denoted Q_c, whereas that to the hot bath comprises both heat and work, with the latter arising from the flow of particles from the exciton reservoir, which in general has a non-zero chemical potential. The rates that appear in the energy currents are

$$\begin{aligned} R_{2,3}^c = \pi J_c(\tilde{e}_{2,3}) [&\mp (n_c(\tilde{e}_{2,3}) + 1) \sin\theta \, \mathfrak{Re}[\rho_{23}] \\ &+ (1 \pm \cos\theta)((n_c(\tilde{e}_{2,3}) + 1)\rho_{22} - n_c(\tilde{e}_{2,3})\rho_{11})] \end{aligned} \tag{4.10}$$

$$\begin{aligned} R_{2,3}^h = \pi J_h(\tilde{e}_{2,3} + \omega) [&\mp (n_h(\tilde{e}_{2,3} + \omega) + 1) \sin\theta \, \mathfrak{Re}[\rho_{23}] \\ &+ (1 \mp \cos\theta)((n_h(\tilde{e}_{2,3} + \omega) + 1)\rho_{33} - n_h(\tilde{e}_{2,3} + \omega)\rho_{11})]. \end{aligned} \tag{4.11}$$

Here ρ_{ij} are the elements of the density matrix in the basis $(|1_R\rangle, |2_R\rangle, |3_R\rangle)$. These rates can also be expressed in terms of the elements of the density matrix in the diagonal basis, $(|\tilde{1}_R\rangle, |\tilde{2}_R\rangle, |\tilde{3}_R\rangle)$. Denoting those elements by $\tilde{\rho}_{ij}$ the rates are

$$R^c_{2,3} = \pi J_c(\tilde{e}_{2,3})\{(1 \pm \cos\theta)[(n_c(\tilde{e}_{2,3})+1)\tilde{\rho}_{22,33} - n_c(\tilde{e}_{2,3})\tilde{\rho}_{11}] + (n_c(\tilde{e}_{2,3})+1)\sin\theta\mathfrak{Re}[\tilde{\rho}_{23}]\} \tag{4.12}$$

$$R^h_{2,3} = \pi J_h(\tilde{e}_{2,3}+\omega)\{(1 \mp \cos\theta)[(n_h(\tilde{e}_{2,3}+\omega)+1)\tilde{\rho}_{22,33} - n_h(\tilde{e}_{2,3}+\omega)\tilde{\rho}_{11}] - (n_h(\tilde{e}_{2,3}+\omega)+1)\sin\theta\mathfrak{Re}[\tilde{\rho}_{23}]\}. \tag{4.13}$$

$J_{\mathrm{c,h}}$ are the spectral densities for the cold and hot baths, respectively. In the following we take a Lorentzian for the cold phonon bath,

$$J_{\mathrm{c}}(x) = (\alpha^{\mathrm{c}}/2)\left[(x-e_2)^2 + g_{\mathrm{ph}}^2\right]^{-1}, \tag{4.14}$$

and a step function for the hot pump bath

$$J_{\mathrm{h}}(x) = \alpha^{\mathrm{h}}\Theta(x - E_0). \tag{4.15}$$

We have also tested a Gaussian spectral density for the cold bath, and found no relevant differences. The parameters $\alpha^{\mathrm{c,h}}$ control the maximum values of the spectral density, and g_{ph} the width of the Lorentzian distribution, whose value needs to be large enough to allow the Born-Markov approximation. E_0 is the energy of the lowest exciton state in the pump reservoir. The bath occupation function for the cold bath is $n_{\mathrm{c}}(E) = (e^{\beta_{\mathrm{c}}E}-1)^{-1}$, and that for the hot bath is the corresponding grand-canonical form, including the chemical potential, $n_{\mathrm{h}}(E) = (e^{\beta_{\mathrm{h}}(E-\mu)}-1)^{-1}$.

4.3 Results

We begin by analyzing the dynamics of the cycle in terms of the occupations of the states $|n_R\rangle$ $(n = 1, 2, 3)$. The diagonal elements of the density matrix, in the rotating basis, obey

$$(\dot{\rho})_{11} = (R_2^c + R_3^c) + \left(R_2^h + R_3^h\right) \equiv R^c - R^h \tag{4.16}$$

$$(\dot{\rho})_{22} = -\left(R_2^c + R_3^c\right) + R = -R^c + R \tag{4.17}$$

$$(\dot{\rho})_{33} = -\left(R_2^h + R_3^h\right) - R = R^h - R. \tag{4.18}$$

Here

$$R = \langle \dot{W} \rangle / \omega = \Omega \; \mathfrak{Im} \rho_{32}, \tag{4.19}$$

and $R_{2,3}^{c,h}$ are given by Eqs. (4.10) and (4.11) or (4.12) and (4.13). From these expressions we identify $R^c = (R_2^c + R_3^c)$ as the rate of population transfer from $|2_R\rangle$ to $|1_R\rangle$, due to the cold bath, $R^h = -(R_2^h + R_3^h)$ at that from $|1_R\rangle$ to $|3_R\rangle$, due to the hot bath, and R as that from $|3_R\rangle$ to $|2_R\rangle$, due to the interaction with the condensate. The steady-state condition,

$$R = R^c = R^h, \tag{4.20}$$

is that the rates around each part of the cycle are equal.

The energy fluxes to the baths, Eqs. (4.8, 4.9), can be interpreted [18] in terms of the eigenstates of H_0', $|\tilde{n}_R\rangle$, which differ from the states $|n_R\rangle$ around which the population circulates. Due to the oscillating driving field the states are Floquet states associated with a periodic quasi-energy. The transformation to the rotating basis introduces replicas of the original energy levels, which are then mixed by the driving field to form dressed-states with shifted energies. This process is illustrated in Fig. 4.2, which shows the original energy levels (with the field turned off) in the left panel (a), their replicas under periodic driving, (b), and the dressed states obtained by diagonalizing H_0', (c).

The heat current to the cold bath, Eq. (4.8) is the sum of two contributions, each the product of the quasi-energy of a dressed state $\tilde{e}_2, \tilde{e}_3$, and one of the two rates, $R_{2,3}^c$. Thus, we can interpret this heat flow as arising from two transitions in the Floquet spectrum, as illustrated in Fig. 4.2(c). The hot bath acts similarly, but induces transitions from the ground state to levels in the second quasi-energy band. The cycle is closed by the power output, Eq. (4.4), that consists of quanta of energy ω emitted at the rate R. This is illustrated in Fig. 4.2 as two independent transitions, each between equivalent dressed states, suggesting the formation of two independent cycles [18]. However, it should be noted that this interpretation implies a secular approximation and only holds in a strong-driving limit. The energy currents cannot in general be interpreted as coming from two separate cycles, as $R^c_{2,3} \neq -R^h_{2,3}$. In fact, the rates in Eqs. (4.12, 4.13) contain contributions of the form of Boltzmann transition rates, and interference terms weighted by the mixing angle θ. The latter are responsible for coupling the two fictitious cycles, that is, because of the sign difference they constitute transitions to the ground state in inverted directions, which is effectively an inter-cycle transition.

The first law of thermodynamics is $\langle \dot{W} \rangle + \langle \dot{Q}_c \rangle + \langle \dot{E}_h \rangle = 0$. Using the forms for $\langle \dot{W} \rangle, \langle \dot{Q}_c \rangle$, and $\langle \dot{E}_h \rangle$, and the steady-state condition, Eq. (4.20), it becomes

$$\tilde{e}_2(R^c_2 + R^h_2) + \tilde{e}_3(R^c_3 + R^h_3) = 0. \tag{4.21}$$

This condition is not exactly satisfied, but holds to a good approximation in the parameter regimes used here, where the Born-Markov approximation is appropriate.

4.3.1 Steady state of the microcavity

We can describe a complete system, including the condensate, by noting that the growth of the condensate comes from the output of a large number M of identical three-level heat engines. M represents the number of states in the bottleneck region that generate scattering to the ground state of the polariton distribution, and is on the order of $M = 10^4$ in typical cases. The growth rate of a condensate, of population N, is then $MR(N)$, where the dependence of the cycle rate R on Ω and therefore N has been made explicit. This growth competes against the losses due to radiative polariton decay, with rate γ. The steady-state condition for the condensate number, N_c, is then that

$$MR(N_c) = N_c\gamma. \tag{4.22}$$

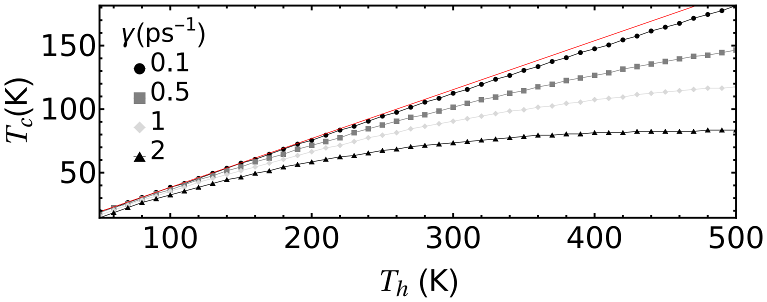

Figure 4.3: Phase diagram of polariton condensation as a function of the temperatures of the hot and cold reservoir for different microcavity decay rates. The points below each line correspond to the condensate region. The red line corresponds to the case of infinite microcavity lifetime, where condensation occurs at the onset of inversion. The parameter region of the condensed phase is smaller for larger radiative decay, as it implies more inversion is required to produce condensation.

In the following, we choose parameter values typical of GaAs microcavities. The prefactor of the phonon spectral density is chosen in line with the exciton relaxation times obtained numerically and experimentally [8] $\alpha^{\mathrm{c}} = 0.1$ ps^{-1}. We take the linewidth of the phonons to be $g_{\mathrm{ph}} = 1.7$ ps^{-1}. The temperature of the cold bath is the lattice temperature of the semiconductor, which we take to be 10 K. The spectral density, as well as the chemical potential, and temperature of the hot bath, depend non-trivially on the incoherent pump. We choose $\alpha^{\mathrm{h}} = 0.2$ ps^{-1}, $E_0 = 1$ eV, $E_0 - \mu = 8$ meV and $T_{\mathrm{h}} = 200$ K initially, and investigate the effects of varying these parameters. We assume a polariton lifetime of $1/\gamma = 1$ ps. For the polariton-polariton scattering strength we use the expression derived in [36] to estimate $g_c \approx 0.048$ ps^{-1}. The detuning appears in our model with fixed condensate and transition energies, and will determine the condensate in-scattering rate, i.e., the gain from the working medium. In practice, however, the condensate, pump, and idler states lie in a continuum, and a range of detunings are present. We expect condensation to occur in the most favorable mode, and so focus on the resonant case $\Delta = 0$.

Eq. (4.22) and the equations-of-motion can be solved numerically to determine the condensate occupation N_c in the steady-state. This solution can be used to map the phase diagram, i.e., the region of parameter space in which $N_c \neq 0$. Fig. 4.3 shows a numerically computed phase diagram for condensation, in terms of the temperatures of the hot (pump) and cold (lattice) heat baths, for several values of the decay rate γ. The condensed state, with $N_c \neq 0$, lies below each curve, with the normal state, $N_c = 0$, above it. For these parameters the transition is continuous. It can be seen that the phase boundaries approach the red diagonal line as $\gamma \to 0$. This corresponds to the ideal thermodynamically-reversible limit [14], in which condensation occurs when inversion is reached, $\rho_{33}/\rho_{22} = 1$. As noted by Scovil and Schulz-DuBois [14], the requirement of inversion implies laser action is bounded by the Carnot efficiency, and reaches it in the reversible limit where inversion first appears. Generalizing their argument to include the chemical potential of the hot reservoir, the condition for inversion

$$\frac{\rho_{33}}{\rho_{22}} = \frac{\rho_{33}}{\rho_{11}}\frac{\rho_{11}}{\rho_{22}} = e^{-\beta_h(e_3-\mu)}e^{\beta_c e_2} > 1, \tag{4.23}$$

implies that the efficiency

$$\eta = (W_{out} - W_{in})/Q_{in} = (\omega - \mu)/(e_3 - \mu), \tag{4.24}$$

is less than the Carnot efficiency $\eta_C = 1 - T_c/T_h$. Here we have used $e_3 - e_2 = \omega$ ($\Delta = 0$) and identified ω as the work output per cycle, μ as the work input, and $e_3 - \mu$ as the heat input (with $e_1 = 0$).

The continuous transition can be understood using a perturbative expansion of the steady-state in Ω. In the normal state we have $\Omega = 0$ so $\theta \to 0$, $\tilde{e}_2 = e_2, \tilde{e}_3 = e_3 - \omega$. The equations-of-motion reduce to the standard Lamb equations for a three-level laser [18], given in the Appendix. The steady-state has the populations ρ_{33}/ρ_{11} and ρ_{22}/ρ_{11} in equilibrium with the hot and cold baths, respectively, and vanishing coherences. Expanding around this solution gives the steady-state coherence to first order in Ω, and hence, using Eq. (4.19), the scattering rate

$$R = \frac{\Omega^2\left(\rho_{33} - \rho_{22}\right)}{\gamma_\downarrow^c + \gamma_\downarrow^h} = \frac{4g_c^2 N\left(\rho_{33} - \rho_{22}\right)}{\gamma_\downarrow^c + \gamma_\downarrow^h}. \tag{4.25}$$

Here $\gamma_\downarrow^c$ ($\gamma_\downarrow^h$) are the emission rates into the cold (hot) bath, respectively. Eq. (4.25) is the Fermi golden rule expression for scattering into a final state, with a linewidth generated by the emission into the baths. It defines, via Eq. (4.22), the critical inversion at which gain exceeds loss, and hence the phase boundary. The energies involved in the cycle are unaffected by the condensate to this order,

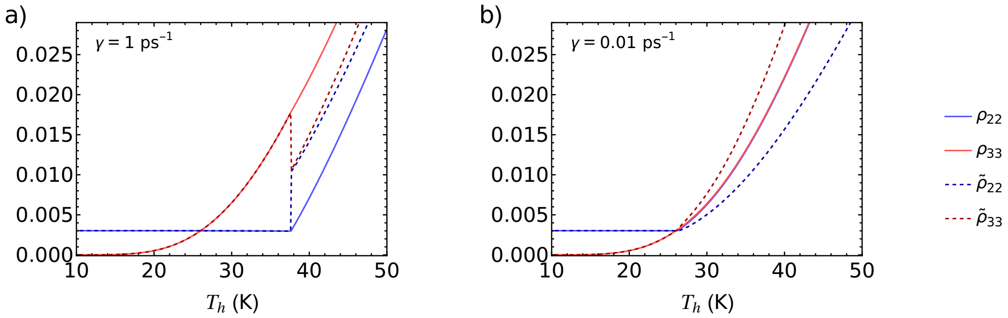

Figure 4.4: Diagonal elements of the density matrix in the bare basis $\rho_{22/33}$ and the eigenbasis $\tilde{\rho}_{22/33}$ for two different values of cavity decay. The elements in the different basis coincide at the normal state, and at the phase boundary to the condensed state, they become mixed and $\tilde{\rho}_{33} = \tilde{\rho}_{33}$. For a microcavity with larger decay rate the phase transition requires some population inversion (a), while for small decay rate the phase transition is near the inversion point (b).

so the efficiency, Eq. (4.24), is constant.

The red line in Fig. 4.3 separates the diagram into two regions: above it, the efficiency set by the energies is greater than the Carnot efficiency, and condensation can never occur. It emerges immediately below this line for $\gamma \to 0$, where condensation is supported by an infinitesimal power flow from the working medium. In this limit the threshold for condensation corresponds to the condition that the entropy changes of the hot and cold reservoirs balance,

$$\frac{e_2}{T_c} = \frac{e_3 - \mu}{T_h}. \tag{4.26}$$

For non-zero γ, condensation requires finite, and therefore irreversible, power flows from the working medium, which will produce a lower-than-Carnot efficiency for given bath temperatures. The phase boundary therefore departs from the reversible line; the non-zero γ implies that the temperature difference $T_h - T_c$ required to drive condensation is increased, as it must overcome the loss.

Another way of looking at the nonequilibrium effects of γ in the threshold is by looking at the inversion required for condensation. Figure 4.4 shows the second and third diagonal terms of the density matrices ρ and $\tilde{\rho}$. Before threshold, because $N_c = 0$, the elements of the two matrices coincide. At the threshold, the condensate field emerges, resulting in a mixture of the two excited states, and $\tilde{\rho}_{22}$ and $\tilde{\rho}_{33}$ acquire the same value. Comparing Figs. 4.4(a) and (b), a larger γ

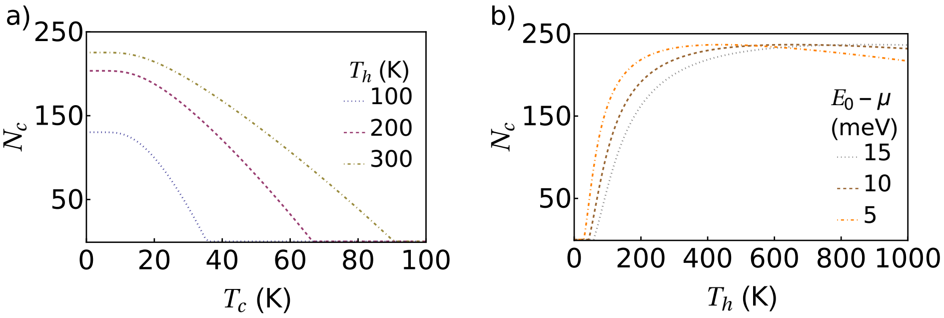

Figure 4.5: Size of the condensate as a function of the temperature of the cold (a) and hot (b) baths for various temperatures of the hot bath, and chemical potentials, respectively. A second order phase transition is observed from the normal state with $N_c = 0$ to a condensed state with non-vanishing occupation.

requires a larger inversion to overcome the loss, and hence a higher temperature for the hot bath. In the condensed phase, the population of the excited states of ρ increases with T_h, but the inversion $\rho_{33} - \rho_{22}$ is constant.

To determine the steady-state occupation in the condensed state we solve Eq. (4.22) using the steady-state calculated numerically. This incorporates the dependence of the dressed-state energies and wavefunctions on the condensate occupation, which provides the nonlinearities, beyond Eq. (4.25), that are needed to stabilize the condensate at a finite density. Results are shown in Fig. 4.5, as functions of the two bath temperatures.

Considering first the dependence on T_h, we see that the condensate size increases rapidly with T_h once the threshold is crossed, and then saturates or decreases. This is expected from the occupation of the hot bath at the energy of the upper level ($\approx e_3$). If we consider the equilibrium of the upper level and the hot bath only, its population will be $(1 + e^{-\beta_h(e_3-\mu)})^{-1}$, which is negligible until $kT_h \sim (e_3 - \mu)$, at which point it rapidly grows before saturating at 0.5. The small decrease could be explained by noting that $\gamma_h^{\downarrow}$, approximately proportional to $(1 + n_h(e_3))$, increases with temperature due to the stimulated emission into the hot reservoir. This will broaden the line and hence, as expected from Eq. (4.25), reduce the gain. Such a mechanism has been shown to produce an upper critical threshold, i.e., a maximum T_h, in the three-level laser model [91].

The dependence of the condensate size on T_c can be understood analogously in terms of the thermal occupation of the cold bath, i.e., the phonons. Below the

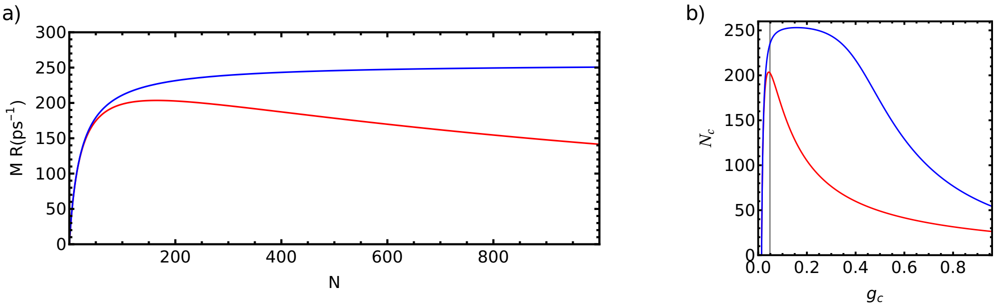

Figure 4.6: (a) Total in-scattering rate into the condensate as a function of its size, and (b) Equilibrium size of the condensate as a function of the light-matter coupling strength. We use red when considering a Lorentzian and blue when considering a constant phonon spectral density. The rate reaches a maximum value for both spectral densities, however, the Lorentzian shape of the spectral density causes a reduction in R for large condensates.

critical temperature the condensate occupation increases smoothly, and plateaus at very low temperatures. The critical T_c arises here from the requirements that the lower state of the $3-2$ transition should be depopulated sufficiently to generate inversion – in other words, the phonons must cool the high-momentum excitons, here represented by the pump and the idler states, to a low temperature so that the idler population is small. The saturation at low temperatures arises from the assumption of a single energy gap for the phonon relaxation, which implies that the equilibrium idler population is effectively zero for temperatures $kT_c \ll e_2$.

4.3.2 Effects of the internal structure of the reservoirs

Fig. 4.6(a) shows the total scattering rate into the condensate, $MR(N)$, in the steady-state, as function of the condensate size N. This shows the existence of a maximum power output of the three-level system. Such maxima are general features of the three-level heat engine [18], caused by the energy-dependence of the scattering rates, which are sampled at the dressed-state energies $\tilde{e}_{2,3}$ with splitting $\sim \Omega$ when $\Omega \gg \Delta$. In Ref. [18] the existence of a maximum power was attributed to the frequency-dependence of the hot bath occupation function. Although this thermal factor will produce such an effect in general, it cannot explain the particular peak in Fig. 4.6, since here kT_h is much larger than the energy shifts at the maximum power point. It arises, instead, from the spectral func-

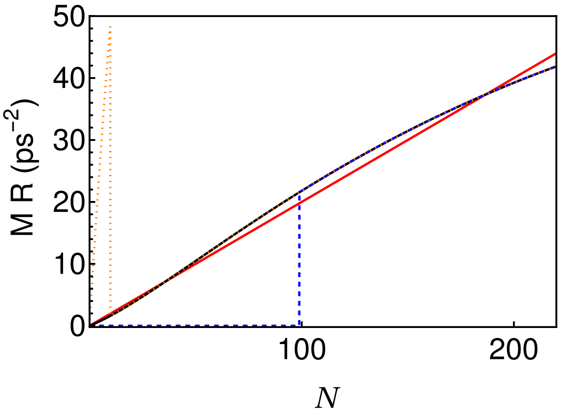

Figure 4.7: In-scattering rates with $\Delta = 0.3$ meV and $E_0 - e_3$=0 (black solid), 0.33 meV (blue dotted), -0.2 meV (orange dotted). The red curve is the loss rate. These parameters lead to in-scattering rates with a convex region (black solid and orange dotted) and discontinuities (blue dotted and orange dotted). Such forms give rise to first-order transitions and bistability (see text).

tion of the cold (phonon) environment, which we have modelled as a Lorentzian of width g_{ph}. When $N = 0$ the dressed-state energies lie at the peak of this Lorentzian, but they move away as $\Omega \sim \sqrt{N}$ increases, reducing the emission rate of phonons into the environment and slowing the cycle. This interpretation is consistent with the result for a flat phonon spectral density, shown for comparison. Although the assumption of a Lorentzian spectral density for the phonons is not necessarily realistic, the heat baths relevant for polariton condensates do have spectral structure. This can be expected to lead to a maximum power once the condensate nonlinearities become comparable to either the scale of the structure or the temperatures.

Fig. 4.6(b) shows the size of the condensate as function of the light-matter coupling strength. As a consequence of the energy shifts caused by the coupling with the field, the size of the condensate has a sharper peak if the phonon spectral density is a Lorentzian (red) than if it is constant (blue). In the first case, the energy shifts affect both the spectral density and the Bose function Eq. (4.10), while in the second case only the Bose function is affected.

In some cases there are additional phenomena which can arise from the non-trivial spectral densities of the baths. Fig. 4.7 shows the gain as a function of condensate size for three different sets of parameters, revealing two unexpected effects. The first is the presence of discontinuities in the steady-state, either connecting a region of zero gain to non-zero gain, or causing a sudden drop in the gain. These arise from the interplay between the energy shifts of the driving and the spectral density of the hot bath, which we have assumed to have a step-function onset at energy E_0. The dashed-blue curve arises in a situation where the upper level of the heat engine lies just below the hot bath, $e_3 < E_0$, so that there is no population of the upper level in the absence of the condensate, and hence no gain. However, as the condensate size increases the upper dressed state, $\tilde{e}_3$, moves to higher energies, and crosses E_0, at which point gain appears. A related situation, shown by the orange dotted curve, appears if e_3 starts just above E_0. In that case, while the two dressed states start in the band, as the condensate occupation increases the lower-energy one drops below E_0, and the gain suddenly decreases. The second, more subtle, effect is also visible in this curve, as well as the black curve, which corresponds to the case where e_3 starts exactly at E_0. This is the presence of a convex part of the gain curve at small N. We suggest this is because there is also a small positive detuning here, so that the upper dressed state is composed mostly of $|3\rangle$ in the limit $N \to 0$. However, as the splitting Ω reaches the detuning Δ, this component of the upper dressed state – which is the only one pumped by the hot bath at this point in the curve – begins to reduce significantly, suppressing the gain. We note this convex form of $R(N)$ implies the transition is first-order, with the crossing point solving $MR(N) = \gamma N$ first appearing at a non-zero N. A first-order behavior can also be expected from the physics of the step-like curve which, for the more realistic case of a smoothly-increasing spectral density, will become a smooth but convex $R(N)$. In addition, we expect these forms to lead to bistability of the condensed states, since they have two intersections with the loss curve.

The physics of these effects lead us to suggest they could be achieved experimentally by constructing a system in which the source of the pairwise scattering, i.e. the bottleneck state, lies in a region where either the population or spectral density of the exciton reservoir increases with increasing energy. A natural way to do this would be to use resonant pumping at an energy above the pairwise resonance. We note that, although we have assumed a thermal population, the expressions for the rates, Eqs. (4.10) and (4.11) or (4.12) and (4.13), can be used

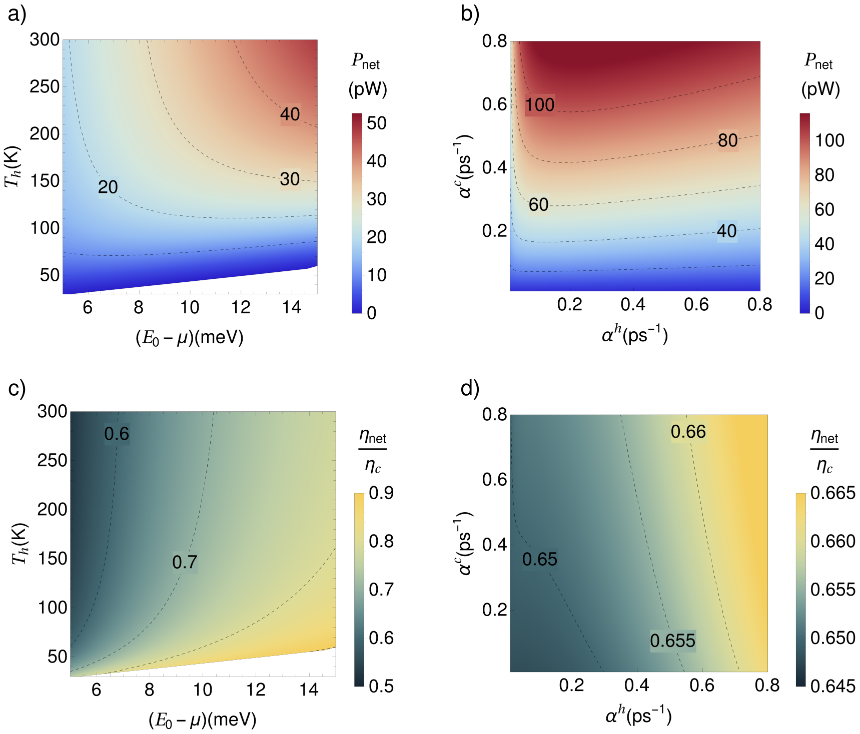

Figure 4.8: Net output power (top row) and efficiency (bottom row) of a steady-state condensate, as functions of the temperature and chemical potential of the hot bath (left column), and of the coupling strengths to the two baths (right column). The chemical potential is measured relative to the lowest state of the pump reservoir, E_0, and the efficiencies are normalized by the Carnot efficiency. The net output power grows if T_h or $(E_0 - \mu)$ increase and has stronger dependence on the coupling strength with the cold than with the hot bath. The efficiency shows only a weak dependence on the parameters considered.

also in the non-thermal case.

4.3.3 Thermodynamic figures of merit

Figure 4.8 shows some results for the steady-state power output and efficiency of the condensate. The white regions denote the non-condensed phase, and the colors depict the net power $P_{\text{out}} - P_{\text{in}}$, and net efficiency $-(P_{\text{out}} - P_{\text{in}})/Q_{\text{h}}$, in the steady-state. The two plots in the left column show the effects of varying the hot bath temperature and chemical potential, while the right column shows the corresponding effects of varying the coupling strengths. The net power increases with increasing hot bath temperature, in line with the condensate occupation shown in Fig. 4.5. However, while the condensate occupation increases with increasing chemical potential, the net power output decreases. This is because although increasing μ increases the cycle rate and hence the gross power, $\omega R = \omega\gamma N/M$, it also increases the work input, giving an overall decrease in the net power, $(\omega - \mu)R$. Considered as functions of the coupling strengths, the net power output increases significantly with an increasing coupling to the cold bath. However, the power output depends only weakly on the hot bath coupling parameter, and can even decrease as it increases. We suggest that the weak dependence arises because, for the temperatures chosen, the cycle rate is limited by emission into the cold bath rather than absorption from the hot one. This emphasizes the need for rapid phonon thermalization in the high-momentum excitons, in order to drive condensation (see Fig. 4.1).

The efficiency, as a function of temperature and coupling constants, is shown in the lower two panels of Fig. 4.8. It is shown relative to the Carnot efficiency, which explains most of the apparent dependence on the temperatures; the energy shifts are small for these parameters, so that η is well approximated by Eq. (4.24). The efficiency at the threshold is below the Carnot efficiency due to the finite loss rate. Since the efficiency is determined almost entirely by the energy levels, there is only a very small effect of the coupling strengths.

4.3.4 Modes of operation of the thermal machine

So far, we have considered condensation in the regime $\omega > \mu$. Here the work output per cycle, ω, exceeds the work input, μ, so that condensation is only possible with the conversion of heat to work. The condensate in this case operates as a heat engine, and requires a higher temperature for the exciton reservoir than for the phonons. However, if $\omega < \mu$ the work output per cycle, ω, is less than the work input per cycle, μ, so the machine operates not as a heat engine, but as a dissipator or refrigerator. In these modes heat is not converted to work, as in a heat engine, but rather the excess work, $\mu - \omega$, is dissipated as heat. To avoid confusion we here use T_x and T_{ph} to refer to the temperatures of the exciton and phonon reservoir, instead of the subscripts denoting hot and cold.

To understand condensation at the different possible modes of the thermal machine we calculate the phase diagram by changing the chemical potential around

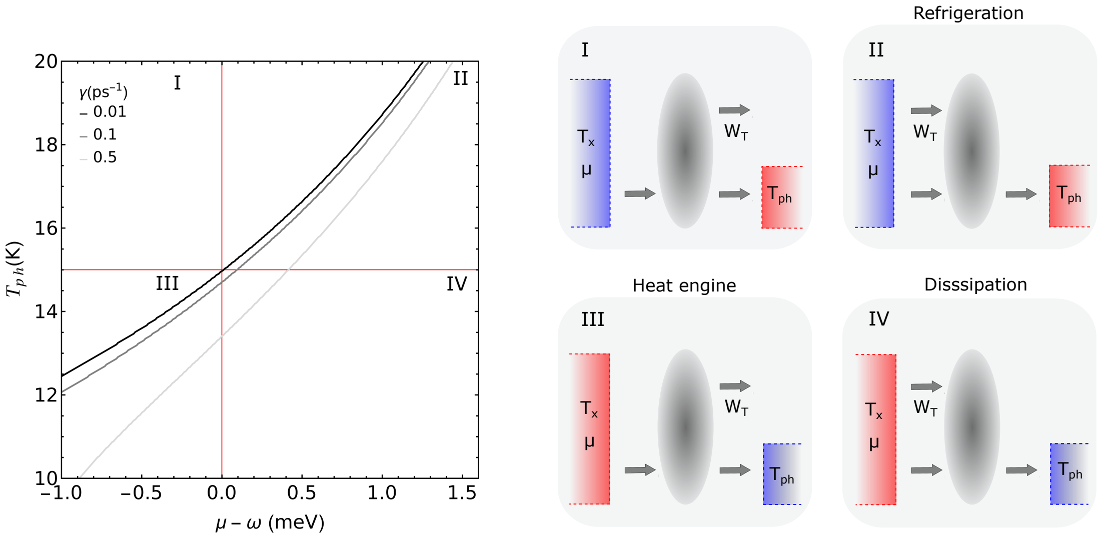

Figure 4.9: Phase diagram of polariton condensation as a function of the phonon temperature and the chemical potential. The horizontal red line corresponds to the temperature of the pump bath $T_x = 15$K, and together with the vertical line at $\mu = \omega$ divide the diagram into four quadrants. The first **I** is not allowed by the second law of thermodynamics, and the other three correspond the possible modes in which a thermal machine can operate: **II**. the refrigeration mode, **III**. the heat engine mode, and **IV**. the dissipation mode. The condensate phase corresponds to the region below the black and grey lines. With a negligible loss rate, the phase boundary corresponds to a reversible limit, therefore increasing the chemical potential, which goes from heat engine mode to refrigeration mode without crossing the dissipative parameter region.

$\mu = \omega$, and taking $T_x = 15$K. In Fig. 4.9 the red lines divide the parameter region in four, which can be classified according to the direction of flow of the net power and heat current. For the regions (I) and (II) $T_x < T_{ph}$, meaning that energy is flowing from a colder to a hotter reservoir. This can happen as long as the net power is being input into the system, and the machine is in the refrigeration mode (II). The situation corresponding to quadrant (I) violates the second law of thermodynamics, so condensation can never happen in that parameter region. The regions (III) and (IV) are such that $T_x < T_{ph}$, and heat flows from hot to cold, therefore are both allowed. (III) corresponds to the heat engine mode and (IV) to the case in which work is excess dissipated.

The grey lines in Fig. 4.9 correspond to the phase diagrams for different values of decay rates, where below each line is the condensed phase, $N_c \neq 0$, and above is the normal phase, $N_c = 0$. The phase boundary of a perfect microcavity (i.e., $\gamma \to 0$) is a reversible limit and, therefore, does not cross the dissipative region (IV).

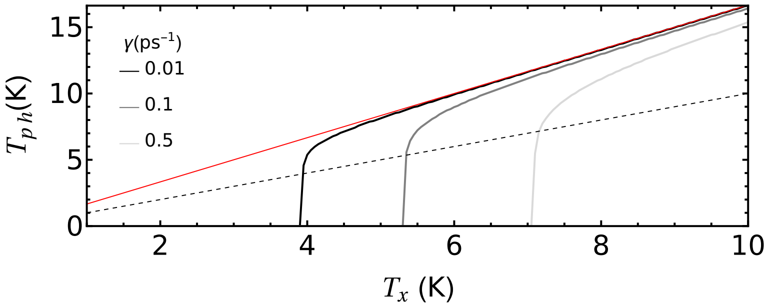

Figure 4.10: Phase diagram of condensation for $\omega < \mu = 1.002$ eV, as a function of the temperatures of the exciton T_x and phonon T_{ph} reservoir, for three different values of decay rates. The area below each curve corresponds to the parameter region where condensation can occur. The red line corresponds to the reversible limit of the thermal machine, and indicates the phase boundary when $\gamma \to 0$.

Fig. 4.10 shows the phase diagram of condensation varying T_h when $\omega - \mu = 2$ meV. The condensate occurs in the region below and to the right of the curves, and it can be seen that at the onset of condensation $T_{ph} > T_x$. The excess work here is deposited as heat in the higher-temperature reservoir, corresponding to a flow of heat against the temperature gradient. The dashed line corresponds to $T_x = T_{ph}$, so that in the region below this the excess work is dissipated in the lower-temperature reservoir.

4.4 Conclusions

In summary, we have argued that a driven-dissipative condensate is a form of heat engine, and as such requires consideration of both a hot and cold bath. We considered in depth the case of a microcavity polariton condensate, and constructed a minimal heat-engine model that captures the key processes involved in condensation. Our results show how condensation is determined by the temperatures of both the hot (exciton) and cold (phonon) bath, and that the temperature difference between these must exceed that required in the reversible limit in order to overcome the polariton loss. They also emphasize the importance of rapid cooling in the high-momentum exciton states, in order to maintain effective scattering into the condensate. The maximum power output of the condensate shows effects of the spectral densities of the environment, and the formation of dressed states, which can also produce unusual phenomena including a first-order phase boundary and bistability.

Our results provide guidance for extending the regimes and systems which support condensation, and our methods could be extended to consider other examples such as the condensation [4] and thermalization [92] of photons. Furthermore, it would also be interesting to explore the reversed operation of the heat-engine and the possibilities for phonon refrigeration [93].

One extension of our work would be to include a distribution of energies for the states in the working medium, i.e. inhomogeneous broadening. In this case the gain, given by Eq. (4.25) and appearing in the threshold Eq. (4.22), would be replaced its average over the broadened line. While this would modify the details of the phase boundary, and make condensation more difficult due to the dispersion of the gain over different frequencies, we would not expect it to have dramatic effects unless the broadening becomes comparable to the scale of the dispersion relation. Small broadenings could, however, modify some of the details of the results in the nonlinear regime, where they would be relevant in comparison to the energy shifts Ω or features in the bath spectral densities. We have found such effects in preliminary work; for example, the peak in Fig. 4.6 is replaced, over the range shown, by a plateau, if the levels e_2 and e_3 are broadened by 2 meV while keeping $e_3 - e_2$ fixed.

Chapter 5

Photon Condensation

IN WHICH WE DERIVE NONEQUILIBRIUM THERMODYNAMIC CONDITIONS ON THE CONDENSATION OF A PHOTON GAS

In the previous chapters, we examined condensation of polaritons, which are particles resulting from the strong interaction between light and matter. In this chapter, we continue the analysis of the thermodynamics of nonequilibrium condensates by focusing on a gas of photons in a microcavity. Photon condensation occurs in microcavities where light is only weakly coupled to matter, so the emission detected from the cavity is that of a bare gas of photons and the interaction with matter serves primarily to cool the photon gas. Like conventional lasers, photon condensates produce coherent light emission and therefore are important for developing all-optical devices, such as transistors and highly efficient light sources.

Both photon and polariton gases are nonequilibrium systems that require a constant external source to maintain a steady state against the losses. The particles interact with a cold environment to thermalise and, if the thermalisation time is small compared with the particle lifetime, it gives rise to a Bose distribution in the steady state. Although a thermal distribution is not necessarily reached, continuous thermalisation with a colder reservoir is essential to increase the occupation of lower energy states.

The mechanisms behind the interaction and thermalisation of photons and polaritons are fundamentally different. The hybrid nature of polaritons provides them with a low mass inherited from their photonic part combined with a cross section derived from their excitonic component. In this way, polariton interactions occur mainly due to exciton scattering, while, in a photon gas, interactions must be consistent solely with the characteristics of light. Photons have vanishing chemical potential and so generally interact without conserving the total number of particles. This means that when a gas of photons is cooled, it loses energy by particles escaping instead of reducing its temperature, which sets a challenge for achieving thermalisation.

Nonetheless, thermalisation can occur in microcavities where photons interact weakly with a material by absorption and re-emission. In this way, the total number of excitations (which includes the photons and the excited molecules in the material) is conserved and thermal equilibrium can be reached while controlling the effective number of photons in the quantum gas. Thermalisation has been observed in both a dye-filled microcavity [94], and GaAs semiconductor microcavity [3]. Inside the microcavity, the longitudinal mode of light is frozen, and the transversal modes constitute a two-dimensional gas with energy and mass determined by the length of the cavity. The medium absorbs and remits the photons, acting like a reservoir with which the photons thermalise. In the case of a dye-filled microcavity, features such as heat capacity and fluctuations have also been explored [95, 96].

In the following, we investigate photon condensation in a dye-filled microcavity. Because of the large cavity lifetime with respect to the thermalisation time, photons can reach an equilibrium Bose-Einstein distribution in a steady state. However, in this chapter, we argue that, despite the presence of an equilibrium steady state, one cannot entirely ignore the nonequilibrium nature of the process. As in the previous chapter, we point out that condensation occurs in a steady state in which particles and energy are supplied from a pump and lost as they escape from the condensate, so the system operates as a thermal machine, constrained by the requirement of positive entropy production. This sets the threshold and, as we shall see, subsumes the usual criteria for equilibrium condensation.

A theoretical model using rate equations for the populations of photons and the degree of excitation of the dye molecules has shown that, for realistic parameters, the steady state distribution of photons is thermal as long as the photon modes are near resonance with the dye (up to -200THz of detuning) [5, 97]. We use this model as a starting point and show how it leads to an interpretation of the condensing photon gas as a thermal machine. Next, we extend this model to consider thermal pump sources. We study a toy model of a photon gas with two energy levels and explore the effects of pumping the microcavity at different energies. These results suggest that the pump can be manipulated to produce condensation from different sources. In particular, we investigate sunlight as a source, and show that condensation can be achieved from sunlight harvesting. While the required temperature is large $T > 1500$K, the coupling with the thermal source can be arbitrarily small. The efficiency with such pump is lower than the one in which the pump affects the population of the dye energy levels directly.

Our analysis requires only that the Kennard-Stepanov relation is obeyed by the radiative rates of the material that mediates the photon thermalisation. Therefore, it can be extended to other systems such as semiconductors, in which photon condensation has also been demonstrated [3, 98].

5.1 A model of photon condensation

In this section, we review the model of photon condensation proposed by Kirton and Keeling [5]. The model is inspired by an experiment conducted at room temperature, with a microcavity made of two curved mirrors and filled with a dye solution (typically rhodamine 6G) [94]. Because of the confinement, the photon modes acquire a cutoff energy ω_0 and behave as a two-dimensional gas. The relevant energy scales and processes considered in the model are displayed in a schematic cartoon of the system in Fig. 5.1(a). The transverse photon modes are equally spaced with energies $\omega_m = \omega_0 + m\epsilon$ and degeneracy $g_m = m + 1$. The dye molecules are treated as two-level systems with energy splitting ω_d and are coupled to a bosonic state corresponding to a rovibrational mode. The vibration

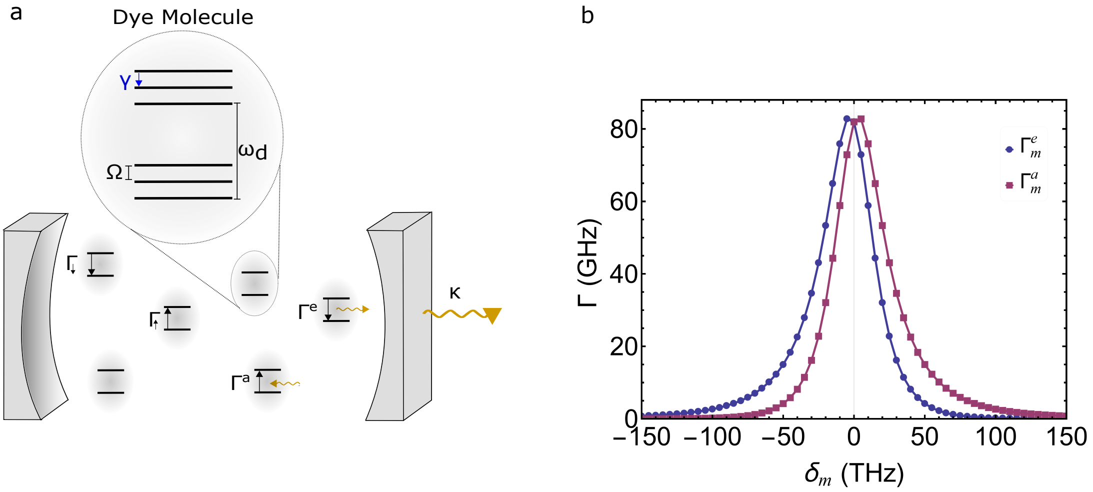

Figure 5.1: (a) Illustration of the dye-filled microcavity. The dye molecules are treated as two-level systems with dressed states controlled by vibration modes. The energy splitting between the states in each manifold is Ω, and γ is the relaxation rate. The dye is affected by the incoherent pump $\Gamma_{\uparrow/\downarrow}$ and radiative emission and absorption rates $\Gamma_m^{e/a}$. The lifetime of the cavity is $1/\kappa$. (b) Rates of emission and absorption of the dye for different photon modes. The photon energy is scaled in relation to the molecular gap $\delta_m = \omega_m - \omega_d$.

states are modelled as modes of a harmonic oscillator with creation operator $b^\dagger$ and frequency Ω. These vibration states are strongly coupled to the electronic state of the dye, with the interaction being parameterised by the Huang-Rhys factor S and emission and absorption rates $\Gamma_m^{e/a}$ into and out of the photonic mode m.

We denote a_m the annihilation operator of each photonic mode, σ_i the Pauli operators corresponding to the i-th dye molecule, g the coupling strength of the photon-dye interaction and write the Hamiltonian as

$$\begin{aligned} H = &\sum_m \omega_m a_m^\dagger a_m + \sum_i \frac{\omega_d}{2}\sigma_i^z + g\sum_{m,i}\left(a_m\sigma_i^+ + a_m^\dagger\sigma_i^-\right) \\ &+ \Omega\left(b_i^\dagger b_i + \sqrt{S}\sigma_i^z(b_i + b_i^\dagger)\right). \end{aligned} \tag{5.1}$$

The first and second terms correspond to the free energy of photons and dye molecules, respectively. The third term is the light-matter interaction, where the rotating wave approximation was made to ensure the conservation of the excitation number. The last term corresponds to the interaction of photons with the phonons in the dye. We only take one phonon mode (per dye molecule) into account, but the calculation can be extended to consider more vibrational modes [97]. The dye-phonon coupling is strong, but it can be dealt with using a polaron transformation $H \to U^\dagger H U$ to eliminate the vibration degrees of freedom, where $U = \exp\left[\sum_i \sqrt{S}\sigma_i^z(b_i - b_i^\dagger)\right]$. The resulting Hamiltonian is

$$H = \sum_m \omega_m a_m^\dagger a_m + \sum_i \frac{\omega_d}{2}\sigma_i^z + \Omega b_i^\dagger b_i + g\left(a\sigma_i^+ D_i + a^\dagger \sigma_i^- D_i^\dagger\right), \tag{5.2}$$

where $D_i = \exp[2\sqrt{S}(b_i^\dagger - b_i)]$ are displacement operators.

In the polaron basis, the interaction can be understood to link the absorption (emission) of a photon to the excitation (decay) of a dye molecule with a certain displacement. This corresponds to exciting a particle from one of the lower states of the dye to one of the upper ones depicted in Fig. 5.1. The coupling constant g can be treated perturbatively, resulting in an evolution governed by the master equation

$$\begin{aligned}\dot{\rho} = -i[\tilde{H}_0, \rho] - \sum_{i,m} \Big\{ &\frac{\kappa}{2}\mathcal{L}[a_m] + \frac{\Gamma_\uparrow}{2}\mathcal{L}[\sigma_i^+] + \frac{\Gamma_\downarrow}{2}\mathcal{L}[\sigma_i^-] \\ &+\frac{\Gamma_m^e}{2}\mathcal{L}[a_m^\dagger \sigma_i^-] + \frac{\Gamma_m^a}{2}\mathcal{L}[a_m \sigma_i^+]\Big\}\rho,\end{aligned} \tag{5.3}$$

where the symbol $\mathcal{L}$ corresponds to Lindblad dissipators. We have added radiative decay with rate κ and excitation (decay) due to an incoherent pump source with rate $\Gamma_\uparrow$ ($\Gamma_\downarrow$). The last two terms correspond to the emission and absorption of photons by the dye, obtained with the Born-Markov and secular approximations on the interaction term in Eq. (5.2). These emission and absorption rates $\Gamma_m^e = \Gamma(-\delta_m)$ and $\Gamma_m^a = \Gamma(\delta_m)$ are functions of the detuning $\delta_m = \omega_m - \omega_d$, and are obtained from the Fourier transform of the retarded correlation function of displacement operators broadened by the incoherent pump (for more details see [5, 97]), $\Gamma(\delta) = 2\mathrm{Re}[K(\delta)]$, where

$$K(\delta) = g^2 \int_0^\infty dt \langle D_i^\dagger(t) D_i(0)\rangle \mathrm{e}^{-(\Gamma_\uparrow + \Gamma_\downarrow)|t|/2} \mathrm{e}^{-i\delta t}. \tag{5.4}$$

They are plotted in Fig. 5.1(b) and, for small frequency detuning, they follow the Kennard-Stepanov relation $\frac{\Gamma_m^e}{\Gamma_m^a} = e^{-\beta_{\text{dye}}\delta_m}$ with β_{dye} being the inverse temperature of the dye. At larger frequency detunings the incoherent pump acts as a white noise, affecting the emission to absorption rates.

The first term in Eq. (5.3) corresponds to the unitary dynamics of a renormalized Hamiltonian

$$\tilde{H}_0 = \sum_{m,i} \tilde{\delta}_m a_m^\dagger a_m + \eta_m a_m^\dagger a_m \sigma_i^+ \sigma_i^-, \tag{5.5}$$

with energy shifts given by $\eta_m = \mathrm{Im}[K(-\delta_m) - K(\delta_m)]$ and $\tilde{\delta}_m = \delta_m + \mathrm{Im}[K(\delta_m)]$. Following [97] we can neglect this term because, for small light-matter coupling, it does not affect the equation of motion used to describe the system.

In Fig. 5.1 and throughout the chapter we use realistic parameters based on [97], by considering a microcavity at room temperature $T_{\text{dye}} = 300\text{K}$ with 10^9 dye molecules with energy splitting $\omega_d = 558.3\text{THz}$, lowest mode detuning $\delta_0 = -100\text{THz}$, cavity mode decay rate $\kappa = 100\text{MHz}$, frequency of the rovibrational mode $\Omega = 5\text{THz}$, light-matter coupling strength $g = 1\text{GHz}$, Huangs-Rhys factor $S = 0.5$, relaxation rate $\gamma = 50\text{THz}$, decay of excited electronic state $\Gamma_\downarrow = 1\text{GHz}$. However, we have considered a smaller cavity mode spacing of $\epsilon = 0.25\text{THz}$, following the experimental value in [4].

We can calculate the population dynamics by considering a large number of dye molecules N_d and making a semi-classical approximation on the number of photons per mode $n_m = \langle a_m^\dagger a_m \rangle$. This leads to the rate equations

$$\dot{n}_m(t) = -\kappa n_m + N_d \left[\Gamma_m^e (n_m + 1) p_e - \Gamma_m^a n_m (1 - p_e)\right], \tag{5.6}$$

$$\dot{p}_e(t) = -\Gamma_\downarrow^{\text{tot}} p_e + \Gamma_\uparrow^{\text{tot}} (1 - p_e), \tag{5.7}$$

where p_e is the probability of the dye being on the excited state, and the total rates of excitation and decay of the two level system are:

$$\Gamma_\uparrow^{\text{tot}} = \Gamma_\uparrow + \sum_m g_m \Gamma_m^a n_m, \tag{5.8}$$

$$\Gamma_\downarrow^{\text{tot}} = \Gamma_\downarrow + \sum_m g_m \Gamma_m^e (n_m + 1). \tag{5.9}$$

Figure 5.2 shows the evolution of the distribution of photons calculated with Eqs. (5.6) and (5.7) for values of pump rate $\Gamma_\uparrow$ below and above the condensation threshold. Starting with a microcavity empty of photons, the pump excites the

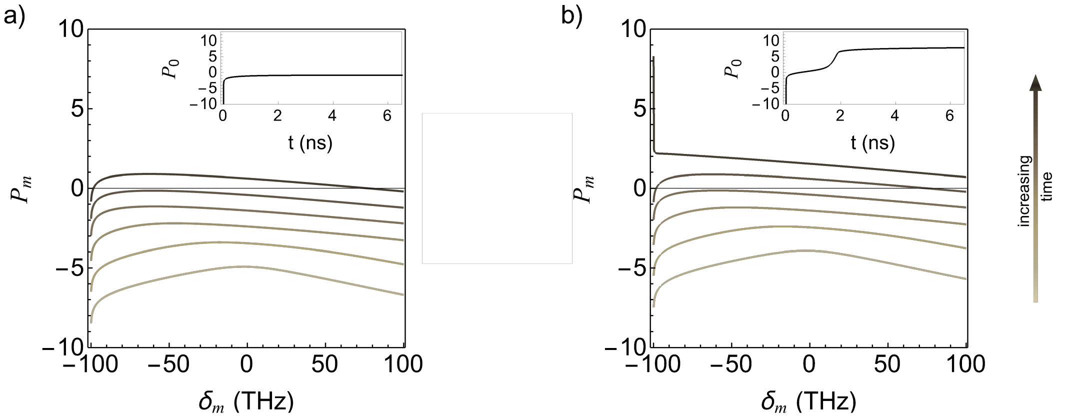

Figure 5.2: Logarithm of the population occupation of photons $P_m = \log_{10}(g_m n_m)$ for different times, with time towards the steady-state for a $\Gamma_\uparrow$ (a) below and (b) above the threshold. The insets show the time evolution of the population in the ground state, P_0.

dye molecules, and the early time distributions reflect the bare fluorescence spectrum dominated by photons in resonance with the dye. With time, as the emission and absorption processes occur repeatedly, thermalisation begins to happen. The thermalisation takes longer for the modes that are further away from resonance because the emission and absorption rates are lower at those frequencies. In fact, thermalisation can even break down if the cavity is such that the lower energy modes have scattering rates comparable to the losses [97].

When the cavity losses and pump rates can be neglected, the steady state of Eqs. (5.6) and (5.7) is such that

$$\frac{n_m + 1}{n_m} = e^{\beta_{\rm dye}\delta_m} \frac{\Gamma_\downarrow^{\rm tot}}{\Gamma_\uparrow^{\rm tot}}, \tag{5.10}$$

which allows us to define an effective chemical potential for the photon gas such that $e^{-\beta_{\rm dye}\mu} = \frac{\Gamma_\downarrow^{\rm tot}}{\Gamma_\uparrow^{\rm tot}}$. While in the thermodynamic limit, condensation is expected to happen when $\mu = \delta_0$, in the following we consider a finite system in which the chemical potential only approaches δ_0, and the total number of photons is

$$N_{\rm ph} = \frac{1}{6}\left(\frac{\pi}{\epsilon\beta_{\rm dye}}\right)^2. \tag{5.11}$$

5.2 Nonequilibrium thermodynamics: heat engines and the second law

In this section, we show that although photons can reach a condensed equilibrium distribution in steady state, their nonequilibrium nature still provides information about the threshold condition. Because of the energy and particle fluxes on the steady state of the quantum gas, the condensate formation has thermodynamic constraints. In its condensed state, the system operates as a thermal machine whose output work is coherent light. As in the case of polaritons, condensation must respect the second law of thermodynamics, and so it requires positive entropy production.

In the experiment, an energy source excites the dye, generating excitation and a non-radiative decay. This can be identified as a hot reservoir in contact with the two-level system, with inverse temperature β_h defined by the rate $e^{-\beta_h \omega_d} = \frac{\Gamma_\uparrow}{\Gamma_\downarrow}$. The dye repeatedly emits and reabsorbs photons with rates that follow the Kennard-Stepanov relation, so the photons thermalise with the phonon temperature. Therefore, phonons can be seen as a cold reservoir. Furthermore, by the same argument of that of the last chapter, the interaction between the dye and the photon ground state will be work if the state is macroscopically occupied.

Using Eqs. (5.6) and (5.7) we obtain the rate of particles into (γ^e) and out of (γ^a) the condensate mode

$$\frac{\gamma^e}{\gamma^a} = \frac{\Gamma_0^e \, p_e}{\Gamma_0^a \, p_g} = \frac{\Gamma_0^e \, \Gamma_\uparrow^{\text{tot}}}{\Gamma_0^a \, \Gamma_\downarrow^{\text{tot}}}. \tag{5.12}$$

The second equality is obtained by substituting the steady state values of the electronic occupation. This equation is equivalent to Eq. (5.10). To achieve condensation the emission rate must balance the absorption rate and the losses, $\frac{\gamma^e}{\gamma^a} \geq 1$.

Using the conservation of the total number of particles in the steady state

$\sum_m g_m \dot{n}_m = 0$, we find an expression for $\Gamma_\uparrow^{\text{tot}}$ and substitute in Eq. (5.12)

$$\frac{\gamma^e}{\gamma^a} = \frac{\Gamma_0^e}{\Gamma_0^a}\left(\frac{\Gamma_\uparrow}{\Gamma_\downarrow} - \frac{N_{\text{ph}}\ \kappa}{N_d\ p_g\ \Gamma_\downarrow}\right) = e^{-\beta_{\text{dye}}\delta_0}\left(e^{-\beta_h\omega_d} - \frac{N_{\text{ph}}\ \kappa}{N_d\ p_g\ \Gamma_\downarrow}\right). \tag{5.13}$$

We can associate an effective temperature β_{eff} to the transition and write $e^{-\beta_{\text{eff}}\omega_0} = \frac{\gamma^e}{\gamma^a}$. Taking the logarithm and approximating $\kappa \approx 0$ gives

$$\beta_{\text{eff}}\omega_0 = \beta_{\text{dye}}\delta_0 + \beta_h\omega_d + \frac{N_{\text{ph}}\ \kappa}{N_d\ p_g\ \Gamma_\uparrow}. \tag{5.14}$$

This expression connects the physics of condensation to that of a heat engine. The left-hand side can be interpreted as the entropy increase in the ground state when a particle is added to it. Taking the limit of $\kappa \to 0$ the terms on the right-hand side correspond to the flow of entropy per cycle in the working medium of a thermal machine in contact with two reservoirs [46]. Specifically, the first and second terms correspond to the entropy change in the working medium due to the exchanges of energies δ_0 and ω_d with the reservoirs with inverse temperature β_{dye} and β_h, respectively. Equation (5.14) has three relevant energy quanta, thereby we can map it to the thermodynamics to that of a three-level heat engine, as in Fig. 5.3(a). The threshold for condensation $\frac{\gamma^e}{\gamma^a} = 1$ corresponds to $T_{\text{eff}} = \infty$. This is in accordance with the definition of heat and work we have been using [15] in which work is energy exchanged reversibly. The threshold for condensation is the reversible limit of the heat engine, where the Carnot limit is achieved

$$T_h^{\text{rev}} = -T_{\text{dye}}\frac{\omega_d}{\delta_0}. \tag{5.15}$$

If $\kappa \neq 0$, the threshold requires that the emission into the condensate mode not only balances the absorption but also the loss rate, so $\frac{\gamma^e}{\gamma^a} > 1$. This is analogous to the requirement of inversion in a laser. The last term in Eq. (5.14) can be interpreted as an additional entropy change in the working medium due to the flow of particles in the system. In this case, the threshold temperature of the pump is higher than the one given by Eq. (5.15).

Figure 5.3(b) shows the steady state number of particles in the ground state

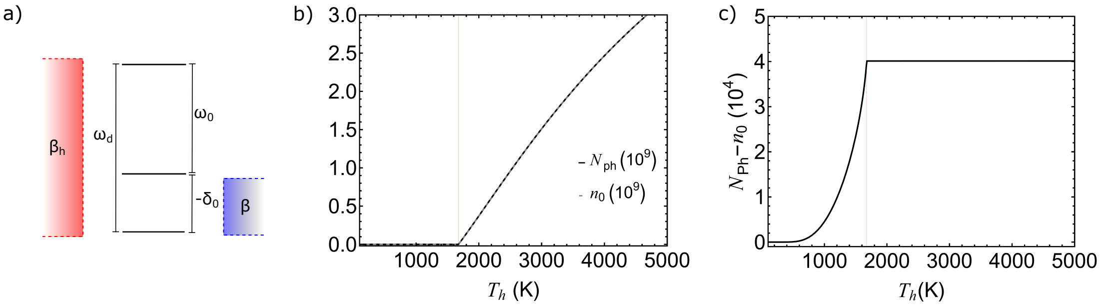

Figure 5.3: (a) Schematic illustration of the three-level heat engine described by Eq. (5.14). (b) Number of photons in the ground state and total number of photons in the microcavity as a function of the temperature of the hot reservoir (pump). (c) Total number of photons in the excited states of the microcavity as a function of T_h. The thermodynamic requirement for condensation, i.e., the reversible limit, is depicted as a red line. Above the threshold, the ground state becomes macroscopically occupied, and the number of particles in the excited states saturates to a maximum.

and the total number of particles in the photon gas as a function of the temperature of the hot reservoir (pump). The two curves are indistinguishable to the eye, so we also show their difference in Fig. 5.3(c). The red line shows the reversible limit of the heat engine. In the rest of the chapter T_h^{rev} will be plotted as a vertical red line in graphs of T_h as reference. We take a small but realistic value of decay rate for the cavity $\kappa = 100\text{MHz}$, so the phase transition happens near, but not precisely, at the reversible point.

Note that even though there are more particles in the gas with a hotter pump, at the condensed state, the difference $N_{\text{ph}} - n_0$ maintains a constant value. This shows that the excited photon states are fully occupied above the threshold, and any additional particle goes to the ground state.

5.3 Condensation pumped by a thermal source of light

In this section, we examine the effects of modifying the pump by incorporating thermal sources, such as sunlight. Studies have shown that a dye-filled cavity can cool photons generated by a thermal source, resulting in a decrease in phase-space volume; however, condensation has not yet been observed under these conditions [92]. Our aim is to investigate the influence of a thermal pump in order to determine effective approaches for achieving condensation.

We treat the thermal pump as the result of an interaction with a blackbody with inverse temperature β_h. The equations of motion, (5.6) and (5.7), become

$$\dot{n}_m(t) = \kappa \left[e^{-\beta_h \omega_m}(n_m + 1) - n_m \right] + N \left[\Gamma^e_m (n_m + 1) p_e - \Gamma^a_m n_m (1 - p_e) \right], \tag{5.16}$$

$$\dot{p}_e(t) = -\Gamma^{\text{tot}}_{\downarrow} p_e + \Gamma^{\text{tot}}_{\uparrow} (1 - p_e). \tag{5.17}$$

In this case the pump affects $\dot{n}_m$ directly, instead of $\dot{p}_e$. To distinguish and compare the two experimental scenarios, we refer to the first as a photon-pumped and the second as a dye-pumped microcavity. Here, the total rates $\Gamma^{\text{tot}}_{\downarrow/\uparrow}$ are entirely due to the interaction of the dye with light. We split these to account for the interaction with the condensate mode separately:

$$\Gamma^{\text{tot}}_{\uparrow} = \sum_{m=0} g_m \Gamma^a_m n_m = \Gamma^a_0 n_0 + \Gamma^{\text{S}}_{\uparrow}, \tag{5.18}$$

$$\Gamma^{\text{tot}}_{\downarrow} = \sum_{m=0} g_m \Gamma^e_m (n_m + 1) = \Gamma^e_0 (n_0 + 1) + \Gamma^{\text{S}}_{\downarrow}. \tag{5.19}$$

To study separately the possible effects of a thermal pump, we start with a simplified model of a photon gas with only two energy levels. Next, we extend the model to the case of a multimode blackbody source pumping many modes of light. We compare the efficiencies of the dye-pumped condensate presented in the last sections with a condensate pumping on the photon energies by a multimode source. Here, we establish theoretical conditions for condensation in solar-pumped dye-filled microcavity that could indicate a pathway to an experimental realisation.

5.3.1 A two-level photon gas

In the case of a dye-pumped photon gas, we showed that only three energy levels are relevant in the calculation of the thermodynamic threshold. This suggests that we can investigate some of the effects of different energy pumps by considering a few-level photon gas. We use a toy model where the photons can only occupy the ground state and another state that is affected by the pump.

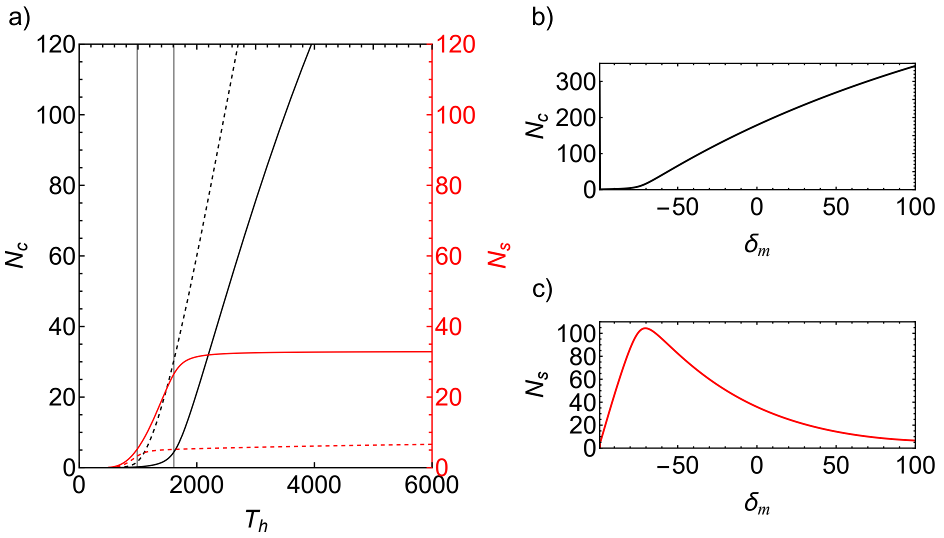

Figure 5.4: Steady-state behaviour of the two-level photon gas.(a) Number of particles in the condensate N_c and in the extra level N_s as a function of the temperature of the hot reservoir, with the extra level having energy detuning $\delta_m = 5$meV (solid), and $\delta_m = 100$meV (dashed). The grey line shows the reversible limit, of thermal machines with energies 0, ω_s, $\omega_s - \omega_0$. (b) Number of particles in the condensate and (c) in the extra level for various energies of the extra level.

The dynamics of the dye-photon system are given by Eqs. (5.16) and (5.17), with the index m accounting for 0 and the additional level. The different choices of the extra level affect the energy gaps and the total number of modes of light, as the degeneracy grows linearly with the energy of the level.

Figure 5.4 shows the steady-state behaviour of the two-level photon gas. In (a), the number of particles in the “condensate” N_c and in the extra level N_s are shown as a function of the temperature of the hot reservoir for two different choices of levels with energy detunings $\delta_m = 5$meV and $\delta_m = 100$meV, in solid and dashed lines respectively. The grey lines show the reversible limit of a three-level heat engine with energy levels 0, ω_s, $\omega_s - \omega_0$. The one on the left is that of the case with the largest energy detuning.

A condensation threshold cannot be clearly defined for such a small system, however, the curves show a saturation of the occupation of the excited level above the reversible limit. This mismatch between the reversible limit and the saturation point can be attributed to both the finite size of the system and the cavity losses, which we have taken to be $\kappa = 0.01\text{ps}^{-1}$ here. Figs. 5.4(b) and

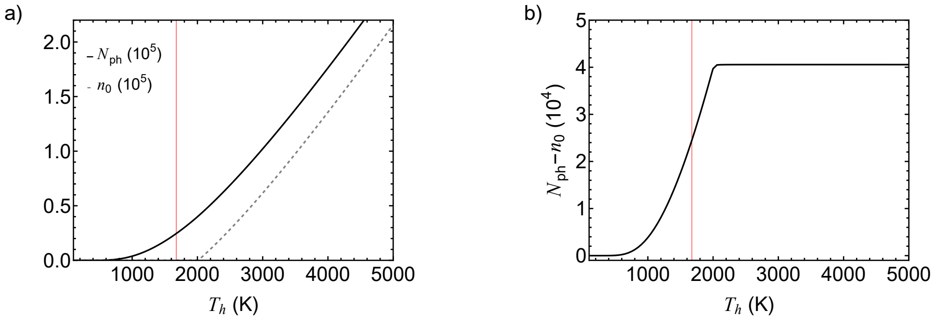

Figure 5.5: (a) Number of photons in the ground state and total number of photons in the microcavity as a function of the temperature of the hot reservoir (pump). (b) Total number of photons in the excited states of the microcavity as a function of T_h. The reversible limit is depicted as a red line for comparison. The phase transition happens smoothly, and above the threshold, the ground state becomes macroscopically occupied, and the number of particles in the excited states saturates.

(c) show the steady-state number of particles in the condensate and in the extra mode, respectively, varying the energy of the extra mode and fixing $T_h = 6000$K.

A comparison between the two results in Fig. 5.4(a), and the curve shown in Fig. 5.4(b) suggests that when pumped at larger energies, condensation has a lower threshold and higher condensate fraction. The increased degeneracy of the higher energy modes may be one of the sources of this effect, however, the non-monotonicity of the curve in Fig. 5.4(c) suggests that there might be other effects coming into play.

5.3.2 Solar-pumped multimode model

In this section, we continue to explore the effects of pumping the microcavity with thermal sources, studying a multimode pump described by equations Eqs. (5.16) and (5.17), with $m = 0, ..., 800$.

Following the same steps as for the dye-pumped case, we calculate the number of photons in the condensate, the total number of photons and the evolution of the distribution to the steady state. Those results are shown in Fig. 5.5 and Fig. 5.6. For comparison, the red line shows the reversible limit T_h^{rev} of Eq. (5.15). The total number of photons in Fig. 5.5(a) shows a phase transition that happens for a critical temperature above the reversible one, and the curve is noticeably smoother. The saturation of the excited photon states is reached at ≈ 2000K (see

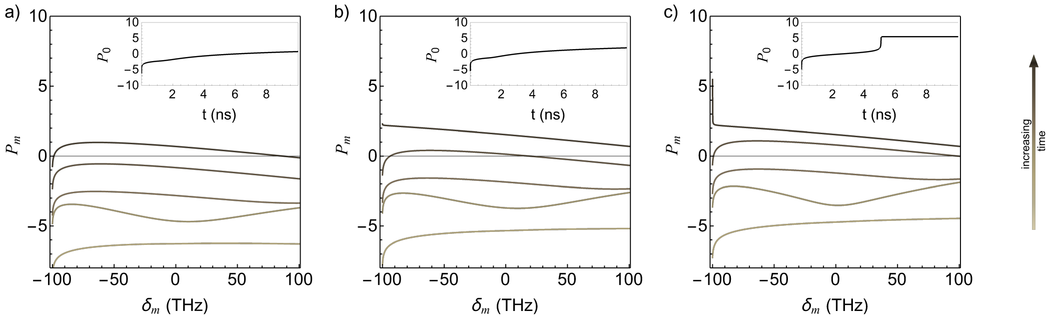

Figure 5.6: Logarithm of the population occupation of photons $P_m = \log_{10}(g_m n_m)$ for different times, up to the steady-state for a temperature T_h (a) far below the threshold (T_h = 1000K), (b) below, but near the threshold (T_h = 2000K), where a macroscopic population starts to emerge, but the gas is not yet condensed, and (c) above the threshold (T_h = 6000K). The insets show the time evolution of the population in the ground state, P_0.

Fig. 5.3(b)), proving that a condensed state can exist at temperatures smaller than the sun $T_{\text{sun}} \approx 5800$K. However, the number of particles in the gas is orders of magnitude lower than the dye-pumped condensate, and so the curves of N_{ph} and n_0 can be distinguished in the figure. That is because when pumping each dye molecule with a certain rate, the energy flux into the system is multiplied by the number of molecules (10^9), while in the multimode pump, the rate is multiplied by the number of photon modes ($\sim 3 \times 10^5$) and so the multimode photon pump effectively adds fewer photons into the system.

The evolution of the photon distribution is shown in Fig. 5.6 for three different hot temperatures: (a) 1000K, lower than the threshold of condensation with the dye pump, (b) 2000K, higher than the threshold of condensation with the dye pump, but lower than the threshold of condensation in this case and (c) 6000K, higher than the threshold for condensation. The pump generates photons, and so, at early times, the distribution reflects the first absorption of the dye, which is greater near resonance. For longer times, the repeated absorption and re-emission lead to thermalisation. Because the rates depend on the frequency, thermalisation is faster in modes near resonance, and the ground state is the last to reach a steady state. From left to right, the steady-state distributions are that of a normal thermal gas, of a gas with a macroscopic population of photons spread over many modes, and of a Bose condensed quantum gas. The insets show the time evolution of the ground state population. In Fig.(c) condensation happens

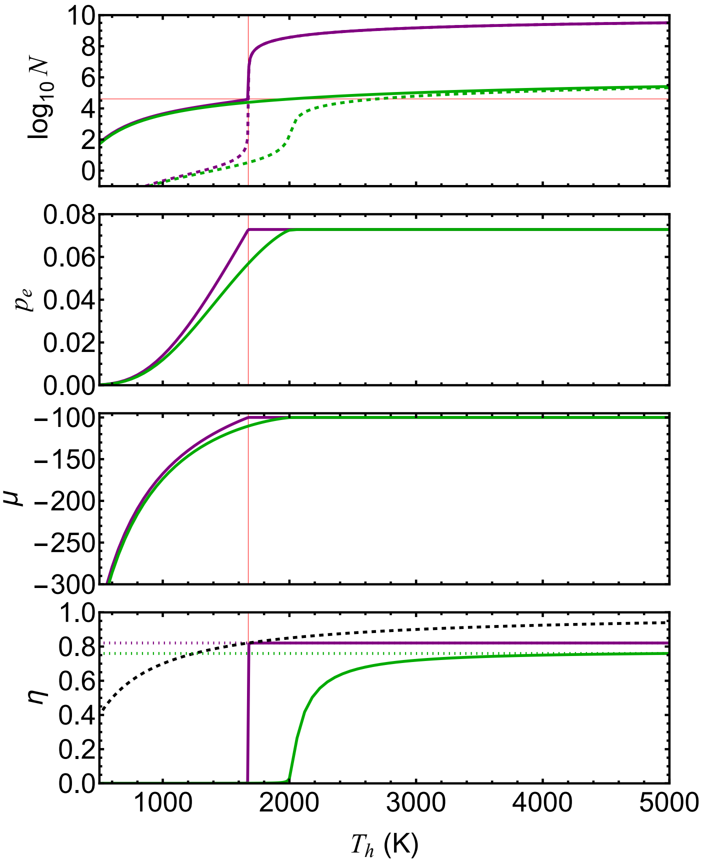

Figure 5.7: Steady state of a photon condensate pumped on the dye populations (purple) and a multimode source of blackbody radiation (green) at temperature T_h. From top to bottom, the graphs show the total number of particles (solid) and number of particles in the ground state (dashed) on a log scale, the probability of finding a dye molecule in the excited state, the chemical potential of the photon gas, and efficiency of the thermal machine. In the bottom figure, the dashed line shows the Carnot efficiency, and the purple (green) dotted lines are the calculated (estimated) limit of the dye-pumped (photon-pumped) condensate. The red vertical line is the reversible limit of the dye-pumped condensate, where the efficiency reaches Carnot's. The multimode pump has a less sharp phase transition, with higher T_h at the threshold. The efficiency does not achieve the Carnot limit, remaining below the other case even after the threshold.

after ∼ 5ns, where a jump is seen in the evolution of P_0.

Following a similar procedure as to the dye-pumped condensate, we find the rate of emission by absorption of the dye into the condensate mode

$$\frac{\gamma^e}{\gamma^a} = \frac{\Gamma_0^e}{\Gamma_0^a}\left\{\frac{\Gamma_\uparrow^{\mathrm{S}}}{\Gamma_\downarrow^{\mathrm{S}}} - \frac{\kappa}{N_d\ p_g\ \Gamma_\downarrow^{\mathrm{S}}}\left[n_0 - e^{-\beta_h\omega_0}(n_0+1)\right]\right\}. \tag{5.20}$$

Associating an effective temperature to the transition $e^{-\beta_{\mathrm{eff}}\omega_0} = \dfrac{\gamma^e}{\gamma^a}$, taking the logarithm and making the approximation $\kappa \approx 0$, we get the entropy increase in the ground state when a particle is added to the condensate

$$\beta_{\text{eff}}\omega_0 = \beta_{\text{dye}}\delta_0 - \log\left(\frac{\Gamma^{\text{S}}_{\uparrow}}{\Gamma^{\text{S}}_{\downarrow}}\right) + \frac{\kappa}{N_d\, p_g\, \Gamma^{\text{S}}_{\uparrow}}\big[n_0 - e^{-\beta_h\omega_0}(n_0+1)\big]. \tag{5.21}$$

This expression is similar to Eq. (5.14), however, the interpretation is not as straightforward. The first term is the entropy change corresponding to energy transfer from the working medium to the cold bath. Motivated by fluctuation theorems [46] the second term can be interpreted as the entropy increase in the working medium due to energy being transfer to all modes of the photon gas but the ground state. This involves entropy and energy exchange with both hot and cold reservoir, and so a break down of the expression as in Eq. (5.14) is not possible. The threshold when $\kappa \to 0$ is when the left hand side of Eq. (5.21) is zero, that is, when $\frac{\Gamma^{\text{S}}_{\uparrow}}{\Gamma^{\text{S}}_{\downarrow}} = e^{-\beta_{\text{dye}}\delta_0}$. However, this is not the reversible limit of the heat engine. As discussed below, the thermal pump excites many modes of light, allowing transitions that cause heat transfer from the hot to the cold bath without producing work.

In Fig. 5.7, we show, in purple and green, the behaviour of the dye-photon system as a function of the temperature T_h of a dye-pumped and photon-pumped microcavity, respectively. As in Figs. 5.3 and 5.5, the graph at the top shows the total number of particles in the gas (solid line) and the number of particles in the ground state (dashed line), but on a logarithmic scale. Because $\kappa \ll \Gamma^{\text{S}}_{\uparrow}$, the threshold of the dye-pumped condensation coincides with the reversible line of the three-level heat engine (vertical red line), where we see a jump on both N_{ph} and n_0. When the photon gas is pumped with sunlight, the total number of particles is not as large as that of a dye-pumped cavity, but it can reach the threshold value Eq. (5.11) shown as a horizontal red line. In this case, the threshold is when $\sqrt{N_{\text{ph}}} \approx n_0$, at approximately 2000K.

At temperatures above the threshold, both the probability of finding a dye molecule in the excited state and the chemical potential of the photon gas reach the estimated value for a condensate (calculated assuming the thermodynamic limit). However, the temperature T_h required for condensation is higher for a gas with a thermal pump and the phase transition is smoother.

The bottom graph of Fig. 5.7 shows the efficiency of condensation, i.e., the work output divided by the heat input in the system. For the dye-pumped microcavity (depicted in purple) the efficiency is

$$\eta_{\text{res}} = \frac{\kappa\omega_0 n_0}{N_d\omega_d(\Gamma_\uparrow p_g - \Gamma_\downarrow p_e)} = \frac{\omega_0 R^0_{\text{out}}}{\omega_d R_{\text{in}}}, \tag{5.22}$$

where R^0_{out} is the rate at which particles escape from the condensate and R_{in} the rate at which energy is added to the dye. The steady state condition is that the rates of particles in and out of the cavity are the same, but because in the condensed state $n_0 \approx N_{ph}$, we can consider that the particles escaping the cavity are almost entirely in the ground state, and the efficiency can be approximated to $\eta_{\text{res}} = \frac{\omega_0}{\omega_d}$. This is depicted as a purple dotted line in the figure.

In the thermal multimode setup, the efficiency (depicted in solid green) is

$$\eta_{\text{mm}} = \frac{-\omega_0(n_0 - e^{-\beta_h\omega_0}(n_0+1))}{\sum_{m=1} g_m\omega_m(n_m - e^{-\beta_h\omega_m}(n_m+1))} = \frac{\omega_0 R^0_{\text{out}}}{\sum_{m=1}\omega_m R^m_{\text{in}}}, \tag{5.23}$$

where R^m_{in} is the rate at which photons are added to the m-th energy level. To compare with Eq. (5.22) we can write the frequencies in terms of the detuning with respect to ω_d, which gives

$$\eta_{\text{mm}} \approx \frac{\omega_0}{\langle\delta\rangle + \omega_d}, \tag{5.24}$$

where $\langle\delta\rangle = \frac{\sum_m R^m_{\text{in}}\delta_m}{\sum_m R^m_{\text{in}}}$, and again because most particles are in the ground state, in the steady state $\sum_m R^m_{\text{in}} \approx R^0_{\text{out}}$. We use the rates R^m_{in} calculated in a well developed condensed state (T_h = 5000K) to estimate η_{mm}, and plot this in a green dotted line in Fig. 5.7. Because $\langle\delta\rangle > 0$, Eq. (5.24) gives an efficiency lesser than Eq. (5.22). We suggest this is because, when the hot reservoir couples to multiple transitions, it enables energy to be exchanged between the hot and cold reservoir without producing work. This can be seen in Figure 5.8, where we show the heat currents when the cavity has a source pumping the dye (a) and the photon modes (b). The reversible line (red vertical line) is at the threshold temperature of operation of the dye-pumped thermal machine T_h^{rev}. However, at

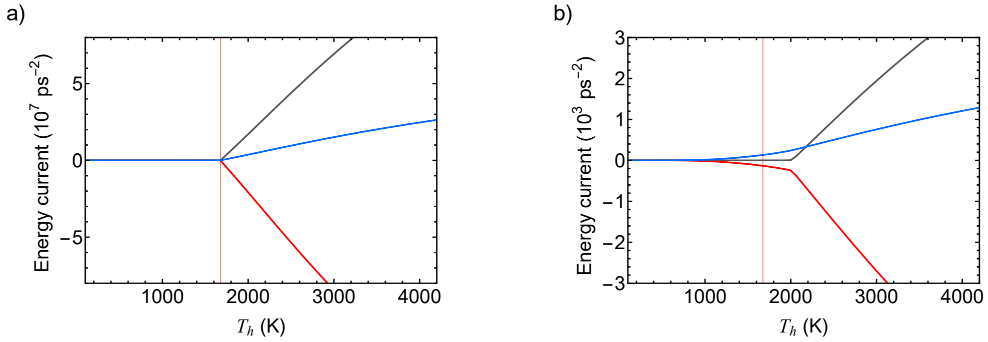

Figure 5.8: Energy currents of a (a) dye-pumped and (b) with a photon-pump microcavity. In red and blue are the energy current to the hot, and cold baths, respectively, and in black the output condensate power. The red vertical line is the reversible limit of Eq. (5.15), which sets the threshold temperature of the heat engine. At the same temperature, in the multimode photon-pumped cavity there is heat flowing from the hot to cold baths, but no output power.

this same temperature, the multimode pump produces energy currents from the hot to the cold baths without output power, i.e, without condensation. We show Carnot's efficiency as the dashed black curve. It is equal to the efficiency of the dye-pumped condensate at the threshold (red line).

Due to the smoother nature of the phase transition, it becomes more difficult to clearly identify a condensation threshold when the system is driven by a multimode source. We follow the approach taken in [97] in which the threshold is defined by the point at which the number of photons in the cavity reaches the critical value in Eq. (5.11) predicted for the equilibrium Bose gas. In equilibrium, this would correspond to a ground state population of $n_0 = 1/\beta\epsilon$ to leading order on ϵ. In Ref. [97] the authors generalise this definition to account for nonequilibrium cases in which the occupation of the ground state is not the highest $n_{\max} = \max\{n_m\} = 1/\beta\epsilon$. This approach has the advantage of distinguishing macroscopic ($n_0 \sim N_{ph}$) and microscopic ($n_0 \sim 1$) occupation of the ground state.

In Fig. 5.9 we show how the threshold, defined in two slightly different ways, depends on the coupling κ. In the top row it is defined as the point at which the total number of photons in the cavity reaches the critical value given by Eq. (5.11). In the bottom row, the threshold is when the population of the maximally occupied state reaches $n_{\max} = 1/\beta\epsilon$. These two definitions are equivalent in the

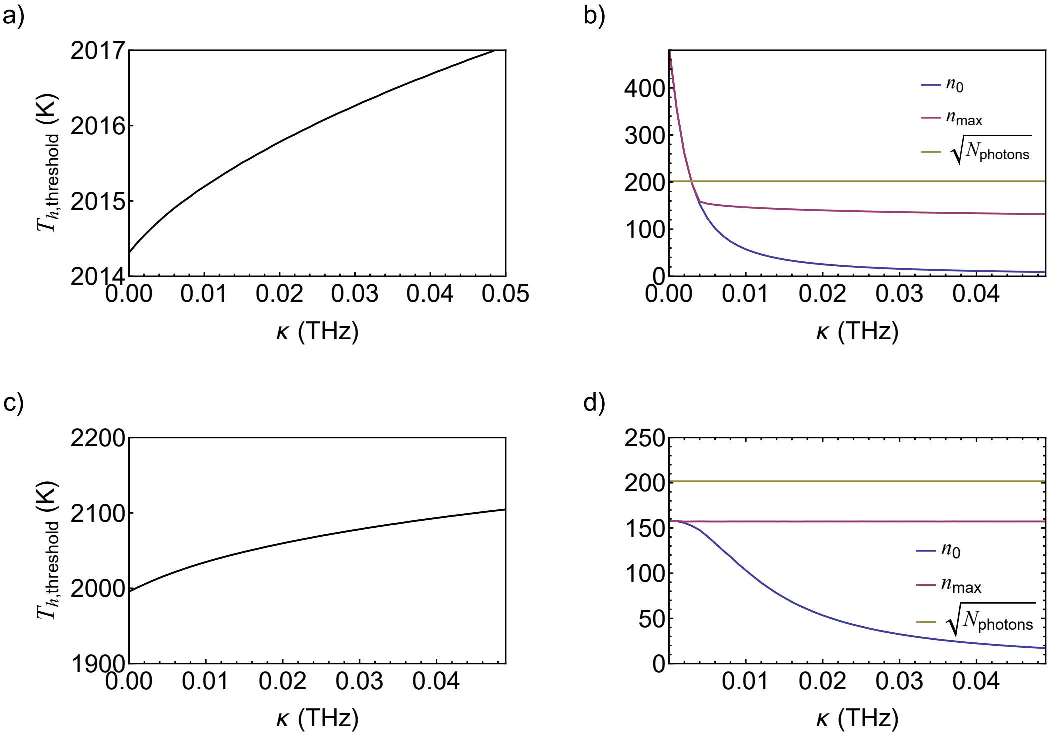

Figure 5.9: Threshold behaviour as a function of the coupling with the light source. In the top row, the threshold is defined by the point at which the number of photons reaches $N_{\text{threshold}}$ (see Eq. (5.11)), and in the bottom row it is given by $n_{\text{max}} = \max\{n_m\} = 1/\beta\epsilon$. (a) and (c) show the T_h at threshold, and (b) and (d) show the number of particles in the ground state, in the most occupied state and the square root of the total number photons. At higher coupling strengths, the systems is further away from equilibrium, so the ground state does not have the highest occupation.

thermodynamic limit ($\epsilon, \kappa \to 0$), [97], however in this finite system they differ slightly.

In Figs. 5.9 the threshold temperature of the pump varies by $\sim$ 4K in (a) and $\sim$ 130K in (c) for the values of coupling strength considered. Despite this difference, in reference to the absolute values of temperature these are small variations ($\sim$ 0.002% and $\sim$ 5%), which shows that the coupling has a weak effect on the phase boundary. Figures (b) and (d) show the number of particles in the ground state, in the most occupied state, and the square root of the total number photons, for the same values of κ. At higher couplings the system gets away from equilibrium, so the ground state is not the one with the highest occupation. We conclude that, in an experimental setting, the coupling can be taken to be arbitrarily small, while the temperature of the source should be kept large.

5.4 Conclusions

In this chapter, we showed that the nonequilibrium nature of a photon gas provides important information on the condensation threshold. Because of the energy and particle flow, a photon condensate operates as a heat engine, like a laser or polariton condensate, converting energy from the pump into work from the condensate. Therefore, as any thermal machine, it must respect the laws of thermodynamics and has its operation constrained by the rate of entropy produced. This constitutes a way to identify the threshold that is somewhat different from that broadly used for equilibrium BEC.

We focused on a model of a dye-filled cavity and linked the threshold criterion to the entropy balance in a reversible heat-engine cycle. We then extended the model to different possibilities of pump, first looking at a model of a two-level photon gas, and later at a multimode model pumped with sunlight. The results show how condensation could be achieved with thermal sources and that it could occur for excitation with sunlight. Such a solar-pumped condensate is an all-optical heat engine with a predicted efficiency of up to 0.8. However, our results suggest that the spread in the energy of the pump leads to lower efficiency. Additionally, we concluded that condensation can happen for arbitrarily small couplings with the light source, as the temperature of the source is the defining parameter to reach the threshold.

We considered a dye-filled cavity for definiteness, but our results are general and can be applied to other systems with rates obeying the Kennard-Stepanov relation. In further investigations, it would be interesting to link our findings to the thermodynamic analyses of the efficiency of conventional photovoltaic cells, such as the results in [99]. Additionally, we could continue to explore the model of a two-level photon gas to understand the precise role of the degeneracy and of other possible effects.

Chapter 6

Universality of coherent phenomena

IN WHICH WE ANALYSE THE CONNECTION BETWEEN
CONDENSATION, LASING, AND SYNCHRONISATION

In the previous chapters, we have shown that both polariton and photon condensates can be described using a three-level model of a heat engine. This model was first suggested by Scovil and Schulz-DuBois [14] to describe a maser and further discussed in other analyses of light amplification [15, 17, 18, 100]. In this way, our work supports the notion that these condensates are fundamentally analogous to laser phenomena. This equivalence had already been accepted in the literature in view of the fact that they emerge from the same effect, i.e., phase symmetry breaking, which implies common properties such as the macroscopic occupation of the ground state and a large range of phase order and spatial coherence [11].

While equivalent in certain fundamental aspects, the distinction between BEC and laser terminology is useful for describing the extent to which non-equilibrium effects influence the system. The usual categorisation involves the rate between the typical thermalization times, $\tau_{\rm th}$ and the lifetime τ_0. If $\tau_{\rm th}/\tau_0 << 1$, as is the case of photons in a dye-filled cavity, the system is able to thermalize with its environment and is characterised as BEC. On the other hand, if $\tau_{\rm th}/\tau_0 >> 1$ then amplification can happen, but particles escape before thermalizing with the environment, and the system is said to be in a laser phase. Moreover, there is a third regime, where the two-time scales are comparable (but $\tau_{\text{th}} \leq \tau_0$), and the system reaches a quasi-thermal equilibrium distribution; that is the typical case of polaritons which we call non-equilibrium condensates [8]. The temporal coherence is expected to increase with the particle-particle interactions and decrease with the particle lifetimes. Therefore, these different regimes have different degrees of temporal coherence, being greater for a condensate than for a laser [11].

In terms of state characterisation, it's important to note that there is no clear-cut transition between these different types of condensates in an experimental setting. Additionally, from a theoretical point of view, there is no symmetry breaking when moving from one regime to the other, so the states should not be considered to be in different phases of matter. In conclusion, for our purposes, the terms 'condensate' and 'lasing' will be used interchangeably from now on to refer to a state characterised by a macroscopic occupation of polaritons or photons.

While both photon and polariton lasers result in light amplification, they are distinguished by the particles involved in their stimulated interactions. Photon lasers rely on the stimulated emission of photons, while polariton lasers employ stimulated scattering of polaritons. This difference might seem trivial, but it reflects the degree of light-matter coupling. For instance, a gas of polaritons in a microcavity at low density emits light from its many modes, acting as an LED. As the pump is increased and the density grows, the system transitions to a laser mode with coherent emission from the ground state of the polariton spectrum. Further density increase leads to phase-filling effects that diminish the exciton-photon coupling, causing the coherent emission to be a pure result of photonic stimulation. The threshold for this second transition is named Mott density [101].

Currently, photon lasers are widely used and technologically well-established. However, polariton lasers have recently emerged as a promising energy-efficient source of coherent light due to their threshold density being many order magnitudes lower than the fundamental limit set for semiconductor photon lasers [11]. In particular, electrically driven polariton lasers have been achieved at cryogenic temperature in GaAs microcavities [9] and at room temperature in a GaN system [10]. Electrically pumped devices have the advantage of being more experimentally controllable. Therefore, this achievement has profound practical implications paving the way for the next generation of laser technology [101].

Both polariton condensates and general laser phenomenon have been modelled using the Dicke model, which consists of a Hamiltonian that describes a set of atoms (two-level system) interacting with light in a microcavity [102, 103]. When the rotating wave approximation is considered in the light-matter interaction, the model is sometimes called the Tavis-Cummings model. While the full Dicke model exhibits a superradiant phase transition, the Tavis-Cummings model cannot produce superradiance when losses are considered. Instead, it can reach a coherent laser state provided that there is atomic inversion. The connection with superradiance has been analysed by Kirton and Keeling [104], where the transition from standard lasing to Dicke superradiance is obtained by changing the balance of the rotating and counter-rotating terms in the light-matter interaction. The authors obtained a phase diagram, showing that there is always a normal phase separating the two distinct regimes of coherent light emission.

Furthermore, the lasing phenomenon has also been linked to the phase-locking in arrays of underdamped Josephson junctions through a Dicke-type model, using the collective electronic polarisation as an order parameter [105]. The energy of the ensemble of oscillators, considered as two-level systems, is shown to be minimal when their polarisation is mutually coherent.

In this chapter, we aim to investigate the same connection but using an ensemble of three-level heat engines. Even though the term synchronisation has a broader use in the literature, we use it here interchangeably with phase locking. We start by looking at a mean-field description of the light-matter coupled equations and interpreting the effects of loss in its phase diagram. To do so we extend the Dicke model to a set of three-level systems. This is a classical limit of the dynamical system, but gives a starting point to the interpretation of definitions that become less clear on the quantum regime. Next, we simulate the asymptotic limit of the ensemble of identical heat engines coupled to a field and calculate their degree of synchronisation using measures proposed in the literature [106].

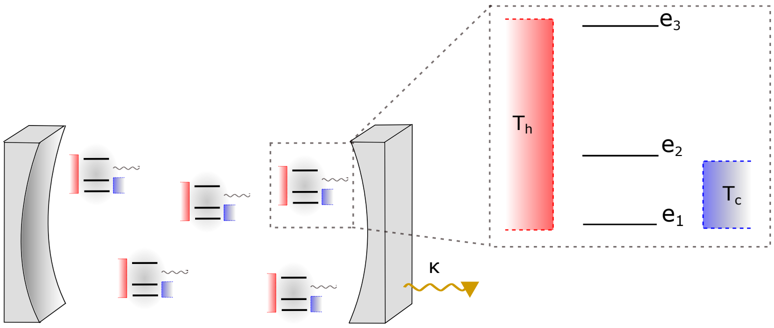

Figure 6.1: Cartoon illustration of a microcavity with an ensemble of three-level heat engines. The photon decay rate of the cavity is κ, and each three-level system is coupled to a hot and cold bath. The hot bath couples the levels 1 and 3, the cold bath couples the levels 1 and 2, and the interaction with the photons couples with the levels 2 and 3.

6.1 Mean-field approach

We consider an ensemble of N three-level heat engines in a microcavity, schematically represented in Figure 6.1. Each system interacts with different independent reservoirs described via the Lindblad master equation. The set of heat engines produces coherent light that competes with a photon loss due to the finite cavity lifetime. The Hamiltonian of the ensemble plus a photonic mode is

$$H = \sum_{j=1}^{N} \sum_{i=0}^{2} E_i \left|i\right\rangle_j \left\langle i\right|_j + \omega a^\dagger a + \frac{g}{\sqrt{N}} \sum_j \left[a^\dagger \left|2\right\rangle_j \left\langle 3\right|_j + a \left|3\right\rangle_j \left\langle 2\right|_j \right], \tag{6.1}$$

where a is the bosonic annihilation operator of photon, E_i the energy of each level, g is the strength of the light-matter interaction and we performed the rotating wave approximation on the last term. The interaction energy couples the two excited states of each system and is rescaled by a factor of $\sqrt{N}$ to guarantee a sensible description of the thermodynamic limit, i.e. a finite value of energy per heat engine. We define $E_1 = 0$, $\Delta E = E_3 - E_2$, $\bar{E} = \dfrac{E_3 + E_2}{3}$ and rewrite the Hamiltonian

$$H = \Delta E \sum_j \lambda_{3,j} + \bar{E}\sqrt{3} \sum_j \lambda_{8,j} + \omega a^\dagger a + \frac{g}{\sqrt{N}} \sum_j \left[a^\dagger \lambda_{1,j}^{-} + a \lambda_{1,j}^{+} \right]. \tag{6.2}$$

The Gell-Mann operators λ_k $(k = 1, ..., 8)$ are an analogous version of the spin

1/2 operators and are given by

$$\lambda_3 = \frac{1}{2}\begin{pmatrix} 1 & 0 & 0 \\ 0 & -1 & 0 \\ 0 & 0 & 0 \end{pmatrix}, \qquad \lambda_8 = \frac{1}{2\sqrt{3}}\begin{pmatrix} 1 & 0 & 0 \\ 0 & 1 & 0 \\ 0 & 0 & -2 \end{pmatrix}, \qquad \lambda_1 = \frac{1}{2}\begin{pmatrix} 0 & 1 & 0 \\ 1 & 0 & 0 \\ 0 & 0 & 0 \end{pmatrix}. \tag{6.3}$$

The transition operators connecting the two excited states of the three-level system are constructed in a similar way as to the spin 1/2, that is, $\lambda_1^+ = (\lambda_1^-)^T$ with $\lambda_1 = \dfrac{\lambda_1^- + \lambda_1^+}{2}$.

To simplify the problem, we follow a similar strategy to the one employed by Fowler-Wright et. al. [107] in the context of organic polaritons and use mean-field theory to reduce the problem to a single thermal machine interacting with a coherent field. In the limit of a large number of three-level systems $N \gg 1$, the bosonic operator a can be replaced by its average value, and each system experiences the interaction with a mean-field Hamiltonian

$$H_{3\mathrm{ls}} = \begin{pmatrix} e_3 & \frac{g}{\sqrt{N}}\langle a\rangle & 0 \\ \frac{g}{\sqrt{N}}\langle a\rangle^* & e_2 & 0 \\ 0 & 0 & 0 \end{pmatrix}. \tag{6.4}$$

Therefore, the evolution is described by coupled equations for each heat engine (indexed by j) and the average field $\langle a\rangle$

$$\begin{aligned} \dot{\rho}_j &= -i[H_{3\mathrm{ls}}(\langle a\rangle), \rho_j] + \mathcal{L}_h(\rho_j) + \mathcal{L}_c(\rho_j) \\ \dot{\langle a\rangle} &= -(i\omega + \gamma)\langle a\rangle - i\frac{g}{\sqrt{N}}\sum_j \langle \lambda_{1,j}^-\rangle. \end{aligned} \tag{6.5}$$

If the ensemble is in an unsynchronised state, the sum of the average transition operators $\langle \lambda_j^-\rangle$ is of order $\sqrt{N}$, and $\langle a\rangle$ is of order one. On the other hand, if the phase of each operator is locked at the natural frequency ω, the sum is of order N, meaning that $\langle a\rangle$ will be of order $\sqrt{N}$, which is a macroscopic state [105].

Taking the mean-field approximation over the spin 1 operators leads to

$$\langle \dot{\lambda}_{1,j}^{-} \rangle = -(i\Delta E + \Gamma^{-})\langle \lambda_{1,j}^{-} \rangle + 2i\langle a \rangle \langle \lambda_{3,j} \rangle \frac{g}{\sqrt{N}}, \tag{6.6}$$

where $\Gamma^{-} = \delta_h^{-} + \delta_c^{-}$ is the sum of the decay rates of the transitions coupled to the hot and cold baths. Then, we can write the average of all individual spin operators as $S_1^{-} = \sum_j \langle \lambda_{1,j}^{-} \rangle / N$ and $S_k^{-} = \sum_j \langle \lambda_{k,j} \rangle / N$, $(k = 1, ..., 8)$ to get

$$\begin{aligned} \dot{S}_1^{-} &= -(i\Delta E + \Gamma^{-})S_1^{-} + 2i\langle a \rangle S_3 \frac{g}{\sqrt{N}} \\ \langle \dot{a} \rangle &= -(i\omega + \gamma)\langle a \rangle - ig\sqrt{N} S_1^{-}. \end{aligned} \tag{6.7}$$

Now, the problem has been reduced to two coupled equations from which we can understand the underlying dynamics. The frequencies at which S_1^{-} and a oscillate are determined by their natural frequencies and the coupling term, which will enforce a tendency to synchronisation. Meanwhile, the loss terms Γ^{-} and γ need to be overcome so that the oscillators have a non-zero mean-field magnitude. In other words, two obstacles must be overcome to achieve a synchronised state. First, the losses need to be overcome allowing the systems to oscillate along their respective limit cycles. In mathematical terms, this is a Hopf bifurcation. Secondly, the interaction needs to be strong enough to ensure phase locking of the spin frequency with the field.

Decomposing each variable in its polar complex form $S_1^{-} = |S_1^{-}| e^{-i\theta_\lambda}$ and $\langle a \rangle = |a| e^{-i\theta_a}$ gives

$$\begin{aligned} |\dot{S_1^{-}}| &= -\Gamma^{-}|S_1^{-}| + 2\frac{g}{\sqrt{N}}|a| S_3 \sin(\theta_a - \theta_\lambda) \\ |\dot{a}| &= -\gamma |a| + g\sqrt{N}|S_1^{-}| \sin(\theta_a - \theta_\lambda) \end{aligned} \tag{6.8}$$

and

$$\begin{aligned} \dot{\theta}_\lambda &= \Delta E - 2g\frac{|a|}{\sqrt{N}|S_1^{-}|} S_3 \cos(\theta_a - \theta_\lambda) \\ \dot{\theta}_a &= \omega + g\frac{\sqrt{N}|S_1^{-}|}{|a|} \cos(\theta_a - \theta_\lambda), \end{aligned} \tag{6.9}$$

which can be used two analyse the two conditions for synchronisation separately. The dynamics of the phase difference $\Delta\theta = \theta_a - \theta_\lambda$ coincides with the classical equation of the Kuramoto model explained in chapter 2

$$\dot{\Delta\theta} = \Delta\omega + J\sin(\Delta\theta + \pi/2) \tag{6.10}$$

where $\Delta\omega = \omega - \Delta E$, and the effective coupling is

$$J = g\left(\frac{|S_1^-|\sqrt{N}}{|a|} + 2S_3\frac{|a|}{|S_1^-|\sqrt{N}}\right). \tag{6.11}$$

In the steady state $\dot{|a|} = \dot{|\lambda_1^-|} = 0$, so the effective coupling J reduces to $J = g\sqrt{\frac{2S_3}{\gamma\Gamma^-}}(\gamma+\Gamma^-)$ and $g = \frac{1}{\sin(\Delta\theta)}\sqrt{\frac{\gamma\Gamma^-}{2S_3}}$. At the normal state (and threshold) the value of S_3 depends uniquely on the thermal equilibration with the reservoirs and is given by

$$S_3\big|_{ns} = \frac{e^{-\beta_h e_3} - e^{-\beta_c e_2}}{2(1+e^{-\beta_h e_3} + e^{-\beta_c e_2})}. \tag{6.12}$$

The condition for synchronisation in the Kuramoto model is $\cos(\Delta\theta) = \Delta\omega/J$, which gives the critical coupling

$$g_c^2 = \frac{\gamma\Gamma^-}{2\,S_3\big|_{ns}}\left(1 + \left(\frac{\Delta\omega}{\gamma+\Gamma^-}\right)^2\right). \tag{6.13}$$

In the limit where both the radiative and non-radiative decay vanish, this is the classical Arnold tongue, demonstrated in chapter 2, in which $g_c \propto \Delta\omega$. Substituting Eq. (6.13) on the expression for J at the steady state we get that the critical effective coupling follows

$$J_c^2 = (\Delta\omega)^2 + (\gamma+\Gamma^-)^2. \tag{6.14}$$

This result has fundamental implications for the nature of the laser transition. It shows that, indeed, the classical limit of the laser phenomenon is intrinsically connected to the classical description of synchronisation. However the effective coupling depends on the magnitude of the spin and field. Because of the losses considered, the phase boundary acquires another dimension, and the typical “tongue" shape becomes a ‘cone’ in a space with dimensions $(x, y, z) = (\Delta\omega, \gamma+\Gamma^-, J_c)$, described by Eq. (6.14). The classical Arnold tongue corresponds to the section on the cone that crosses $\gamma + \Gamma^- = 0$. With a simple algebraic manipulation, we can also see that the Kuramoto condition is always achieved

$$\Delta\omega / J_c = \sqrt{1 - \left(\frac{\gamma + \Gamma^-}{J_c^2}\right)^2} < 1, \tag{6.15}$$

which shows that in fact, the existence of a limit cycle is the defining constraint of the problem. In other words, we conclude that as long as $|S_1^-|,\ |\langle a \rangle| > 0$, the oscillators are synchronised.

An interesting point to make is that if the light-matter interaction is in a regime in which the rotating wave approximation cannot be taken in the Hamiltonian of Eq. (6.1), the coupled equations (6.5) and (6.6) will have an additional term

$$\begin{aligned} \dot{\langle a \rangle} &= -(i\omega + \gamma)\langle a \rangle - 2i\frac{g}{\sqrt{N}}\sum_j \mathfrak{Re}\langle \lambda_{1,j}^- \rangle, \\ \dot{\langle \lambda_1^- \rangle} &= -(i\Delta E + \Gamma^-)\langle \lambda_{1,j}^- \rangle + 4i\langle \lambda_{3,j} \rangle \frac{g}{\sqrt{N}}\mathfrak{Re}\langle a \rangle. \end{aligned} \tag{6.16}$$

The evolution of the phase difference is not a Kuramoto-type equation, but given by

$$\dot{\Delta\theta} = \Delta\omega + \frac{J(t)}{2}\left[\sin(\Delta\theta + \pi/2) + \sin(\theta_a + \theta_\lambda + \pi/2)\right]. \tag{6.17}$$

Because of the additional sin that emerges from the rotating terms of the interaction, the system cannot synchronise, but it has a phase transition to a superradiant phase in which the spin and field have no oscillation [104].

6.2 Synchronisation in the quantum regime

In the classical limit, synchronisation is well-defined in terms of deterministic phase trajectories (see chapter 2). However, in the quantum regime, fluctuations that are neglected in a mean-field theory become significant. As a result, the transitions from an unsynchronised to a synchronised regime become less sharp, shifting the focus from whether a system is synchronised or not to the extent or degree of its synchronisation. In this way, while quantum oscillators offer a valuable framework for exploring the impact of quantum correlations on collective behaviour, concepts such as limit cycles, synchronisation, and entrainment require redefinition.

Van der Pol oscillators are a nonlinear oscillator with damping that varies with the amplitude of its oscillation. Because of the clear connection with its classical analogue, they are the most canonical object of study of quantum synchronisation [108–112]. Considering a van der Pol oscillator with wave packet initially localised near the position predicted for its classic limit cycle with minimum uncertainty, it will evolve to a delocalized wave packet along the trajectory of the limit cycle. This can be viewed in terms of the Wigner distribution of the oscillator, which evolves from a small ball to a ring-shaped form with the radius of the classical trajectory. This defines a quantum limit cycle with no phase preference. When an external driving is turned on, the distribution acquires a maximum that rotates along the classical trajectory [113].

In other quantum systems, unfortunately, the analogy is not as simple. Taking the case of spin systems, it has been debated if qubits can even possess valid limit cycles [114]. However, today, it is broadly accepted that they not only can be in a limit cycle but also synchronise with both an external driving and with another qubit [115–118, 111, 119]. In the context of few-level systems, spin 1 has also been investigated [120, 106], and in particular synchronisation of thee-level thermal machines [121, 122].

The authors in [121] use a quasiprobability distribution in phase space, named Husimi-Kano Q-representation, to measure phase localisation and argue that because thermal states are diagonal, they do not possess any phase preference, and so can be said to be in a limit cycle. This definition contrasts with the point of view presented in the last section, where we argue that the thermal normal state of a three-level heat engine is just a ‘trivial’ non-oscillating state and that the limit cycle is achieved with the Hopf bifurcation. Because the conditions for synchronisation are less restrictive than the conditions for having a limit cycle, the first is only achieved when the second can exist. The difference between the two points of view is rather subtle but can be summarised into the question of whether a stationary state should be considered a limit cycle. That said, the authors connect the thermodynamic behaviour of a heat engine with synchronisation, showing that the output power is bounded by the degree of synchronisation

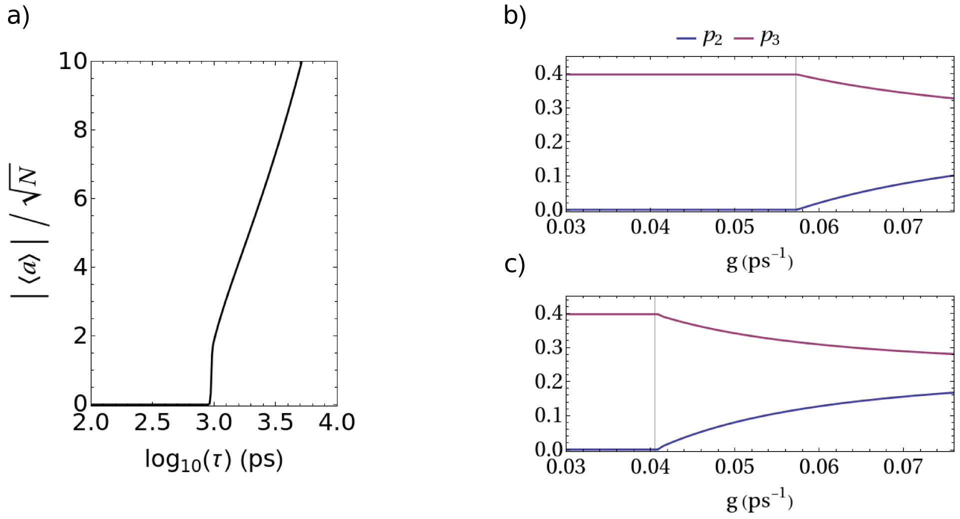

Figure 6.2: Steady-state simulation of an ensemble of $N = 10^9$ identical three-level heat engines interacting with a field. The absolute value of the normalised field operator as a function of the cavity lifetime in a logarithmic scale (a). The population of the excited levels as a function of the light-matter coupling for cavity lifetimes of $\tau = 100$ps (b) and $\tau = 200$ps (c) is given by the temperatures of the hot $T_h = 200$K and cold $T_c = 10$K baths at the normal state and tends towards equalisation as g increases. The grey vertical line shows the critical coupling predicted by the mean-field theory Eq. (6.13).

in the system. This result presents an important step in the connection between coherence and synchronisation, which has been further explored with a Liouvilian analysis [122].

We use Eqs. (6.5) to analyse the synchronisation of an ensemble of N identical three-level heat engines. We take the same parameters as for the polariton heat engine, with the third energy level shifted by the chemical potential, and consider that each system is in equilibrium with its reservoirs at an initial time when the field is perturbed. Figure 6.2 shows the long time results of the simulation. In (a), the absolute value of the normalised field operator shows a phase transition as the cavity lifetime is increased. Figures 6.2(b) and (c) show the excited populations as a function of the light-matter coupling strength g for two different cavity lifetimes. At the normal phase, populations depend solely on the choice of temperatures ($T_h = 200$K and $T_c = 10$K). However, for g above the threshold, the photon interaction establishes a tendency for equalisation of p_2 and p_3. The grey vertical line shows the phase boundary predicted by the mean-field theory Eq. (6.13), which agrees with the point at which population inversion becomes affected by the field.

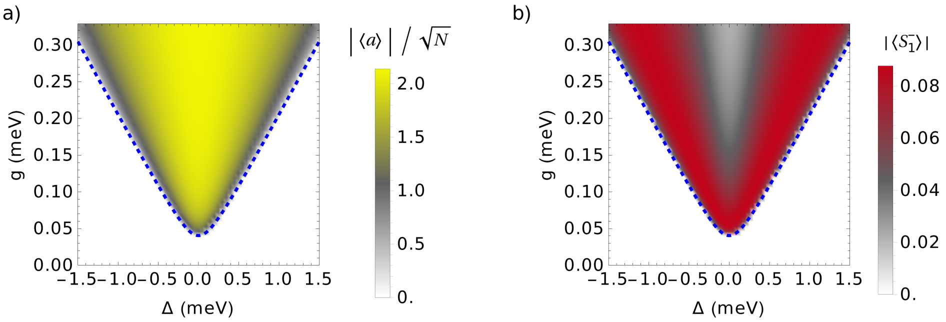

Figure 6.3: Colour maps of the average magnitude of the normalised field (a) and spin (b) as a function of the light-matter coupling g and the detuning Δ. The threshold follows Eq. (6.13), depicted as a blue dashed line, and shows the expected behaviour of the quantum Arnold's tongue.

Figure 6.3 shows the long-time behaviour of the absolute value of the normalised field operator and the absolute value of the average operator S_1^- as a function of the coupling strength and the detuning $\Delta = (e_3 - e_2) - \omega$, with the blue dashed line demarcating the phase boundary Eq. (6.13). The colour map in (a) shows the expected behaviour of a Arnold tongue (or 'cone'); however, (b) has a peak and decreases for higher values of g. The mean-field Eqs. (6.8) explain this behaviour. While high light-matter coupling implies a higher magnitude of a, it also reduces the inversion and consequently implies a smaller S_3. These two effects compete against each other, causing S_1^- to have a maximum value as a function of g. It is important to point out here that the Lindblad equation used to describe the effects of the reservoirs does not account for the energy shifts caused by the coupling with a, and, therefore, is only appropriate when these energy shifts, $\sim g|a|/\sqrt{N}$ are small compared with the variation in spectral densities and occupation functions. As we saw in Fig. 4.6(b), if these shifts were considered, the magnitude of the field would also have a maximum with respect to g.

In contrast with the classical Arnold tongue Fig. 2.3(b), the phase boundary on Fig. 6.3 does not touch the horizontal axes. This is because even with zero detuning, the system needs to overcome the losses γ and Γ to enter the laser/synchronised state. Near the threshold $J \propto g$, and so the shape of the phase boundary is a section of the "synchronisation cone" set by Eq. (6.14).

In the field of quantum synchronisation, a key focus of investigation is identi-

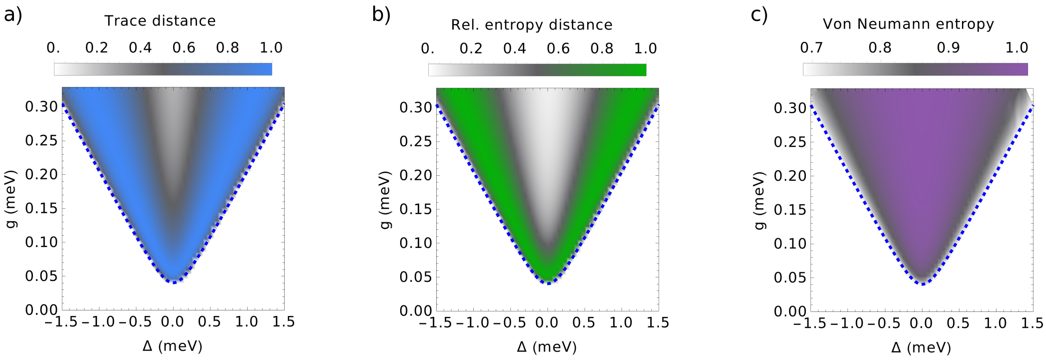

Figure 6.4: Potential quantifiers of synchronisation. (a) Normalised trace distance from the diagonal state. (b) Normalised relative entropy of synchronisation. (c) Von Neumann entropy.

fying the optimal measures for quantifying it. The choice of a suitable quantifier is often system-dependent as it must be measured in relation to the particular set of limit cycles that the system of interest can achieve. The phase space distribution has been used to measure phase concentration as a quantifier of synchronisation [114, 121, 116]. Information-based measures have been proposed both as tools for quantifying synchronisation and as means of linking it to quantum correlations [120, 109, 118, 111, 123, 124, 115].

To investigate the connection of phase locking with coherence and entanglement, we show the long-time behaviour of two synchronisation measures proposed in [106] and the von Neuman entropy in Fig. 6.4. The first two are normalised to be 1 at maximum. The synchronisation measures are constructed by defining a metric and taking the minimum distance $\mathcal{D}$ between the state and all possible limit cycles

$$\Omega(\rho) \equiv \min_{\sigma\in\Sigma}\mathcal{D}(\rho,\sigma), \tag{6.18}$$

where Σ is the set of all limit cycles. The trace distance is given by

$$\mathcal{D}_D(\rho,\sigma) = ||\rho-\sigma||_1 = \mathrm{Tr}[\sqrt{(\rho-\sigma)^\dagger(\rho-\sigma)}]. \tag{6.19}$$

The relative entropy by

$$\mathcal{D}_R(\rho,\sigma) = S(\rho||\sigma) = \mathrm{Tr}[\rho\log\rho - \rho\log\sigma]. \tag{6.20}$$

Considering the definition of limit cycle used by the authors in [121, 106], the limit cycle with minimum distance to the state of interest is the diagonal state. So, these measures become a measure of coherence, with similar behaviour to $|S_1^-|$. The von Neumann entropy of the steady-state density matrix presents a different behaviour, resembling the colourmap of $|\langle a\rangle|$. Its value in the normal state is defined by the steady-state populations defined by the choice of temperatures for the thermal reservoirs. In the laser state, the entropy increases, indicating that the coupling with the field causes a growth of the system-bath entanglement. A larger entanglement means more information on the system is lost, and so the process is less reversible.

6.3 Discussion

In this chapter, we extended our analysis of non-equilibrium condensation by discussing some fundamental aspects of the condensed state and comparing it to laser phenomena. We used a mean-field theory to establish the connection with phase locking in a microcavity with an ensemble of three-level heat engines and a field. We show that the non-equilibrium nature of the system shapes the phase boundary of condensation into a generalised version of the classical Arnold tongue; to what we call a synchronisation cone. Because the condition for synchronisation is weaker than the condition for the existence of a field, the second sets the conditions required for coherent emission. We also simulate the long-time dynamics of the system and calculate the measures of synchronisation proposed in [106].

The Dicke model has also been analysed with approaches that go beyond the first-order mean-field approximation [103, 125]. However, there is still much to explore. In further investigations, it would be interesting to look at the effects of considering an ensemble of non-identical three-level systems, with broadening over the energy levels, for example.

Chapter 7

Conclusions

In this thesis, we analysed Bose condensation in nonequilibrium quantum gases from the perspective of quantum thermodynamics. The nonequilibrium nature of these systems implies that there is a constant flow of energy and particles in the steady state, which connects condensation to laser phenomenon. We showed that as for a laser in Scovil's model [14], these condensates are constrained by the requirement of positive entropy production.

We focused on optical microcavities where light and matter interact to form polaritons or photon condensates. Starting with polaritons, we used kinetic equations to analyse the role of phonon-polariton and polariton-polariton scattering separately in the build up of a condensate. Using these results we built a three-level model to describe how a polariton gas, in contact with a non-resonant pump and a phonon reservoir, can produce work by emission of coherent light. We obtained a phase diagram (Fig.4.3) for condensation and showed that if the system is close to equilibrium, the phase boundary is defined by the reversible limit of the heat engine, that is, by the second law of thermodynamics. We analysed the effects of the internal structure of the pump and phonon reservoir on the phase transition (Fig. 4.7) and calculated thermodynamic figures of merit (Fig. 4.8). The results emphasise the importance of rapid cooling in the high-momentum exciton states, in order to maintain effective scattering into the condensate. Additionally, we analysed the effects of the exciton chemical potential in the operation of the three-level system, concluding that condensation can also happen in a dissipative and a refrigeration regime of the thermal machine (Figs. 4.9 and 4.10).

Next, we extended our approach to photon condensates. Using kinetic mean-field equations we showed that condensation of a photon gas is restricted by the condition of positive entropy production and it can also be mapped to a model of a three-level heat engine. We analysed the effects of a thermal pump, first looking at a two-level model, and later at a multimode model pumped with sunlight. We showed that condensation by sunlight harvesting can happen (Figs. 5.5 and 5.7) and that in an experimental setting, one should prefer a hotter light source weakly coupled to the cavity (Fig. 5.9).

Our results support the idea that nonequilibrium condensates are fundamentally analogous to laser phenomena. Therefore, in the last chapter, we analysed this connection and linked it with synchronisation. We showed that the nonequilibrium nature of a microcavity leads to a new dimension in the synchronisation phase diagram and that the existence of a limit cycle sets the condition for coherent emission of light.

Condensation in nonequilibrium Bose gases has various possible implementations and numerous practical and theoretical applications. Thermodynamics offers a general and comprehensive framework for analysing the ways in which particles and energy are allowed to be exchanged. The findings presented in this thesis use thermodynamics to enhance the understanding of the conditions necessary for condensation in polaritons and photon gases, and offer insights that can be applied to improve the efficiency of these systems. Furthermore, our work provides guidance for extending the regimes and systems that support condensation, and our methods could be extended to consider other examples of nonequilibrium quantum gases.

Bibliography

[1] J. Keeling and S. Kéna-Cohen, Annual Review of Physical Chemistry **71**, 435 (2020).

[2] H. Deng, H. Haug, and Y. Yamamoto, Reviews of Modern Physics **82**, 1489 (2010).

[3] R. C. Schofield, M. Fu, E. Clarke, I. Farrer, A. Trapalis, H. S. Dhar, R. Mukherjee, T. Severs Millard, J. Heffernan, F. Mintert, R. A. Nyman, and R. F. Oulton, Nature Photonics , 1 (2024).

[4] J. Klaers, J. Schmitt, F. Vewinger, and M. Weitz, Nature **468**, 545 (2010).

[5] P. Kirton and J. Keeling, Physical Review Letters **111**, 100404 (2013).

[6] T. K. Hakala, A. J. Moilanen, A. I. Väkeväinen, R. Guo, J.-P. Martikainen, K. S. Daskalakis, H. T. Rekola, A. Julku, and P. Törmä, Nature Physics **14**, 739 (2018).

[7] S. O. Demokritov, V. E. Demidov, O. Dzyapko, G. A. Melkov, A. A. Serga, B. Hillebrands, and A. N. Slavin, Nature **443**, 430 (2006).

[8] A. Kavokin and G. Malpuech, *Cavity Polaritons*, 1st ed., Thin Films and Nanostructures No. 32 (Elsevier, Acad. Press, Amsterdam, 2003).

[9] C. Schneider, A. Rahimi-Iman, N. Y. Kim, J. Fischer, I. G. Savenko, M. Amthor, M. Lermer, A. Wolf, L. Worschech, V. D. Kulakovskii, I. A. Shelykh, M. Kamp, S. Reitzenstein, A. Forchel, Y. Yamamoto, and S. Höfling, Nature **497**, 348 (2013).

[10] P. Bhattacharya, T. Frost, S. Deshpande, M. Z. Baten, A. Hazari, and A. Das, Physical Review Letters **112**, 236802 (2014).

[11] A. Rahimi-Iman, *Polariton Physics: From Dynamic Bose-Einstein Condensates in Strongly-Coupled Light-Matter Systems to Polariton Lasers* (Springer Nature Switzerland AG, 2020).

[12] D. Sanvitto and S. Kéna-Cohen, Nature Materials **15**, 1061 (2016).

[13] N. G. Berloff, M. Silva, K. Kalinin, A. Askitopoulos, J. D. Töpfer, P. Cilibrizzi, W. Langbein, and P. G. Lagoudakis, Nature Materials **16**, 1120 (2017).

[14] H. E. D. Scovil and E. O. Schulz-DuBois, Physical Review Letters **2**, 262 (1959).

[15] J. E. Geusic, E. O. Schulz-DuBios, and H. E. D. Scovil, Physical Review **156**, 343 (1967).

[16] R. Kosloff, The Journal of Chemical Physics **80**, 1625 (1984).

[17] E. Geva and R. Kosloff, Physical Review E **49**, 3903 (1994).

[18] E. Geva and R. Kosloff, The Journal of Chemical Physics **104**, 7681 (1996).

[19] M. T. Mitchison, Contemporary Physics **60**, 164 (2019).

[20] P. Eastham, *Bose Condensation in a Model Microcavity*, Ph.D. thesis, University of Cambridge (2001).

[21] J. Keeling and N. G. Berloff, Contemp. Phys. **52**, 131 (2011).

[22] M. H. Anderson, J. R. Ensher, M. R. Matthews, C. E. Wieman, and E. A. Cornell, Science **269**, 198 (1995).

[23] K. B. Davis, M. O. Mewes, M. R. Andrews, N. J. Van Druten, D. S. Durfee, D. M. Kurn, and W. Ketterle, Physical Review Letters **75**, 3969 (1995).

[24] T. Guillet and C. Brimont, Comptes Rendus Physique **17**, 946 (2016).

[25] S. Ghosh and T. C. H. Liew, npj Quantum Information **6**, 16 (2020).

[26] S. Klembt, T. H. Harder, O. A. Egorov, K. Winkler, R. Ge, M. A. Bandres, M. Emmerling, L. Worschech, T. C. H. Liew, M. Segev, C. Schneider, and S. Höfling, Nature **562**, 552 (2018).

[27] F. Chen, H. Li, H. Zhou, S. Luo, Z. Sun, Z. Ye, F. Sun, J. Wang, Y. Zheng, X. Chen, H. Xu, H. Xu, T. Byrnes, Z. Chen, and J. Wu, Physical Review Letters **129**, 057402 (2022).

[28] J. Chávez-Carlos, D. Garrido-Ramírez, A. J. V. Carmona, V. S. Batista, F. Pérez-Bernal, C. A. Trallero-Herrero, M. A. Bastarrachea-Magnani, and L. F. Santos, "Quantum sensing in an exciton-polariton condensate," (2024), arXiv:2407.14590 [cond-mat, physics:quant-ph] .

[29] D. Ballarini, M. De Giorgi, E. Cancellieri, R. Houdré, E. Giacobino, R. Cingolani, A. Bramati, G. Gigli, and D. Sanvitto, Nature Communications **4**, 1778 (2013).

[30] J. P. Moroney and P. R. Eastham, Physical Review B **108**, 195302 (2023).

[31] R. Hanai, A. Edelman, Y. Ohashi, and P. B. Littlewood, Physical Review Letters **122**, 185301 (2019).

[32] I. Carusotto and C. Ciuti, Reviews of Modern Physics **85**, 299 (2013).

[33] P. B. Littlewood, P. R. Eastham, J. M. J. Keeling, F. M. Marchetti, B. D. Simons, and M. H. Szymanska, Journal of Physics: Condensed Matter **16**, S3597 (2004).

[34] D. W. Snoke, Annalen der Physik **523**, 87 (2011), arXiv:1011.3849 .

[35] D. W. Snoke and J. P. Wolfe, Physical Review B **39**, 4030 (1989).

[36] F. Tassone and Y. Yamamoto, Physical Review B **59**, 10830 (1999).

[37] F. Tassone, C. Piermarocchi, V. Savona, A. Quattropani, and P. Schwendimann, Physical Review B **56**, 7554 (1997).

[38] H.-P. Breuer and F. Petruccione, *The Theory of Open Quantum Systems* (Oxford University Press, Oxford ; New York, 2002).

[39] C. N. Murphy, L. Toledo Tude, and P. R. Eastham, Applied Sciences **12**, 1620 (2022).

[40] R. Dümcke and H. Spohn, Zeitschrift für Physik B Condensed Matter **34**, 419 (1979).

[41] R. K. Wangsness and F. Bloch, Physical Review **89**, 728 (1953).

[42] G. Lindblad, Communications in Mathematical Physics **48**, 119 (1976).

[43] V. Gorini, A. Kossakowski, and E. C. G. Sudarshan, Journal of Mathematical Physics **17**, 821 (1976).

[44] G. Adesso, J. Anders, F. Binder, L. A. Correa, and C. Gogolin, eds., *Thermodynamics in the Quantum Regime: Fundamental Aspects and New Directions*, 1st ed., Fundamental Theories of Physics No. 195 (Springer International Publishing : Imprint: Springer, Cham, 2018).

[45] J. Gemmer, M. Michel, and G. Mahler, *Quantum Thermodynamics: Emergence of Thermodynamic Behavior Within Composite Quantum Systems*, Lecture Notes in Physics, Vol. 657 (Springer Berlin Heidelberg, Berlin, Heidelberg, 2004).

[46] G. T. Landi and M. Paternostro, Reviews of Modern Physics **93**, 035008 (2021).

[47] G. Maslennikov, S. Ding, R. Hablützel, J. Gan, A. Roulet, S. Nimmrichter, J. Dai, V. Scarani, and D. Matsukevich, Nature Communications **10**, 202 (2019).

[48] M. Campisi, J. Pekola, and R. Fazio, New Journal of Physics **17**, 035012 (2015).

[49] M. T. Mitchison, M. Huber, J. Prior, M. P. Woods, and M. B. Plenio, Quantum Science and Technology **1**, 015001 (2016).

[50] M. Esposito, M. A. Ochoa, and M. Galperin, Physical Review B **91**, 115417 (2015).

[51] C. N. Murphy and P. R. Eastham, Communications Physics **2**, 120 (2019).

[52] K. Zhang, F. Bariani, and P. Meystre, Physical Review A **90**, 023819 (2014).

[53] K. Zhang, F. Bariani, and P. Meystre, Physical Review Letters **112**, 150602 (2014).

[54] Y. Dong, K. Zhang, F. Bariani, and P. Meystre, Physical Review A **92**, 033854 (2015).

[55] Y. Dong, F. Bariani, and P. Meystre, Physical Review Letters **115**, 223602 (2015).

[56] J. Monsel, *Quantum Thermodynamics and Optomechanics*, Springer Theses (Springer International Publishing, Cham, 2020).

[57] N. Linden, S. Popescu, and P. Skrzypczyk, Physical Review Letters **105**, 130401 (2010).

[58] N. Brunner, N. Linden, S. Popescu, and P. Skrzypczyk, Physical Review E **85**, 051117 (2012).

[59] M. Kilgour and D. Segal, Physical Review E **98**, 012117 (2018).

[60] G. B. Cuetara, A. Engel, and M. Esposito, New Journal of Physics **17**, 055002 (2015).

[61] M. Esposito, U. Harbola, and S. Mukamel, Reviews of Modern Physics **81**, 1665 (2009).

[62] S. Gasparinetti, P. Solinas, A. Braggio, and M. Sassetti, New Journal of Physics **16**, 115001 (2014).

[63] A. Balanov, N. Janson, D. Postnov, and O. Sosnovtseva, *Synchronization*, Springer Series in Synergetics (Springer Berlin Heidelberg, Berlin, Heidelberg, 2009).

[64] J. Kasprzak, M. Richard, S. Kundermann, A. Baas, P. Jeambrun, J. M. J. Keeling, F. M. Marchetti, M. H. Szymańska, R. André, J. L. Staehli, V. Savona, P. B. Littlewood, B. Deveaud, and L. S. Dang, Nature **443**, 409 (2006).

[65] A. Baas, K. G. Lagoudakis, M. Richard, R. André, L. S. Dang, and B. Deveaud-Plédran, Physical Review Letters **100**, 170401 (2008).

[66] Q. Mei, K. Ji, and M. Wouters, Physical Review B **103**, 045302 (2021).

[67] I. Gnusov, S. Harrison, S. Alyatkin, K. Sitnik, J. Töpfer, H. Sigurdsson, and P. Lagoudakis, Science Advances **9**, eadd1299 (2023).

[68] K. A. Sitnik, I. Gnusov, M. Misko, J. D. Töpfer, S. Alyatkin, and P. G. Lagoudakis, Applied Physics Letters **124**, 201102 (2024).

[69] V. E. Hartwell, *Well - Microcavity Structures Experiments and Numerical Simulations*, Ph.D. thesis, University of Pittsburgh (2008).

[70] D. Porras, C. Ciuti, J. J. Baumberg, and C. Tejedor, Physical Review B **66**, 085304 (2002).

[71] A. Imamoglu, R. J. Ram, S. Pau, and Y. Yamamoto, Physical Review A **53**, 4250 (1996).

[72] P. G. Savvidis, J. J. Baumberg, D. Porras, D. M. Whittaker, M. S. Skolnick, and J. S. Roberts, Physical Review B **65**, 073309 (2002).

[73] V. E. Hartwell and D. W. Snoke, Physical Review B **82**, 075307 (2010).

[74] J. Levinsen, G. Li, and M. M. Parish, Physical Review Research **1**, 033120 (2019).

[75] E. Estrecho, T. Gao, N. Bobrovska, D. Comber-Todd, M. D. Fraser, M. Steger, K. West, L. N. Pfeiffer, J. Levinsen, M. M. Parish, T. C. H. Liew, M. Matuszewski, D. W. Snoke, A. G. Truscott, and E. A. Ostrovskaya, Physical Review B **100**, 035306 (2019).

[76] I. R. Lapidus, American Journal of Physics **50**, 45 (1982).

[77] A. I. Tartakovskii, D. N. Krizhanovskii, and V. D. Kulakovskii, Physical Review B **62**, R13298 (2000).

[78] M. M. Glazov, H. Ouerdane, L. Pilozzi, G. Malpuech, A. V. Kavokin, and A. D'Andrea, Physical Review B **80**, 155306 (2009).

[79] J. Ciers, D. D. Solnyshkov, G. Callsen, Y. Kuang, J.-F. Carlin, G. Malpuech, R. Butté, and N. Grandjean, Physical Review B **102**, 155304 (2020).

[80] G. Malpuech, A. Kavokin, A. Di Carlo, and J. J. Baumberg, Physical Review B **65**, 153310 (2002).

[81] C. Piermarocchi, F. Tassone, V. Savona, A. Quattropani, and P. Schwendimann, Physical Review B **53**, 15834 (1996).

[82] H. T. Cao, T. D. Doan, D. B. Tran Thoai, and H. Haug, Physical Review B **69**, 245325 (2004).

[83] R. Huang, Y. Yamamoto, R. André, J. Bleuse, M. Muller, and H. Ulmer-Tuffigo, Physical Review B **65**, 165314 (2002).

[84] J. Kasprzak, D. D. Solnyshkov, R. André, L. S. Dang, and G. Malpuech, Physical Review Letters **101**, 146404 (2008).

[85] T. D. Doan, H. T. Cao, D. B. T. Thoai, and H. Haug, Physical Review B **74**, 115316 (2006).

[86] G. Malpuech, Y. G. Rubo, F. P. Laussy, P. Bigenwald, and A. V. Kavokin, Semiconductor Science and Technology **18**, S395 (2003).

[87] R. Balili, V. Hartwell, D. Snoke, L. Pfeiffer, and K. West, Science **316**, 1007 (2007).

[88] A. Kavokin, ed., *Microcavities*, second edition ed., Series on Semiconductor Science and Technology No. 16 (Oxford University Press, Oxford ; New York, NY, 2017).

[89] T. D. Doan, H. T. Cao, D. B. Tran Thoai, and H. Haug, Physical Review B **72**, 085301 (2005).

[90] J. J. Baumberg, P. G. Savvidis, P. Lagoudakis, M. Martin, D. Whittaker, R. Butte, M. Skolnick, and J. Roberts, Physica E: Low-dimensional Systems and Nanostructures **13**, 385 (2002).

[91] S.-W. Li, M. B. Kim, G. S. Agarwal, and M. O. Scully, Physical Review A **96**, 063806 (2017).

[92] E. Busley, L. Espert Miranda, C. Kurtscheid, F. Wolf, F. Vewinger, J. Schmitt, and M. Weitz, Physical Review A **107**, 052204 (2023).

[93] S. Klembt, E. Durupt, S. Datta, T. Klein, A. Baas, Y. Léger, C. Kruse, D. Hommel, A. Minguzzi, and M. Richard, Physical Review Letters **114**, 186403 (2015).

[94] J. Klaers, F. Vewinger, and M. Weitz, Nature Physics **6**, 512 (2010).

[95] T. Damm, J. Schmitt, Q. Liang, D. Dung, F. Vewinger, M. Weitz, and J. Klaers, Nature Communications **7**, 11340 (2016).

[96] F. E. Öztürk, F. Vewinger, M. Weitz, and J. Schmitt, Physical Review Letters **130**, 033602 (2023).

[97] P. Kirton and J. Keeling, Physical Review A **91**, 033826 (2015).

[98] M. Pieczarka, M. Gębski, A. N. Piasecka, J. A. Lott, A. Pelster, M. Wasiak, and T. Czyszanowski, Nature Photonics , 1 (2024).

[99] A. Rose, Journal of Applied Physics **31**, 1640 (1960).

[100] R. Kosloff and A. Levy, Annual Review of Physical Chemistry **65**, 365 (2014).

[101] L. Zhang, J. Hu, J. Wu, R. Su, Z. Chen, Q. Xiong, and H. Deng, Progress in Quantum Electronics **83**, 100399 (2022).

[102] P. R. Eastham and P. B. Littlewood, Solid State Communications **116**, 357 (2000).

[103] P. Kirton, M. M. Roses, J. Keeling, and E. G. Dalla Torre, Advanced Quantum Technologies **2**, 1800043 (2019).

[104] P. Kirton and J. Keeling, New Journal of Physics **20**, 015009 (2018).

[105] P. R. Eastham, M. H. Szymanska, and P. B. Littlewood, Solid State Communications Quantum Phases at the Nanoscale, **127**, 117 (2003).

[106] N. Jaseem, M. Hajdušek, P. Solanki, L.-C. Kwek, R. Fazio, and S. Vinjanampathy, Physical Review Research **2**, 043287 (2020).

[107] P. Fowler-Wright, B. W. Lovett, and J. Keeling, Physical Review Letters **129**, 173001 (2022).

[108] T. E. Lee and H. R. Sadeghpour, Physical Review Letters **111**, 234101 (2013).

[109] T. E. Lee, C.-K. Chan, and S. Wang, Physical Review E **89**, 022913 (2014).

[110] S. Walter, A. Nunnenkamp, and C. Bruder, Physical Review Letters **112**, 094102 (2014).

[111] V. Ameri, M. Eghbali-Arani, A. Mari, A. Farace, F. Kheirandish, V. Giovannetti, and R. Fazio, Physical Review A **91**, 012301 (2015).

[112] S. Dutta and N. R. Cooper, Physical Review Letters **123**, 250401 (2019).

[113] T. Weiß, *Nonlinear Dynamics in Quantum Synchronization and Topological Transport*, Ph.D. thesis, Nonlinear dynamics in quantum synchronization and topological transport Nichtlineare Dynamik in der Quantensynchronisation und in topologischem Transport Der Naturwissenschaftlichen Fakultät der Friedrich-Alexander-Universität Erlangen-Nürnberg (2017).

[114] A. Roulet and C. Bruder, Physical Review Letters **121**, 053601 (2018).

[115] H. Eneriz, D. Z. Rossatto, F. A. Cárdenas-López, E. Solano, and M. Sanz, Scientific Reports **9**, 19933 (2019).

[116] Á. Parra-López and J. Bergli, Physical Review A **101**, 062104 (2020).

[117] P. Kurzyński, Physical Review Research **2**, 033289 (2020).

[118] O. V. Zhirov and D. L. Shepelyansky, Physical Review B **80**, 014519 (2009).

[119] G. L. Giorgi, F. Plastina, G. Francica, and R. Zambrini, Physical Review A **88**, 042115 (2013).

[120] A. Roulet and C. Bruder, Physical Review Letters **121**, 063601 (2018).

[121] N. Jaseem, M. Hajdušek, V. Vedral, R. Fazio, L.-C. Kwek, and S. Vinjanampathy, Physical Review E **101**, 020201 (2020).

[122] P. Solanki, N. Jaseem, M. Hajdušek, and S. Vinjanampathy, Physical Review A **105**, L020401 (2022).

[123] G. L. Giorgi, F. Galve, G. Manzano, P. Colet, and R. Zambrini, Physical Review A **85**, 052101 (2012).

[124] G. Manzano, F. Galve, G. L. Giorgi, E. Hernández-García, and R. Zambrini, Scientific Reports **3**, 1439 (2013).

[125] F. Carollo and I. Lesanovsky, Physical Review Letters **126**, 230601 (2021).

Appendix A

Polariton heat engine: equations-of-motion

This Appendix contains additional equations relevant to the chapter 4. In chapter 4 we analysed the equations for the energy currents between the three-level system and the hot and cold baths. Here we present the equations-of-motion for the elements of the density matrix of the three-level system and analyse the limit of small coupling (or large detuning).

The equations-of-motion for the diagonal elements of the density matrix, in the bare basis, are given in Eqs. (4.16–4.18). We give here the remaining terms, considering the contributions from the two baths separately. We use an abbreviated notation in which subscripts denote the frequencies at which the spectral densities and bath occupations are sampled, so that in expressions for the cold (hot) bath we have $J_i = J_c(\tilde{e}_i), n_i = n_c(\tilde{e}_i)$ $(J_i = J_h(\tilde{e}_i + \omega), n_i = n_h(\tilde{e}_i + \omega))$. For the cold bath we have

$$\begin{aligned}\dot{\rho}_{23}|_c = -\frac{\pi}{2}\{&[\rho_{11}(J_2 n_2 - J_3 n_3) + \rho_{33}(J_3(1+n_3) - J_2(1+n_2))]\sin\theta \\ &+ \rho_{23}[J_2(1+n_2)(1+\cos\theta) + J_3(1+n_3)(1-\cos\theta)]\},\end{aligned} \tag{A.1}$$

$$\dot{\rho}_{12}|_c = -\frac{\pi}{2}\{(\rho_{12}-\rho_{21})[J_2(1+2n_2)(1+\cos\theta)+J_3(1+2n_3)(1-\cos\theta)] \\ +(\rho_{13}-\rho_{31})[J_3(1+n_3)-J_2(1+n_2)]\sin\theta\}, \quad (A.2)$$

$$\dot{\rho}_{13}|_c = -\frac{\pi}{2}\{\rho_{13}[J_2n_2(1+\cos\theta)+J_3n_3(1-\cos\theta)] \\ +\rho_{21}[J_2n_2-J_3n_3]\sin\theta\}. \quad (A.3)$$

The corresponding expressions for the hot bath are

$$\dot{\rho}_{23}|_h = -\frac{\pi}{2}\{[\rho_{11}(J_2n_2-J_3n_3)+\rho_{22}(J_3(1+n_3)-J_2(1+n_2))]\sin\theta \\ +\rho_{23}[J_2(1+n_2)(1-\cos\theta)+J_3(1+n_3)(1+\cos\theta)]\}, \quad (A.4)$$

$$\dot{\rho}_{13}|_h = -\frac{\pi}{2}\{\rho_{13}[J_3(1+2n_3)(1+\cos\theta)+J_2(1+2n_2)(1-\cos\theta)] \\ +\rho_{12}[J_3(1+n_3)-J_2(1+n_2)]\sin\theta\}, \quad (A.5)$$

$$\dot{\rho}_{12}|_h = -\frac{\pi}{2}\{\rho_{12}[J_3n_3(1+\cos\theta)+J_2n_2(1-\cos\theta)]\}. \quad (A.6)$$

In the limit $\theta \to 0$, the energies of the dressed states reduce to the original energies, $\tilde{e}_2 = e_2, \tilde{e}_3 = e_3 - \omega$, and the equations-of-motion become the standard Lamb equations for a three-level laser [18]. The population transfer rates become

$$R^c = 2\pi J_2(1+n_2)\rho_{22} - 2\pi J_2n_2\rho_{11} \\ = \gamma^c_\downarrow\rho_{22} - \gamma^c_\uparrow\rho_{11}, \quad (A.7)$$

$$-R^h = 2\pi J_3(1+n_3)\rho_{33} - 2\pi J_3n_3\rho_{11} \\ = \gamma^h_\downarrow\rho_{33} - \gamma^h_\uparrow\rho_{11}. \quad (A.8)$$

The dissipative contributions to the equations-of-motion for the off-diagonal elements of the density matrix become

$$\dot{\rho}_{23} = -\frac{1}{2}(\gamma_{\downarrow}^{c} + \gamma_{\downarrow}^{h})\rho_{23}, \tag{A.9}$$

$$\dot{\rho}_{13} = -\frac{1}{2}(\gamma_{\uparrow}^{h} + \gamma_{\downarrow}^{h} + \gamma_{c}^{\uparrow})\rho_{13}, \tag{A.10}$$

$$\dot{\rho}_{12} = -\frac{1}{2}(\gamma_{\uparrow}^{c} + \gamma_{\downarrow}^{c} + \gamma_{h}^{\uparrow})\rho_{12}. \tag{A.11}$$

where a counterrotating term from the cold bath has been neglected in Eq. (A.11). These expressions describe the decay of the coherences, with the rates related in the expected way to those of the populations.